Performance Assessment of Transient Behaviour of Small Wind Turbines

by

Kevin Pope

A Thesis Submitted in Partial Fulfillment
of the Requirements for the Degree of

Masters of Applied Science

in

The Faculty of Engineering and Applied Science

Mechanical Engineering

University of Ontario Institute of Technology

August 2009

Abstract

Small wind turbine installations have a variety of potential uses, each with unique performance demands and operating conditions. Many applications require that the turbine is placed in wind conditions that are not ideal for optimum operation. Better predictive techniques can improve wind turbine performance through improved control strategies and enhanced designs. Conventional methods of wind power design and control utilize an average power coefficient. In this thesis, various techniques to predict the transient power coefficient of a wind turbine are developed. The operation of a Savonius wind turbine is accurately represented, with a new model which considers the flow distributions to predict the changes in power output at all rotor positions. Another model is developed that represents the dynamics of a small horizontal wind turbine, including the effect of transient wind conditions on rotor speed and acceleration. These can supplement current methods to determine turbine placement, selection and categorization.

Acknowledgments

My supervisor Dr. Greg F. Naterer is thanked for his expert guidance and exceptional patience. Also, the Ontario Graduate Scholarship program (OGS), Zephyr Alternative Power Inc. and the Natural Sciences and Engineering Research Council of Canada (NSERC) are gratefully acknowledged for their financial support.

Table of Contents

List of Tables

List of Figures

Nomenclature

a	Radius of cylindrical blade [m]
A	Area [m^2]
b	Number of blades
c	Chord length of rotor blade [m]
C_a	Axial induction factor
C_D	Drag coefficient
C_L	Lift coefficient
C_p	Power coefficient
$C_p h$	Specific heat capacity [J/kg-˚K]
d	Distance to origin [m]
$\hat{e}$	Position vector of cylindrical coordinate system
E	Empirical constant
ex	Specific exergy [J/kg]
$\dot{Ex}$	Exergy rate [W]
g	Acceleration of gravity [m/s^2]
H	Turbine height [m]
i	Turbulence intensity
I	Irreversibilities [W]
J	Polar moment of inertia [m^4]
k_w	Weibull shape parameter
k_P	Turbulence kinetic energy at point P [J]
K	Kármán constant
KE	Kinetic energy [J]

L	Length [m]
m	Mass [kg]
$\dot{m}$	Mass flow rate [kg/s]
p	Pressure [Pa]
P	Power [W]
Q	Torque [J]
$\vec{r}_0$	Distance to origin of rotating system [m]
r	Radius [m]
R	Rotor radius [m]
R^2	Coefficient of determination
s	Scaling factor
S	Solidity
t	Time [s]
T	Temperature [˚C]
u	x-component of velocity [m/s]
$\vec{u}_r$	Whirl velocity [m/s]
U	Freestream velocity [m/s]
U_P	Mean fluid velocity at point P [m/s]
v	y-component of velocity [m/s]
$\vec{v}_r$	Relative velocity [m/s]
$\vec{v}$	Absolute velocity [m/s]
V	Mean wind velocity [m/s]
V_{rev}	Relative wind velocity [m/s]
~~V~~	Volume [m^3]

W	Turbine width [m]
W_x	x-component of relative wind velocity [m/s]
W_{out}	Work output [J]
y_P	Distance from point P to the wall [m]
Y	Output [W]
z	Vertical position [m]

Greek

β	Rotor overlap [m]
η	Energy efficiency
θ	Rotor position [rad]
$\dot{\theta}$	Angular velocity [rad/s]
$\ddot{\theta}$	Angular acceleration [rad/s^2]
θ_s	Stator angle [rad]
λ	Tip speed ratio
μ	Dynamic viscosity of air [Pa-s]
ξ	Numerically determined variable
ρ	Wind density [kg/m^3]
σ	Stator spacing [m]
$\bar{\bar{\tau}}_r$	Viscous stress [N/m^2]
τ_w	Wall shear stress [Pa]
φ	Angle of relative wind [˚]
ϕ	Cylindrical coordinate
ψ	Exergy efficiency

Ψ	Stream function
ω	Humidity ratio
$\vec{\omega}$	Angular velocity relative to stationary frame [rad/s]
Ω	Rotor velocity [rad/s]

Subscripts

0	Ambient
B	Benz limit
c	Cell
D	Drag
dest	Destruction
e	Exit
eff	Effective
f	Face
KE	Kinetic energy
L	Lift
ph	Physical
r	Radial coordinate
s	Surface
x	Horizontal vector
y	Vertical vector

Chapter 1

Introduction

Combustion of vast quantities of fossil fuels worldwide for power production is responsible for numerous environmental problems. The emissions from hydrocarbon combustion contain pollution agents including NO_x, SO_x, CO and CO_2. These chemicals are connected to a variety of environmental degradation problems, including acid rain, smog, and climate change. There is an urgent need to alter the current consumption and production patterns that rely on fossil fuels. Wind power can provide a sustainable contribution to society's energy needs, while reducing our needs for fossil fuels.

1.1 Background

Significant evidence exists that the environmental impact of climate change is rapidly gaining momentum and its alleviation has paramount importance. Since the combustion of fossil fuels, and the subsequent release of carbon dioxide (CO_2) emissions, is a primary cause of climate change, reducing these polluting emissions is crucial to sustainability. Driven by its emission-free operation, the capacity of wind power has expanded rapidly to make a significant contribution to global electricity generation. The

World Wind Energy Association (WWEA) has reported yearly growth rates in global wind energy generation from 2006 to 2008 of 25.6%, 26.6% and 29%, respectively [1 - 3]. During 2008, the global installed capacity grew by 27.3 GW, bringing the overall total to 121.2 GW, capable of generating an annual total of 260 TWh. These promising trends led WWEA to predict that over 1.5 TW of installed wind power capacity is possible by the end of 2020 [3].

Despite these rapid developments, wind power still only contributes 1.5% of the global energy generation [3]. For wind power to increase market penetration, several different potentials need to be fulfilled to help maximize wind power potential, reduce costs, and encourage public acceptance. Wind power is an ancient technology that has recently seen a resurgence of interest and use. In past years, the vast quantities of energy supplied by fossil fuels, along with the bountiful supplies available, made wind power economically uncompetitive. Consequently, its benefits were not fully utilized. The recent resurgence of wind power has seen a variety of different design configurations and operating principles.

1.2 Literature survey

An overview of past literature, pertaining to three important areas of small wind turbine installations, is presented in this section. This includes (i) wind turbine designs, (ii) urban wind power potential, and (iii) efficiency predictors and power control.

1.2.1 Wind turbine designs

As illustrated in Fig 1.1, wind turbines are commonly categorized into two distinct divisions, vertical and horizontal axis wind turbines (VAWTs and HAWTs). Such a

division considers both mechanical properties and design issues. Each division has many variations, with their own unique benefits and drawbacks.

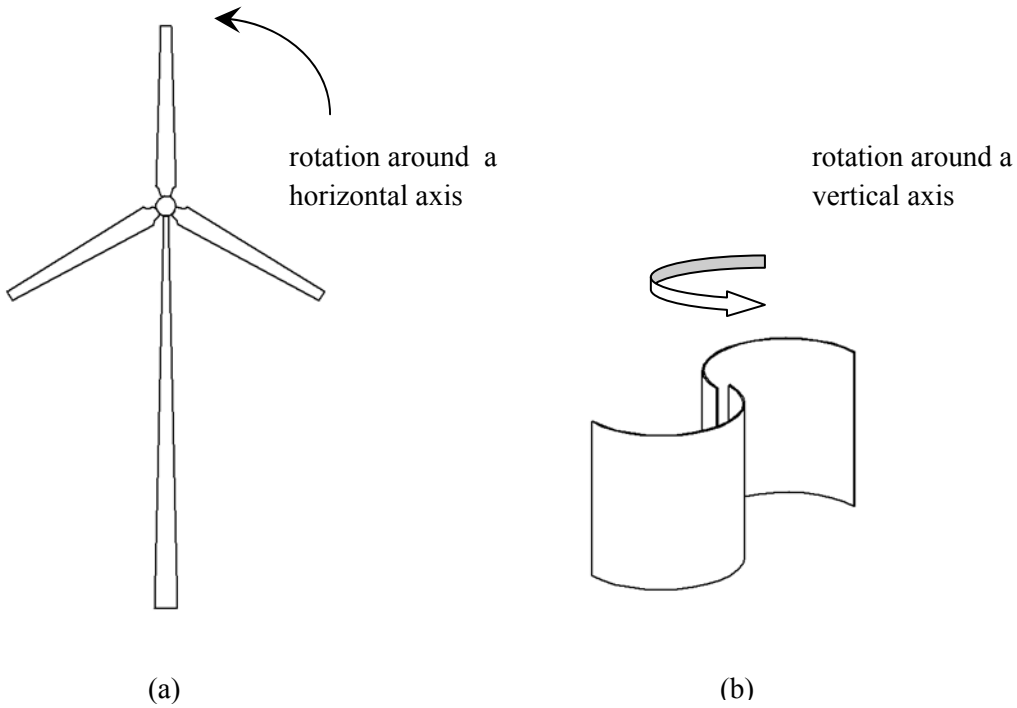

Figure 1-1 Wind turbines with (a) horizontal axis and (b) vertical axis of rotation

Horizontal axis wind turbines (refer to fig. 1a) have captured the majority of the current market, due to their high efficiencies in strong winds. A lift force is generated as the wind flows over the rotating airfoils. The twist in the rotor blades allows the lift to be in the direction of rotation throughout its length (the relative wind speed and the blade rotation are combined to get this vector). The drag force on a HAWT is perpendicular to the rotation; it does not directly affect the rotational force, but it can indirectly reduce the lift force and generate instability. This popular design is generally used in remote high wind locations. HAWTs are ineffective in turbulent winds as they require stable wind direction and velocity for efficient operation. Fluctuations in wind direction result in large power fluctuations, thereby decreasing the stability, fatigue strength and electrical

stability of the turbines. Reducing the torque and fatigue fluctuations on the shaft of a HAWT can help increase longevity and decrease maintenance costs [4]. This can be achieved, in part, by placing the turbine in an area of low turbulence. Remote wind power generation adds to the required land resources. This may require the construction, installation, and maintenance of roads and power lines, adding to the economic and environmental costs of the system.

In the second category of wind turbines, VAWTs have their own benefits and drawbacks. There are differences in structural dynamics, control systems, maintenance, manufacturing and electrical equipment. Comparing a typical HAWT design to two VAWT designs in terms of these variables, VAWTs offer several advantages over the HAWT. The major advantage is a VAWT (H-rotor) design's ability to keep the structure simple. This is achieved by eliminating the need for a yaw mechanism, pitch regulation and gearbox. This limits the number of mechanical parts, as well as the complexity, thereby reducing maintenance and installation expenses [5]. Such strengths provide VAWTs with unique advantages that have not been fully utilized to date.

VAWTs can be further categorized into lift and drag machines. Such a division represents the main operating forces used during turbine operation. This is a less clearly defined division, as many designs experience both forces in varying amounts. The forces can both contribute to the turbine performance (such as a drag VAWT illustrated in Fig. 1b), or one force detracts from the turbine performance, and it should be limited (such as the drag force on an H-rotor (lift) VAWT). The turbines which use primarily lift forces (Darrius type designs) can achieve higher efficiencies than drag force designs. With the use of vertical airfoils, either curved (Darrius) or straight (H-rotor) blades, these turbines use the combination of the wind and rotational speed to achieve a force vector which is in

the direction of rotation. However, a different design style of the VAWT has the potential to offer significant advantages in high turbulence areas. In particular, a VAWT that relies mainly on drag forces to accelerate the rotor is often called a variation of the Savonius design, or less commonly, a drag machine. Relatively simple construction, acceptance of wind from any direction regardless of orientation, low cost, self-starting, and quiet operations are among the many benefits of the design. Since a drag machine (Savonius) is designed to use a larger portion of the drag forces to achieve rotation, the magnitude and direction of the lift force becomes highly variable. Generally, the magnitude of the lift force is also significantly reduced because typical aerofoil geometries are not used. A drag machine's output is limited by a theoretical maximum λ (tip speed ratio) below one. Relatively low efficiencies, compared with lift type designs (both HAWT and VAWT) have limited the number of installations with this particular design configuration.

Past literature [6-8] has shown efficiency improvements and competitive efficiencies. For example, in a series of 16 wind tunnel experiments, researchers [6] investigated Savonius models with identical aspect ratios. An optimum number of rotor blades (two or three), number of stages (one, two, or three), and the blade shape (twisted or semicircular) were investigated. The author found that a two stage design, with two twisted rotor blades, preformed the best, achieving a maximum power coefficient of 0.32. A two stage design means two turbines are stacked, one on top of the other, and generally set at varying angles to stagger the peaks in force produced in each stage, thereby producing an overall power output with reduced variability. This result was validated by a series of wind tunnel tests, whereby Savonius turbines were compared and the effect of rotor overlap was investigated. A maximum power coefficient (C_p) of 0.37 was reported by the authors [7]. This compares well with published HAWT power coefficients. For

example, a micro HAWT with a rotor diameter of 0.5 m was tested for an intended purpose of urban use. The authors [8] reported a power coefficient of 0.36.

Current research and design improvements are available for Savonius designs. A hybrid design was developed from the combination of Savonius (drag) and Darrieus (lift) turbines. This has the potential to utilize the particular advantages of each design. Recent experiments found that a hybrid Savonius-Darrieus turbine could achieve a maximum C_p of 0.51 [9]. In contrast to the stand-alone Savonius design, a hybrid Savonius-Darrieus turbine performs best with no overlap within the Savonius rotors [7]. A comparative experimental study reported that when the wind velocities fluctuated rapidly, a design with a Savonius rotor within a Darrieus turbine preformed better than either individual turbine. The hybrid turbine performed better than the summation of individual turbines because of the decreased startup time achieved by the hybrid design. The combined effect decreases the power output, due to flow interference between the rotors. However, this detrimental effect is outweighed by the benefits of improved startup. This is a result of a Savonius turbine's high solidity and torque, which are utilized by connecting it to a Darrieus design, thereby improving startup performance. This is an effective balance of the operating advantages of each turbine [10]. Such operating advantages are important for a wind turbine placed in urban centers and they are generally analogous with the requirements of small wind power installations.

1.2.2 Urban wind power potential

In this section, the potential for wind power generation in urban settings is investigated. Wind power is predominantly derived from horizontal axis wind turbines (HAWTs), in mid to large scale wind farms. Although these large centralized installations

are beneficial, there is a significant opportunity to increase capacity by smaller scale distributed generation. Producing power where it will be used can reduce installation and land costs, with little or no transmission expense. An urban center fulfills the needs of distributed power, as there is a significant power demand and available structures that can act in place of a high support tower. The conventional HAWTs are often favoured due to their higher efficiency, but they are not necessarily suitable for all purposes. Horizontal axis turbines require sustained wind velocities to efficiently generate power. The performance demands of an urban wind power installation require a turbine that can operate within the harsh conditions produced from the complex terrain.

Considerations of turbulence do not fully represent the operating conditions of urban wind power, as changes in wind direction are also significant. For example, the effects of different levels of inlet turbulence intensity were experimentally investigated by altering the turbulence intensity by 4.4%, 9% and 12%. A minimal effect on turbine performance with increasing turbulence intensity was reported by the authors [11]. However, in complex terrain, fatigue loads on HAWTs can be up to 75% higher, due to high turbulence and changing wind direction [12]. Similarly, small wind turbine loading increases by about 25% when placed in complex terrains [13]. The use of VAWTs, or other design features that can withstand the added fatigue, are essential, as severe turbine failure is unacceptable within densely populated urban centers. VAWTs offer intrinsic operation features, such as a lower λ, to resist these fatigue loads without expensive materials or overdesigned safety margins.

HAWTs do not operate well in regions of high turbulence, such as urban areas [14]. The flows in urban canyons with and without street obstructions have been experimentally investigated with a series of wind tunnel tests. The authors [15] reported

an increased turbulence of 50% to 200% when the street obstructions were included. Thus, with the multitude of obstructions in a typical urban center, the turbulence within urban canyons leads to very harsh conditions for wind power generation, particularly for turbine designs that do not perform well in conditions of very high turbulence (inherent to virtually all lift type designs). Furthermore, the city structures within an urban center act as a heat source, causing unstable and turbulent winds. The resulting thermal gradient causes highly unstable and unpredictable flow fields [16]. Experimental investigations of the turbulence associated with urban roughness found evidence of two-scale turbulence behaviour at the top of the canopy region. The authors [17] suggest that the small-scale turbulence is likely generated by the separated shear layers, intermingled with large-scale eddies. This causes harsh operating conditions for a wind turbine, especially if it is mounted on an urban rooftop. In another study, a detailed analysis of the influence of wind direction on intense power fluctuations in large offshore windfarms in the North Sea was performed. The authors [4] reported that the excessive power fluctuations from the wind farm pose a significant risk, requiring further assessment.

Urban wind turbulence can provide unique obstacles for the startup requirements of wind turbines. Large installations generally use a motor to rotate the rotor to the required rotational velocity. However, low cost and maintenance restrictions make self startup an essential feature of small wind turbine installations. This comes with considerable implications for urban wind power. Successful urban installations must efficiently provide self startup and HAWTs can lose significant power in low wind or turbulent conditions. The wind speeds typical in urban areas are significantly lower than those in rural areas, which can cause a standard HAWT to remain stationary for 21% of the year [18]. Since most small HAWTs do not have variable pitch blades, the angle of

attack at startup does not coincide with the low rotational speeds. This can cause an appreciable delay in the rotor's acceleration. In an experimental study, turbines begin rotating at 4.6 m/s on average, but this varied between 2.5 and 7.0 m/s [19]. The operating features of a VAWT exhibit noticeable advantages over a HAWT in this area, as reduced cut-in speed (the lower limit of a turbine's operating range of wind velocities) and an ability to accept turbulent wind are advantages of most Savonius (drag) type turbines.

In an urban setting, the wind is always changing speed, and the direction is rarely uniform. In these conditions, vertical axis wind turbines (VAWTs) can be more effectively harnessed within complex urban terrains to significantly increase the capacity of small scale wind power generation. Three urban locations for VAWT placement have been recommended. Locating it between diffuser shaped buildings can improve the aerodynamic efficiency of the turbine. Placing a wind turbine in a duct through a building can use the pressure difference between the windward and leeward sides of the building for power generation. Also, a turbine on top or alongside a building will be exposed to higher wind speed areas close to the building [20]. Wind power could potentially provide a large portion of Canada's power. Issues of intermittency arise as the use of the resource increases. This can be alleviated by expanding the capacity of urban power, because distributing the turbines amongst various cities will smooth the wind speed correlations, thereby mitigating problems of intermittency [21].

All renewables have a positive effect on greenhouse gas emissions [22]. A past study included construction, maintenance and demolition in the life cycle analysis of a wind farm. The authors [23] reported 3 grams of CO_2 for each kWh of electricity from coastal wind power plants, and 25 grams of CO_2 for each kWh of electricity from inland plants. This is less than other predicted footprints, such as 130 grams of CO_2 for each

kWh of electricity from photovoltaics. Distributed generation comes with justifiable concerns about added costs pertaining to the economies of scale. This has implications for both CO_2 emissions and turbine economics. A past published analysis [24] presented a life cycle audit of the energy use and CO_2 emissions for a 1.5 kW rooftop-mounted HAWT. A comparable CO_2 footprint to larger wind turbines was reported, providing some alleviation for such concerns.

1.2.3 Efficiency predictors and power control

With current methods, the wind kinetic energy is generally the primary parameter that establishes maximum power output. By relating this wind energy to the rotor dynamics, electrical systems can have a more useful upper bound for the rotor control strategy. By developing better predictive and control methods, a larger portion of wind power can be extracted from existing systems. Models of wind turbine dynamics can be categorized into three general areas: (i) models based on wind turbine power curves, (ii) sub-transient models, and (iii) transient / dynamic models. Methods in the first category are useful for predictions of total power from different turbines operating at various sites. But they cannot represent the dynamic behaviour of the turbine. To provide designers and engineers with more detailed design tools, it is important that the dynamics are fully represented, as their impact is significant on electrical grid integration and operation of variable speed turbines. Sub-transient refers to those models with the smallest timescales (typically less than 1 second). Sub-transient models are more complex and often require a time step size that is too small for practical use in actual power system dynamics [25]. Transient refers to the models with a timescale between sub-transient and steady state. An important advantage of this category is its ability to better compare variable and constant

speed wind turbines, with one model. Better model accuracy is a key factor in achieving technology advancements and capacity improvements for wind turbines.

Historically, wind turbine controllers have relied heavily on trial and error to adjust the rotor and shaft dynamics. However, recently there has been significant progress that allows a variety of new models to become available, from single state models, to more complicated models that have hundreds of states [26]. Lavoie et al. [27] designed a two degree of freedom predictive controller that uses a cost function minimization in the algorithm. A wind turbine power controller with accurate response to both the set-point change and disturbances was reported. Sliding mode controllers are an efficient method of wind turbine operation. They have been shown to maximize energy capture by tracking the wind speed fluctuations, applying an adaptive feedback linearization control strategy. In a computer simulation, the controlled turbines exhibited a significant improvement in performance compared to a fixed speed wind turbine [28]. In another study, a sliding mode control was used for efficiency optimization with a double output induction generator. The authors presented a control strategy that commands the inverter firing angle so that the extreme control values are maximized [29].

In past literature, a number of dynamical and control models have been reported to utilize the wind kinetic energy to predict turbine power (for examples, see references [26, 30, 31]). These predictions can be used to control the rotor pitch and generator resistance to optimize power output. Common among all models, the kinetic energy of the wind is the primary input for each model. More sophisticated models supplement this input by including various effects including structural resonance, blade vibrations, yaw motion, cross wind error, and many more.

Typical design methodologies employ the first law of thermodynamics for wind power system analysis and design. Empirical tests and experience must often be used to improve system performance and implementation. The process irreversibilities are not represented in the analysis [32]. A theoretical maximum efficiency can be predicted, but irreversibilities are not identified. With a first law methodology, the designer includes a pre-determined design factor to account for the irreversibilities. Past experimental results have shown that the actual flow across a wind turbine rotor is 20% slower than the ideal flow [33]. Predicting turbine performance with complicated variations in operating demands and design configurations reveal the deficiencies with this strategy [34]. In contrast, the second law defines a quality of energy and quantity of irreversibility or loss associated with the thermodynamic process. In this thesis, the concept of entropy generation will be used to describe the magnitude of energy dissipation. Higher levels of entropy generation are associated with a lower level of useful energy. The second law requires that the amount of entropy in an isolated system will always increase [35]. This principle can be applied to a variety of engineering applications, including wind turbines in this thesis.

Entropy-based design and exergy analysis have been shown to identify the maximum theoretical capability of energy system performance in various applications. For example, it can provide component-level energy management to improve diffuser performance [36] and reduce voltage losses within a fuel cell [37]. Exergy analysis has been used to diagnose inefficiencies of power plants [38], minimize the carryover leakage irreversibilities in a power plant regenerative air heater [39], and many other power plant associated applications. These studies have shown exergy analysis to be very useful for

improving a wide range of thermofluid systems. Exergy analysis also provides a design tool for increased accuracy and more efficient performance.

However, there are few examples in past literature [40, 41] that pertain to wind exergy. Through an energy and exergy analysis of the characteristics of wind energy, it was found that differences between energy and exergy efficiencies are approximately 20 - 24% at low wind speeds and approximately 10 - 15% at high wind speeds [40]. Sahin et al. [41] developed a useful exergetic analysis technique for determining the exergetic efficiency of a wind turbine. The technique utilizes the wind chill temperature associated with wind velocity to predict the entropy generation of the process. Better turbine design and location selection can be achieved with the aid of such exergy analysis.

1.3 Objectives and overview of thesis

The main objective of this thesis is to improve the predictive techniques of small wind turbines. Various techniques to predict the transient power coefficient of a wind turbine are developed. Wind velocity is the key variable that affects the transient operation of a horizontal axis wind turbine. However, typical vertical axis designs have a power coefficient that is highly variable throughout each rotor rotation. Techniques to predict this variable turbine output are developed in this thesis to supplement current methods to improve turbine operation, placement and design.

This thesis is organized into six chapters. A new analytical technique to predict the transient power coefficient of a Savonius VAWT is developed in Chapter 2. In Chapter 3, three techniques are formulated to predict the power coefficient. The formulations include an energy and exergy analysis that is used for predictions of both HAWTs and VAWTs. It also examines the transient rotor dynamics which is suited for

HAWTs, where the power coefficient does not significantly vary with rotor rotation, and a dimensionless investigation, particularly suited for VAWTs. The numerical model, presented in Chapter 4, is used to generate the results and analyze the various predictive techniques. Numerical simulations are an effective predictive tool, however, the long simulation times and computational storage can be impractical for a variety of applications. The results of the various predictive techniques, including the numerical simulations, are presented in Chapter 5. Each formulation is applied to various turbine designs. The model accuracy is demonstrated and the operating differences of turbine designs are identified. Chapter 6 summarizes the significant findings and conclusions. Future research pertaining to transient power coefficients is suggested. The tools developed in this research are shown to be useful for the development of small wind turbines.

Chapter 2

Analytical Formulation of Vertical Axis Wind Turbine Performance

In this chapter, a new analytical predictive technique is developed to forecast the performance of a Savonius style VAWT. The present model can predict the power coefficient at all rotor angles. Velocity fields are used with momentum theory to predict the transient forces on a Savonius rotor surface during operation. A scaling factor is applied to match the analytical and numerical results and increase the accuracy of the predictions.

2.1 Flow field and velocity vector estimation

In this section, the flow field formulation will be presented. It is assumed that the change of density of air as it flows through the turbine is negligible.

$$M_{sys} = \int_{sys} \rho \, d\forall \tag{2.1}$$

To predict the fluid motion, the Navier-Stokes equations are combined with the conservation of mass Equation (2.1) for a complete description of fluid motion.

$$\rho\left(\frac{\partial \boldsymbol{V}}{\partial t}+\boldsymbol{V}\cdot\boldsymbol{\nabla V}\right)=-\boldsymbol{\nabla}p+\rho\boldsymbol{g}+\mu\nabla^2\boldsymbol{V} \tag{2.2}$$

where g and μ represent the acceleration from gravity and dynamic viscosity of air, respectively. For a two-dimensional flow, the velocity field is described by

$$\boldsymbol{V}(x,y,t)=u(x,y,t)\hat{\boldsymbol{\imath}}+v(x,y,t)\hat{\boldsymbol{\jmath}} \tag{2.3}$$

The transient velocity of the fluid can be determined in terms of spatial coordinates. The *x* and *y* components of the velocity vector are represented by *u* and *v*, respectively. In two-dimensional form, the Navier-Stokes equations can be expressed as follows,

$$\rho\left(\frac{\partial u}{\partial t}+u\frac{du}{dx}+v\frac{du}{dy}\right)=-\frac{dp}{dx}+\rho g_x+\mu\left(\frac{d^2u}{dx^2}+\frac{d^2u}{dy^2}\right) \tag{2.4}$$

$$\rho\left(\frac{\partial v}{\partial t}+u\frac{dv}{dx}+v\frac{dv}{dy}\right)=-\frac{dp}{dy}+\rho g_y+\mu\left(\frac{d^2v}{dx^2}+\frac{d^2v}{dy^2}\right) \tag{2.5}$$

The complexity of the Navier-Stokes equations makes it difficult to obtain exact mathematical solutions for most real-world applications. In this section, the forces on a rotating rotor blade of a Savonius turbine are estimated by combining linear momentum theory and differential analysis of fluid flow.

For inviscid flow, the Navier-Stokes equations reduce to the Euler equation of motion,

$$\rho\boldsymbol{g}-\boldsymbol{\nabla}p=\rho\left(\frac{\partial \boldsymbol{V}}{\partial t}+\boldsymbol{V}\cdot\boldsymbol{\nabla V}\right) \tag{2.6}$$

In two-dimensional form, Eq. (2.6) can be expressed as

$$\rho g_x-\frac{dp}{dx}=\rho\left(\frac{\partial u}{\partial t}+u\frac{du}{dx}+v\frac{du}{dy}\right) \tag{2.7}$$

$$\rho g_y-\frac{dp}{dy}=\rho\left(\frac{\partial v}{\partial t}+u\frac{dv}{dx}+v\frac{dv}{dy}\right) \tag{2.8}$$

The left side of the Euler equation includes the force due to gravity and a pressure term. The first term can be eliminated since g_x and g_y are zero for a VAWT. Invisid flow also simplifies the pressure term. When the friction between fluid layers is negligible, the pressure is equal to the normal stress and independent of direction,

$$-p = \sigma_{xx} = \sigma_{yy} \tag{2.9}$$

The pressure acting on the rotor blades from the fluid flow through the turbine is an important part of the operational forces. The right side of Eq. (2.6) is the two-dimensional form of the continuity equation.

Further simplification is achieved by the incompressible flow assumption, thereby reducing the continuity equation to the following result

$$\boldsymbol{\nabla} \cdot \boldsymbol{V} = 0 \tag{2.10}$$

or

$$\frac{\partial u}{\partial x} + \frac{\partial v}{\partial y} = 0 \tag{2.11}$$

The Navier-Stokes equations become

$$\boldsymbol{V} \cdot \boldsymbol{\nabla V} = -\boldsymbol{\nabla} p \tag{2.12}$$

For predicting the operation of a Savonius turbine, the tangent to the velocity field is

$$\frac{dy}{dx} = \frac{v}{u} \tag{2.13}$$

This is defined as a streamline, obtained by integrating the velocity field. A second useful tool describes the line traced out by the motion of a fluid particle, defined as a pathline. For steady flow, the path followed by the particle will be equal to both the streamline and the pathline.

Connecting the velocity gradients and tangent lines with the use of the stream function, $\Psi(x, y)$, simplifies the problem complexity.

$$u = \frac{\partial \Psi}{\partial y} \qquad v = -\frac{\partial \Psi}{\partial x} \tag{2.14}$$

where the stream function satisfies the continuity equation. It can be used to plot the paths of constant Ψ. The application of Eq. (2.14) allows a family of streamlines to be determined to represent the fluid motion through the turbine. The Euler equation is a general form of Newton's second law, and it can be used to derive the Bernoulli equation along a streamline as follows [42],

$$\int \frac{dp}{\rho} + \frac{V^2}{2} + gz = constant \tag{2.15}$$

Applying the above formulation to the operation of a wind turbine, the freesteam can be represented by a uniform flow (i.e. $u = U \; and \; v = 0$). Additional effort is required to predict the complex streamlines through and around the Savonius turbine.

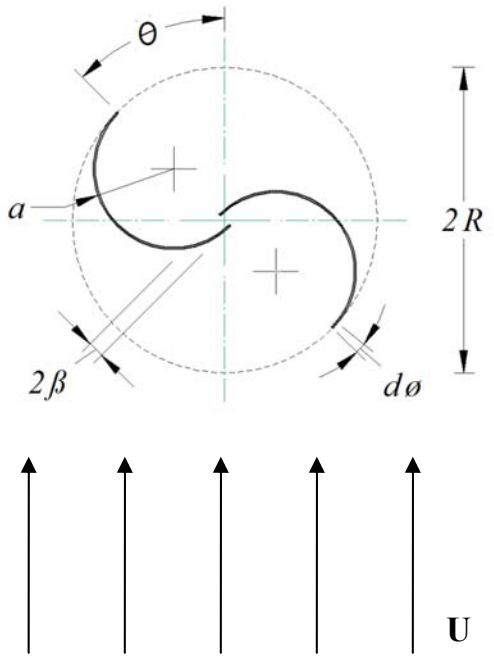

Figure 2-1 Geometrical variables of a Savonius VAWT

A cylindrical coordinate system is introduced to represent the rotor geometry within a velocity field, illustrated in Fig. 2.1. By expressing the velocity vector, $\boldsymbol{V}$, as

$$\boldsymbol{V} = v_r \hat{\boldsymbol{e}}_r + v_\phi \hat{\boldsymbol{e}}_\phi \tag{2.16}$$

where r is the distance from the rotor blade origin to the vector, and ϕ represents the cylindrical coordinate of surface relative to the origin of the cylindrical curve. The two-dimensional differential form of the continuity equation, for incompressible fluids, takes the following form:

$$\frac{1}{r}\frac{\partial(rv_r)}{\partial r} + \frac{1}{r}\frac{\partial v_\phi}{\partial \phi} = 0 \tag{2.17}$$

The stream function , $\Psi(r, \phi)$, can be represented as

$$v_r = \frac{1}{r}\frac{\partial \Psi}{\partial \phi} \qquad v_\phi = -\frac{\partial \Psi}{\partial r} \tag{2.18}$$

With this coordinate system, a new method to represent the turbine interaction with the air flow will be developed using a source sink pair. A source represents a location where the streamlines flow radially outward from a single point; conversely, with a sink, the flow is inward. The conservation of mass for this subsystem requires that the following mass balance is maintained:

$$(2\pi r)v_r = m \tag{2.19}$$

or

$$v_r = \frac{m}{2\pi r} \tag{2.20}$$

where m is the volume rate of flow per unit length. The sign of m establishes whether the point is a source or a sink (i.e. direction of v_r). To obtain the stream function, combine Eqs. (2.18) and (2.20), with $v_\phi = 0$ (since the flow is strictly radial for a source or sink), to yield

$$v_r = \frac{1}{r}\frac{\partial \Psi}{\partial \phi} = \frac{m}{2\pi r} \qquad v_\phi = -\frac{\partial \Psi}{\partial r} = 0 \tag{2.21}$$

and integrating to obtain

$$\Psi = \frac{m}{2\pi}\phi \tag{2.22}$$

Together, a source and sink pair can represent a variety of complex flow patterns. When the pair of equal strength is combined within a velocity field, the stream function becomes

$$\Psi = \frac{m}{2\pi}(\phi_1 - \phi_2) \tag{2.23}$$

where $\phi_1$and $\phi_2$represent the angles between the x-axis and an arbitrary point for a sink and a source, respectively. As the distance between the sink source pair approaches zero, the stream function can be represented by the following relation [42]:

$$\Psi = -\frac{k\ sin\ \phi}{r} \tag{2.24}$$

Combined with uniform flow, this doublet can be used to represent streamlines around a cylinder.

2.2 Analytical predictions of transient power coefficient

In this section, the superposition of a uniform potential flow and a doublet is extended to represent flow around a rotating cylindrical rotor blade, similar to a Savonius vertical axis wind turbine. These flow fields can be used to analyze the drag and lift forces caused by the pressure distributions along the rotor blade, throughout all angular positions during operation. The stream function can be expressed as

$$\Psi = \Psi_{uniform\ flow} + \Psi_{doublet} \tag{2.25}$$

where

$$\Psi_{uniform\ flow} = U\, r \sin\phi \tag{2.26}$$

and

$$\Psi_{doublet} = -\frac{K \sin\phi}{r} \tag{2.27}$$

The variables *U*, *r*, and ϕ represent the freestream velocity, the distance from the origin of the rotor radius, and the angular position of the blade surface (relative to the freestream and the origin of the blade curve). The constant *K* characterizes the strength of the doublet defined by ma/π, where *a* denotes the blade radius. If the flow separation caused by the viscous effects of the fluid are not fully represented, the flow around the cylindrical blade can be determined by $\Psi = constant$ for all $r = a$. After significant manipulation, it can be shown that the doublet strength is Ua^2 and the tangential velocity be represented as follows:

$$v_\phi = -\frac{\partial \Psi}{\partial r} = U\left(1 + \frac{a^2}{r^2}\right)\sin\phi \tag{2.28}$$

The pressure distribution on the convex surface of each blade can be obtained from the Bernoulli equation as follows,

$$p_0 + \frac{1}{2}\rho U^2 = p_s + \frac{1}{2}\rho v_{\phi_s}^2 \tag{2.29}$$

where the tangential velocity on a stationary blade surface is $v_{\phi_s} = -2U\sin\phi$. On the blade surface, $r = a$, reducing Eq. (2.28). Combining the reduced form of Eq. (2.28) with Eq. (2.29) results in

$$p_s = p_0 + \frac{1}{2}\rho U^2(1 - 4\sin^2\phi) \tag{2.30}$$

This equation predicts the pressure distribution along the convex side of a cylindrical blade surface.

The preceding analysis has not considered the rotor motion. The turbine rotation causes the control volume to rotate around a central axis, which changes the relative wind velocity at the rotor blades, at different values of θ. The wind velocity (parallel to the freestream) relative to the rotor blade can be defined as

$$W_x(\theta) = U_\infty + d\ \Omega \sin\theta \tag{2.31}$$

where Ω and U_∞ represent the rotor velocity and freestream wind speed, respectively. The variable *d* is the distance from the acting point of the force to the axis of rotation,

$$d(\theta) = \frac{1}{2}[(a-\beta) + a \sin\ 18.8°\ ]\ [1 - \sin\ (\theta/2)\ ] + [(a-\beta) + a \sin\ 35.6°\ ]\ \sin\ (\theta/2) \tag{2.32}$$

The magnitude of *d* is estimated from the location of flow separation on the blade, as follows.

The fluid particles travel along the streamlines, so the particle rotation is assumed zero. Streamlines are useful for describing inviscid fluid flow, but to accurately represent the viscous flow over a turbine blade, the frictional effects between the turbine and air stream must be considered. The combination of irrotational and boundary layer theory can more accurately represent the operation of a Savonius VAWT. According to the theory of boundary layer flow, the separation location is $\phi \approx 108.8° \approx 1.90$ radians [42]. The forces are estimated to act at the angle which centers between the front edge of the blade and the location of separation. One half of the linear distance (parallel to the freestream) from the origin to the location of flow separation can be estimated from

$$\mathrm{d}(0) = \frac{1}{2}[(a-\beta) + a \sin\ 18.8°] \tag{2.33}$$

The first two variables represent the distance to the center of the rotor, 90°, or one half of the rotor. The last term estimates the remaining distance to the location of flow separation. As illustrated in Fig. 2.2, at $\theta = 180°$, the magnitude of *d* can be represented by

$$d(180°) = [(a - \beta) + a \sin 35.6\,°\,] \tag{2.34}$$

which is equivalent to

$$d(180°) = \frac{1}{2}[(a - \beta) + a \sin\ 18.8\,°] + [(a - \beta) + a \sin 35.6\,°\,] - \frac{1}{2}[(a - \beta) + a \sin\ 18.8\,°] \tag{2.35}$$

or

$$d(\theta) = \tfrac{1}{2}[(a - \beta) + a \sin\ 18.8\,°] + \left\{[(a - \beta) + a \sin 35.6\,°\,] - \tfrac{1}{2}[(a - \beta) + a \sin\ 18.8\,°]\right\} \sin\ \left(\frac{\theta}{2}\right) \tag{2.36}$$

This equation is simplified to obtain Eq. (2.32).

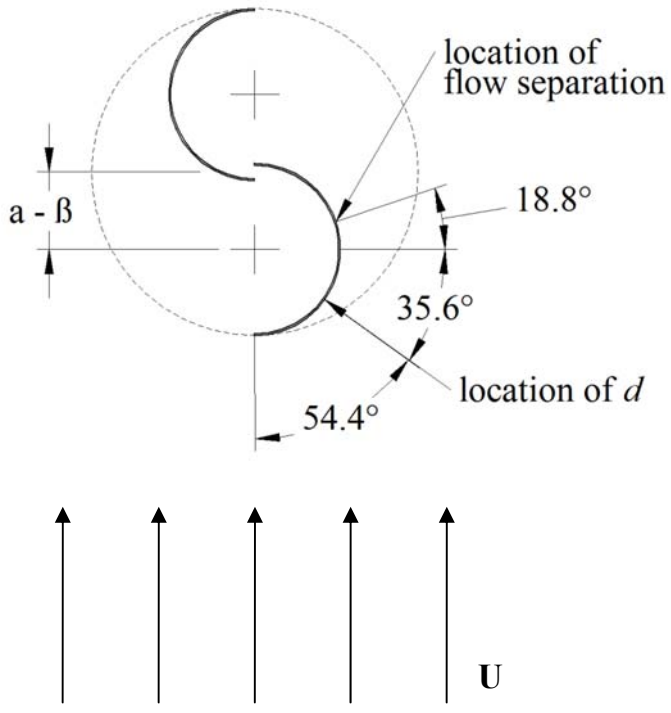

Figure 2-2 Location of *d* on a Savonius wind turbine

The preceding formulation can be used to predict the variations in pressure at different locations along the rotor surface, Eq. (2.30), combined with the relative wind speed, Eq. (2.31). The force induced by the pressure differential on a cylindrical Savonius blade can be predicted. The two-dimensional components of the pressure forces along the blade can be represented by the following equations,

$$F_{p,x} = -\int_{\xi_1(\theta)}^{\xi_2(\theta)} \left[p_0 + \frac{1}{2}\rho W_x^2 (1 - 4\sin^2\phi)\cos\phi \; a \right] d\phi \tag{2.37}$$

and

$$F_{p,y} = -\int_{\xi_1(\theta)}^{\xi_2(\theta)} \left[p_0 + \frac{1}{2}\rho W_x^2 (1 - 4\sin^2\phi)\sin\phi \; a \right] d\phi \tag{2.38}$$

where the integral limits are defined as $\xi_1(\theta) = 0 - \theta$ and $\xi_2(\theta) = \pi - \theta$, which correspond to the transient positioning of the rotor blade as it rotates around the central axis.

The ratio of the blade area to the rotor swept area of a turbine represents the degree to which the turbine behaves as a solid in the oncoming airstream. Characterized by the following relation,

$$S = \frac{ba}{R} \tag{2.39}$$

the solidity of a turbine corresponds to the blockage effect acting on the airstream. A Savonius turbine has a high solidity, representing operating conditions where the blockage is prominent. The air stream experiences a significant blockage effect as it flows into the turbine area. The mean average wind speed is slightly lowered in the area of the turbine, including the windward side, as illustrated by CFD predictions in Fig. 2.3 (to be discussed further in Chapter 5). As the air steam flows into the turbine rotors, there is a localized transfer of momentum (and velocity) from the air to the rotor blade.

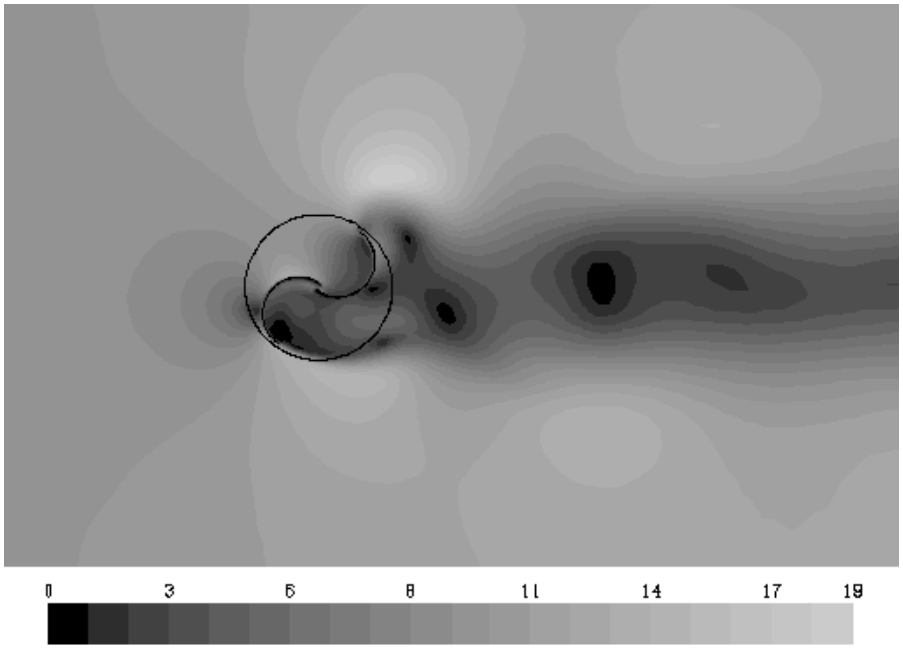

Figure 2-3 Velocity contours (m/s) of a Savonius wind turbine

Representing this momentum transfer can increase the accuracy of an analytical technique to predict a turbine with high solidity, as with a Savonius turbine.

The linear momentum equation is used to represent the effect of the air stream on the turbine blade. In its general form,

$$\frac{\partial}{\partial t}\int_{CV} \boldsymbol{V}\rho \, dV + \int_{CS} \boldsymbol{V}\rho\boldsymbol{V} \cdot \hat{\mathbf{n}} \, dA = \sum \boldsymbol{F}_{\substack{contents\ of\ the \\ control\ volume}} \tag{2.40}$$

The net rate of change in momentum across the control surface is represented by considering the change in linear velocity as the air flows into and out of the control volume. To represent a Savonius turbine, two independent stream tubes are considered: one for the power stroke, and another for the return stroke, respectively. Maintaining a constant control volume eliminates the first term of the linear momentum equation, expanded to represent the momentum force for a rotating Savonius blade as follows,

$$F_{x,m}(\theta) = \begin{cases} W_x \rho A W_x + W_x \rho A W_2 , & \text{if } 0 \leq \theta < \pi \\ -(W_x \rho A W_x + W_x \rho A W_x), & \text{if } \pi \leq \theta < 2\pi \end{cases} \quad (2.41)$$

The above equations assume that the air velocity decelerates from $U_\infty$to 0 as it strikes the rotor surface, at all values of θ. The exit velocity differs for the power and return strokes, which requires a piecewise function. The relative velocity of the fluid leaving the blade on the returning stroke, W_2, is defined as follows,

$$W_2(\theta) = -\sin\frac{\pi}{2} W_x \quad (2.42)$$

Here W_2 accounts for the angle at which the fluid is deflected by the convex curve ($-\sin\frac{\pi}{2}$). During the power stroke, the fluid is deflected by 180°, allowing W_x to also be used to represent the relative exit velocity during the power stroke. The area, A, is a function of θ to account for the changing cross section of the turbine blade, relative to the freestream, as it rotates about the central axis,

$$A(\theta) = a \cdot (1 + |\sin\theta|) \quad (2.43)$$

The torque (Q) on the blade can then be predicted from the following equation, which includes the lift and drag forces.

$$Q = d \cdot \left(F_{y,p}\cos\theta - F_{x,p}\sin\theta - F_{x,m}\right) \quad (2.44)$$

Finally, the power coefficient is determined by

$$C_P = C\frac{Q\Omega}{0.5\,\rho\,2(a-\beta)U^3}$$

or

$$C_P = C\frac{Q\Omega}{\rho\,(a-\beta)U^3} \quad (2.45)$$

where $2(a-\beta)$ is equal to the turbine radius, R, and the coefficient C is the formulation correction factor. Equation (2.45) is the standard representation of a turbine power

coefficient (i.e. $P = 0.5C_P\rho AV^3$) with the addition of the correction factor, C. Two aspects of the model accuracy are addressed with the correction factor, $C = C_1 \cdot C_2$. The coefficients C_1 and C_2 represent corrections to the aerodynamic forces acting on a single rotor blade, and the interaction between multiple rotor blades, respectively. The effects of C, including C_1 and C_2, are discussed further in Section 5.6.

Chapter 3

Performance Indicators for Wind Turbines

The performance of a wind turbine can be approximated from average values of the capacity factor and kinetic wind energy. More precise formulations of the predicted turbine efficiency can be used to improve performance through superior design methodologies and improved site selection. Transient forecasts of the power coefficient can improve performance by more effective control techniques and increased operating limits. In this chapter, the efficiency indicators and transient performance predictors will be developed.

3.1 Formulation of energy and exergy efficiencies

This section will establish the first law efficiency (η) and the second law efficiency (ψ). The energy efficiency is defined as the ratio of useful work to the difference in kinetic energy,

$$\eta = \frac{\dot{W}_{out}}{P} \tag{3.1}$$

where the power, *P*, is defined by Eq 3.6. The exergy efficiency refers to the ratio of useful work to the exergy of the wind as

$$\psi = \frac{\dot{W}_{out}}{\dot{E}x_{flow}} \tag{3.2}$$

In general, the energy balance equation for a wind turbine can be represented by

$$KE_1 = W_{out} + KE_2 \tag{3.3}$$

where *KE* is the kinetic energy of the flow stream and W_{out} is the useful work produced by the turbine. The equation describes the energy content of air as it passes through a two-dimensional plane. It is based on the kinetic energy of wind, which is

$$KE = \frac{1}{2}mV^2 \tag{3.4}$$

where *KE* is energy, *m* is mass, and *V* is the wind velocity. Rather than mass, a more convenient variable is volume (~~*V*~~), as related to mass by $m = \rho \cdot \not{V}$, where ρ is the density of air. The volume is expressed by the product of the cross-sectional area perpendicular to the wind (*A*) and the horizontal length of incoming wind (*L*). The horizontal length of incoming wind is then expressed as $L = \not{V} \cdot t$. This re-arrangement results in the more convenient following expression:

$$KE = \frac{1}{2}\rho AtV^3 \tag{3.5}$$

Since power is related to kinetic energy by $P = KE / t$, the above expression is more commonly used in the following form:

$$P = \frac{1}{2}\rho AV^3 \tag{3.6}$$

where *P* is the magnitude of power, ρ is the density of wind, *A* is the cross-sectional area perpendicular to wind, and *V* is the wind velocity. This expression describes the total

kinetic power of a wind stream. Kinetic energy is generally assumed to be the only source of energy captured by a wind turbine. It is used to establish wind power maps that are used for turbine placement and resource estimation. Although KE_1 can be readily determined from velocity measurements or predictions, many problems are associated with determining KE_2. The exit velocity from a wind turbine is difficult to measure, as it is highly variable and it quickly dissipates in all directions. As a result, empirical work outputs are generally required to determine the wind turbine efficiency (η).

Defining the axial induction factor (C_a) as the fractional reduction in wind velocity before and after the turbine,

$$C_a = \frac{V_1 - V_2}{V_1} \tag{3.7}$$

the power out can be estimated by the product of the thrust and the velocity at the turbine (refer to reference [42] for details)

$$P = \frac{1}{2}\rho\, A\, V^3 4\, C_a(1 - C_a)^2 \tag{3.8}$$

and

$$\eta = 4\, C_a(1 - C_a)^2 \tag{3.9}$$

Note that the axial induction factor, as defined above, is a key variable in the derivation of the Benz limit; which is determined by setting the derivative of Eq. (3.9) equal to zero, predicting a maximum efficiency at $C_a = 1/3$.

$$\eta_B = \frac{16}{27} \tag{3.10}$$

This is recognized as the theoretical maximum power output for a wind turbine, called the Benz limit.

The density of wind is most affected by temperature and relative humidity of the air. Temperature can be readily measured and computed. As a result, density is normally selected solely on this basis (i.e., $\rho\ (T)$, where T = air temperature). The air moisture content (ω) also affects wind density. A more accurate measure of density is $\rho\ (T, \omega)$. However, the effect is not significant, and is not commonly modelled in practice.

A second law analysis includes the flow irreversibilities associated with the system. The exergy balance equation can be expressed as

$$\dot{E}x_{flow,1} = \dot{W}_{out} + \dot{E}x_{flow,2} + \dot{E}x_{dest} \tag{3.11}$$

where $\dot{E}x_{dest}$ represents the exergy destruction associated with the process. It is a representative measure of the irreversibilities involved with the process. This methodology offers a useful alternative measure of turbine efficiency that includes the irreversibilities, which were not considered in the first law analysis. The exergy of flow, $\dot{E}x_{\text{flow}}$, can be defined as the maximum attainable work acquired as the air flows through the turbine [34]. The relevant terms include physical ($\dot{E}x_{ph}$) and kinetic exergy ($\dot{E}x_{KE}$),

$$\dot{E}x_{flow} = \dot{E}x_{ph} + \dot{E}x_{KE} \tag{3.12}$$

Physical exergy includes the enthalpy and entropy changes associated with the turbine operation, expressed as [40]

$$\dot{E}x_{ph} = \dot{m}\left[C_P h\ (T_2 - T_1) + T_0\left(C_P h \ln\left(\frac{T_2}{T_1}\right) - \mathrm{R}\ln\left(\frac{\mathrm{p}_2}{\mathrm{p}_1}\right) - \frac{C_P h\left(\mathrm{T}_0 - \mathrm{T}_{\text{average}}\right)}{\mathrm{T}_0}\right)\right] \tag{3.13}$$

where $p_i = p_0 \pm \frac{\rho}{2}V^2$. The first term in square brackets represents the change in flow enthalpy, while the second term characterizes the flow irreversibilities of the system. The

variables T_1 and T_2 are determined through the wind chill temperature (T_{windch}), based on a model developed by Zecher [43].

$$T_{windch} = 35.74 + 0.6215\,T - 35.75\,(V^{0.16}) + 0.4274\,T(V^{0.16}) \tag{3.14}$$

where the units of T_{windch} and V are °F and mph, respectively. By definition, the irreversibilities, I, associated with the system can be determined by [41]

$$I = T_0 \Delta S \tag{3.15}$$

or

$$I' = T_0 \left(C_P h \ln\left(\frac{T_2}{T_1}\right) - \mathrm{R} \ln\left(\frac{\mathrm{P}_2}{\mathrm{P}_1}\right) - \frac{\dot{m}\, C_P h \left(\mathrm{T}_0 - \mathrm{T}_{\mathrm{average}}\right)}{\mathrm{T}_0} \right) \tag{3.16}$$

where ΔS is the change in entropy and I' is the irreversibility rate. The kinetic component of the flow exergy is equivalent to the difference of kinetic energy through the turbine (i.e., ΔKE). From Eq. (3.3), the change in kinetic energy can also be expressed by the work output of the turbine. The specific exergy destruction can be defined as

$$ex_{dest} = \frac{T_0 \Delta S}{\rho A V} \tag{3.17}$$

The exergy methodology offers a significant opportunity to improve the wind turbine design and enhance the site selection by supplementing the information provided by the energy analysis.

3.2 Rotor dynamics correlation for maximum power and transient control

In this section, a new rotor dynamics model is developed for transient power output from a horizontal axis wind turbine. In addition to the standard maximum kinetic energy of the wind, the model incorporates rotor velocity and rotational acceleration to

enhance the control techniques that convert mechanical to electrical energy via shaft rotation. With current methods, the wind kinetic energy is generally the primary parameter that establishes maximum power output. By relating this wind energy to the rotor dynamics, electrical systems can have a more useful upper bound for the rotor control strategy. The new model predicts the rotor velocity for various turbine configurations, operating over a range of wind conditions. This approach offers the potential for higher accuracy when predicting fatigue stresses, transient operating conditions, and rotor control when converting mechanical to electrical energy.

The focus on rotor dynamics, involving angular velocity and acceleration allows a relationship to be developed between the wind velocity and turbine shaft rotation to enable controllers to predict and limit the imposed acceleration forces on the rotor dynamics. Incorporating this method into more complicated control strategies can create a balance between extracting the highest energy available from the wind, while limiting destructive acceleration forces within the turbine rotors and mechanical systems. The acceleration forces experienced by a turbine are dependent on the wind characteristics at its installed location, as well as the design, materials and operating principals of the turbine itself. This innovative method of including the rotor dynamics can be used to predict the unique acceleration forces that are imposed for an individual site specific analysis. For example, in a study on the implications of seasonal and diurnal variations of wind velocity for power output estimation of a turbine [44], the authors reported that time of day variations need to be reported to accurately assess the economic viability and reliability of the installation. However, including limitations imposed on the operation due to rotor acceleration could improve the model's estimation of dependability, refining the economic potential predictions of individual installations.

The generality of the following model allows it to be integrated into mathematical formulations of HAWT performance used to evaluate design parameters and predict turbine capacity. For example, the axial fan theory was applied to a HAWT to predict an optimum pitch angle and chord length of the turbine blade. The method was shown to be useful in predicting the applied lift and drag forces developed on the rotor blades [45]. However, this method does not fully represent the acceleration forces developed at each section of the rotor blade. Considering the acceleration in the design of the turbine could be used to linearize the difference in the acceleration forces throughout the blade. This has the potential to limit destructive forces within the turbine blade when operating in fluctuating wind conditions.

Wind power systems are typically characterized by the turbine's efficiency when capturing the kinetic energy of the wind. A conventional approach for predicting the wind kinetic energy uses the following equation:

$$P = \frac{1}{2} C_P \rho A V^3 \tag{3.18}$$

where C_P, ρ, and A represent the turbine power coefficient, air density, and rotor swept area, respectively. This predicted capacity of the turbine indicates the optimal amount of power. However, the C_p value of the turbine is dependent on shaft speed of the turbine and it is highly variable with changing wind speeds. The system should be controlled to operate at the optimal shaft rotation at any particular wind speed. This rotor control can be inferred from experimental power curves involving the variable tip speed ratio (λ), a dimensionless ratio of rotor velocity ($\dot{\theta}$), rotor radius (R) and wind velocity (V), as follows,

$$\lambda = \frac{\dot{\theta} R}{V} \tag{3.19}$$

The stochastic properties of wind flow across the rotor are highly variable and not fully represented by this approach. This section will develop a new model that uses the rotor rotational velocity and acceleration to predict and control the turbine power output. This will allow better performance through new insight into the turbine's operation.

The following new model includes the rotational behaviour of the blades to predict the maximum turbine power output and efficiency. The angular kinetic energy of the rotor can be written as

$$KE = \frac{1}{2} J \dot{\theta}^2 \tag{3.20}$$

where J and $\dot{\theta}$ represent the radial moment of inertia and velocity, respectively. Differentiating this expression yields

$$y = \frac{d(KE)}{dt} = \frac{d(J\dot{\theta}^2 / 2)}{dt} = J\dot{\theta}\ddot{\theta} \tag{3.21}$$

The power output (y) indicates the rotational dynamics of the wind turbine. Substituting Eq. (3.19) and $A = \pi R^2$ into Eq. (3.18), yields

$$y = P = \frac{1}{2} C_p \pi \rho \mathrm{R}^5 \frac{\dot{\theta}^3}{\lambda^3} \tag{3.22}$$

Rearranging Eq. (3.21) and substituting Eq. (3.22) yields the following single state dynamical system for the rotor power,

$$\ddot{\theta} = \frac{C_p \pi \rho \mathrm{R}^5}{2J\lambda^3} \dot{\theta}^2 \tag{3.23}$$

Equation (3.23) depends on the rotational input parameters and predicts the corresponding rotor acceleration. This equation assumes the wind velocity is constant throughout the

rotor swept area, a potential source of error that could limit the model to smaller turbines or steady flow conditions, where the difference in velocity, is negligible throughout the rotor disk.

Using the correlation by Manwell et al. [46], the shaft torque is given by

$$Q = \int \frac{1}{2} \rho c V_{rel}^2 br \left(C_L \sin\varphi - C_D \cos\varphi \right) dr \tag{3.24}$$

In this equation, c, V_{rel} and b represent the airfoil chord length, relative velocity, and number of blades, respectively. This equation is a result of blade element theory, where the torque arises from a tangential force acting at a distance r from axis of rotation. The coefficients of lift (C_{L}) and drag (C_{D}) and the angle of relative wind (φ) are the other variables in the equation. The relative velocity at the rotor tips can be expressed as

$$V_{rel} = V\left(1 - \frac{\dot{\theta} R}{V} \right) \tag{3.25}$$

Substituting Eq. (3.25) into Eq. (3.24) and simplifying,

$$Q = \int \frac{1}{2} \rho cbr \left(C_L \sin\varphi - C_D \cos\varphi \right) \left(V - \dot{\theta} R \right)^2 dr \tag{3.26}$$

Furthermore, the rotor kinetic energy and torque can be related by equating Eqs. (3.20) and (3.26),

$$\frac{1}{2} J \dot{\theta}^2 - \int \frac{1}{2} \rho cbr \left(C_L \sin\varphi - C_D \cos\varphi \right) \left(V - R\dot{\theta} \right)^2 dr = 0 \tag{3.27}$$

This result provides a useful new correlation that relates the wind and rotor velocities; a useful utility for applying Eq (3.23) to obtain predictions of HAWT performance with transient wind velocities. The preceding formulation has an important utility for predicting and effectively controlling the rotor dynamics to capture the maximum wind

power from a time-varying air stream. Sample results will be presented for this new formulation in Section 5.4.

3.3 Power correlation for vertical axis wind turbines with varying geometries

In this section, another analytical formulation is presented to predict another aspect of performance of a vertical axis wind turbine (VAWT). The model differs from other past techniques, as it can predict C_p with changes in both tip speed ratio (λ) and various geometrical variables. It will be shown that the model can provide good accuracy for Savonius type VAWTs. The new dimensionless correlation will provide a valuable design tool that can be extended to other types of turbines for predicting a turbine's performance over a range of operating conditions. The new model includes four primary variables, as well as five geometrical variables. These variables are reduced to include the power coefficient (C_p) and λ.

A dimensional analysis with the Buckingham-Pi theorem will be developed as follows. Based on extensive empirical and field test data, the power output from a wind turbine, in terms of the tip speed ratio, can be correlated in the following general functional form,

$$C_p = a \cdot (\lambda)^2 + b \cdot (\lambda) + c \tag{3.28}$$

where a maximum C_p is achieved at a unique tip speed ratio for each turbine design. This maximum is constant, regardless of wind speed (see Fig. 3.1). In practice, the power coefficient depends on additional design and flow variables. Experimental data that are

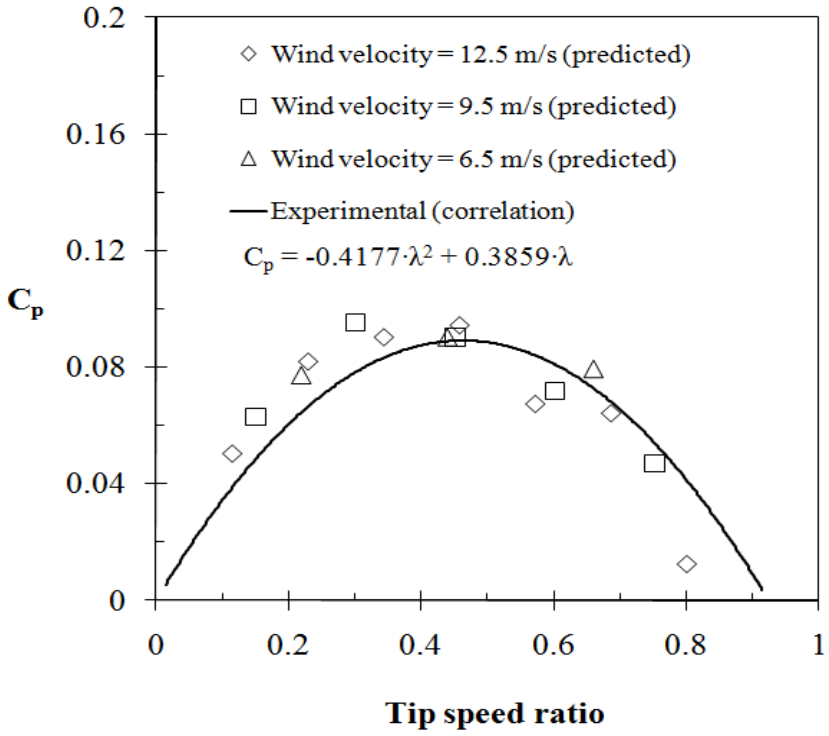

Figure 3-1 Power curve for the Zephyr vertical axis wind turbine (note: experimental data of Hunt and Savory, 2006)

correlated with respect to dimensionless variables can be used to develop convenient correlations that summarize the main trends resulting from complicated flow fields. For example, Wang et al. [47] showed that experimental data of droplet flow impingement on a wind turbine airfoil will collapse consistently onto a single normalized correlation of Nu / $Pr^{1/3}$ at varying Prandtl numbers. Furthermore, it was shown that the functional form of the Hilpert correlation can effectively accommodate measured data for a wind turbine airfoil over a range of Reynolds numbers [48]. This section describes a method whereby geometrical variables are combined with C_p and λ to produce a power coefficient correlation that reduces the complexity of analysis and helps facilitate practical design and development of VAWTs.

Consider a specific design represented by the Zephyr VAWT (see Fig. 3.2a). Nine key variables are identified to represent the turbine power output (P) for different stator geometries. The variables include the rotor velocity (Ω), rotor radius (R), freestream velocity (V), air density (ρ), turbine height (H), turbine width (W), stator spacing (σ), and stator angle (θ_s) (see Fig. 3.2b). The power output depends on these variables as follows: $P = f(\rho, V, R, H, W, \sigma, \theta_s, \Omega)$. Dimensions of these variables can be represented by the

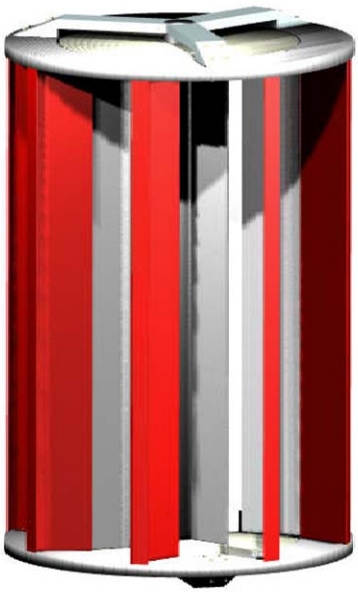

(a)

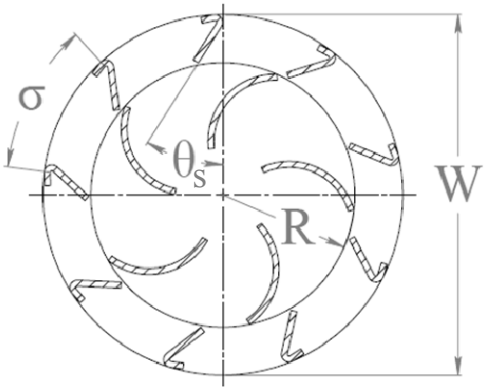

(b)

Figure 3-2 Zephyr vertical axis wind turbine (a) illustration and (b) geometrical variables

base dimensions of mass (M), length (L), and time (T), as follows: $P \equiv M^1 \cdot L^2 \cdot T^{-3}$, $\rho \equiv M^1 \cdot L^{-3} \cdot T^0$, $V \equiv M^0 \cdot L^1 \cdot T^{-1}$, $R \equiv M^0 \cdot L^1 \cdot T^0$, $H \equiv M^0 \cdot L^1 \cdot T^0$, $W \equiv M^0 \cdot L^1 \cdot T^0$, $\sigma \equiv M^0 \cdot L^1 \cdot T^0$, $\theta_s \equiv M^0 \cdot L^0 \cdot T^0$, $\Omega \equiv M^0 \cdot L^0 \cdot T^{-1}$. From these nine variables and three dimensional units, the Buckingham-Pi theorem [42] states that six dimensionless Pi terms will be sufficient to represent and predict the turbine's performance. The reference variables, ρ, V and R, lead to the following three Pi variables, as determined by the Buckingham-Pi theorem:

$$\Pi_1 = \frac{P}{\rho \cdot V^3 \cdot R^2} \tag{3.29}$$

$$\Pi_2 = \frac{R}{H} \tag{3.30}$$

$$\Pi_3 = \frac{R}{W} \tag{3.31}$$

Combining these three terms results in the following power coefficient (C_p); $C_p = 2 \cdot \Pi_1 \cdot \Pi_2 \cdot \Pi_3 = \frac{P}{1/2 \cdot \rho \cdot H \cdot W \cdot V^3}$. The fourth and fifth Pi terms are additional terms for representing changes in the stator geometry.

$$\Pi_4 = \frac{\sigma}{R} \tag{3.32}$$

$$\Pi_5 = \theta_s \tag{3.33}$$

The last Pi term is represented in terms of R, Ω, and V. It is equivalent to the variable tip speed ratio (λ), a common dimensionless parameter for wind power analysis.

$$\Pi_6 = \lambda = \frac{R \cdot \Omega}{V} \tag{3.34}$$

These terms are then combined such that $2 \cdot \Pi_1 \cdot \Pi_2 \cdot \Pi_3 = \xi(\Pi_4, \Pi_5, \Pi_6)$, which can be reduced to

$$C_p = \xi \cdot \left(\frac{\sigma}{R}, \theta_s, \lambda \right) \tag{3.35}$$

where ξ will be determined through numerical predictions with CFD (Computational Fluid Dynamics). This expression will lead to correlations that provide useful insight about the turbine's geometric characteristics. It will provide helpful information for design considerations and power improvements.

Chapter 4

Numerical Formulation of Wind Turbine Operation

Numerical simulations are performed with the commercial software FLUENT 6.3.26 to represent the operation of a variety of wind turbine designs. These simulations will provide useful predictions of turbine performance. The solution domain and mesh discretizations are generated with GAMBIT 2.4.6 software. A rotating reference frame and a sliding mesh are included in the solution formulations to represent the motion of the turbine rotor blades. The governing equations, boundary conditions, and solution formulation will be discussed in this chapter.

4.1 Governing equations of fluid flow

The governing equations are the incompressible form of the Navier-Stokes equations [49]. The conventional and most widely employed solution approach for turbulence modeling involves time averaging. As a consequence of this averaging, a number of turbulent stresses are introduced into the solution, so equations must be defined to represent these terms. As a result of the approximations needed to solve the

equations, many models have been developed. Each offers unique advantages for the particular parameters for which it was developed [50]. A rotating frame adaptation of the governing Navier-Stokes equations will be used in this thesis. The governing equations for fluid flow include the conservation of mass (Eq. 4.1) and momentum equations (Eq. 4.2). The conservation of momentum contains two acceleration terms that represent the rotation. These include the Coriolis acceleration, defined as $2\vec{\omega} \times \vec{v}_r$, and the centripetal acceleration described by $\vec{\omega} \times \vec{\omega} \times \vec{r}$.

$$\frac{\partial \rho}{\partial t} + \nabla \cdot \rho \vec{v}_r = 0 \tag{4.1}$$

$$\frac{\partial}{\partial t}(\rho \vec{v}_r) + \nabla \cdot (\rho \vec{v}_r \vec{v}_r) + \rho(2\vec{\omega} \times \vec{v}_r + \vec{\omega} \times \vec{\omega} \times \vec{r}) = -\nabla p + \nabla \overline{\overline{\tau}}_r + \vec{F} \tag{4.2}$$

In these equations, $\vec{r}$ is the radial position from the origin of the rotating domain, $\vec{\omega}$ is the angular velocity of the rotor domain, $\vec{v}_r$ is the relative velocity, p is the static pressure, $\bar{\bar{\tau}}$ is the stress tensor and $\vec{F}$ represents the external body forces [49]. A mixed formulation of cylindrical and Cartesian coordinates will be adopted, in order to simulate the two separate regions of the domain, i.e., rotating rotor-stator section and external incoming flow, respectively.

The standard k - ε model, Eqs. (4.3) and (4.4), are used to simulate turbulence in the flow field [49]. They are coupled to the Navier-Stokes equations though the convection terms. This is a widely used model that provides reasonable accuracy and a robust ability to represent a wide range of flow regimes. It is a two-equation model that includes turbulent kinetic energy, k, and dissipation rate, ε, as follows,

$$\frac{\partial}{\partial t}(\rho k) + \frac{\partial}{\partial x_i}(\rho k u_i) = \frac{\partial}{\partial x_j}\left[\left(\mu + \frac{\mu_t}{\sigma_k}\right)\frac{\partial k}{\partial x_j}\right] + G_k + G_b - \rho\varepsilon - Y_M + S_k \tag{4.3}$$

$$\frac{\partial}{\partial t}(\rho\varepsilon)+\frac{\partial}{\partial x_i}(\rho\varepsilon u_i)=\frac{\partial}{\partial x_j}\left[\left(\mu+\frac{\mu_t}{\sigma_\varepsilon}\right)\frac{\partial\varepsilon}{\partial x_j}\right]+C_{1\varepsilon}\frac{\varepsilon}{k}(G_k+C_{3\varepsilon}G_b)-C_{2\varepsilon}\rho\frac{\varepsilon^2}{k}+S_\varepsilon \quad (4.4)$$

In this model, G_k represents the generation of turbulence kinetic energy due to mean velocity gradients, G_b describes the generation of turbulence kinetic energy due to buoyancy, and Y_m represents the contribution of the fluctuating dilatation to the overall dissipation rate. The variables σ_k and σ_ε are the turbulent Prandtl numbers for k and ε, with values of 1.0 and 1.3, respectively. The constants $C_{1\varepsilon}$ and $C_{2\varepsilon}$ are $C_{1\varepsilon}$ = 1.44 and $C_{2\varepsilon}$ = 1.92. The turbulent (or eddy) viscosity, μ_t, is computed by combining k and ε such that

$$\mu_t=\rho C_\mu\frac{k^2}{\varepsilon} \quad (4.5)$$

where C_μ is a constant 0.09 [49]. These equations will be used to predict air flow through the turbine and subsequently improve its performance.

The turbulence model requires the turbulence intensity and turbulence viscosity ratio to be used for turbulence estimation. The turbulence intensity (i) is defined as the ratio of the root-mean-square of the velocity fluctuation (u') to the mean freestream velocity (u_{avg}), described by Eq. (4.6). The turbulence viscosity ratio is defined as the ratio of turbulent viscosity (μ_t) to molecular viscosity (μ) in Eq. (4.7).

$$i\equiv\frac{u'}{u_{avg}} \quad (4.6)$$

$$\text{Turbulent Viscosity Ratio}\equiv\frac{\mu_t}{\mu} \quad (4.7)$$

A turbulence intensity of 10% is assumed at the velocity inlet [51] and the turbulent viscosity ratio is assumed to be 1, to represent external flows [42]. At the outlet, a backflow turbulence intensity of 12% is assumed to account for the increased turbulence

created by the turbine interaction [52]. The backflow turbulence viscosity ratio is also assumed to be 1.

4.2 Boundary conditions

The velocity at the inlet is specified as a constant. The mass flow rate into the solution domain (see Fig. 4.1) is calculated by

$$\dot{m} = \int \rho \vec{v} \cdot d\vec{A} \tag{4.8}$$

where $\dot{m}$ is the mass flow rate. The air density is a constant 1.225 kg/m^3. The face pressure (p_f) is resolved from the boundary condition of the pressure outlet used to represent the exit boundary of the solution domain. The face pressure at each cell is calculated from Eq. (4.9), while other conditions are extrapolated from the interior of the solution domain [49].

$$p_f = 0.5(p_c + p_e) \tag{4.9}$$

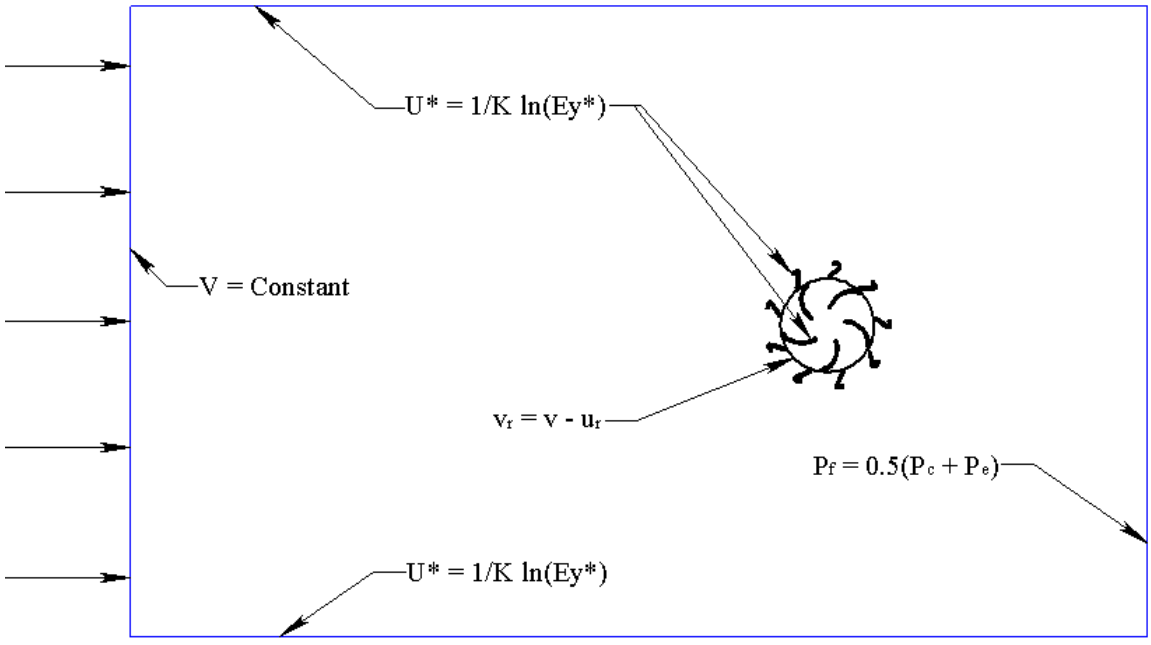

Figure 4-1 Boundary conditions for numerical predictions

In this equation, p_c is the interior cell pressure neighbouring the exit face, and p_e is the pressure at the exit, assumed as standard atmospheric pressure of 101,325 Pa.

The standard wall functions U^* are used to represent the stator walls, rotor blades, and outer boundary walls in the solution. The law-of-the-wall [49] for the mean velocity yields

$$U^* = \frac{1}{K}\ln\left(Ey^*\right) \tag{4.10}$$

such that

$$U^* \equiv \frac{U_P C_\mu^{1/4} k_P^{1/2}}{\tau_\omega / \rho} \tag{4.11}$$

$$y^* \equiv \frac{\rho C_\mu^{1/4} k_P^{1/2} y_P}{\mu} \tag{4.12}$$

where E is an empirical constant equal to 9.793, K is the von Kármán constant (K = 0.4187), U_p is the mean velocity of the fluid at point P, k_p is the turbulent kinetic energy at point P, y_p is the distance from point P to the wall, and μ is the dynamic viscosity of air (1.7894×10^{-05} kg/m-s).

The SIMPLE algorithm is used for pressure-velocity coupling to enforce the conservation of mass and obtain the pressure field. Other features of the solution parameters include a second order implicit unsteady formulation and a second order upwind scheme for turbulent kinetic energy and turbulence dissipation rate predictions. This numerical formulation will be used to predict air flow through the turbine and subsequently improve its performance. Significant features of the rotating solver are summarized below:

- Finite volume method with a segregated solver;

- Standard k - ε turbulence model ;
- Standard wall functions for near-wall treatment;
- Air density is constant as 1.225 kg/m^3;
- Air viscosity is constant as 1.7894×10^{-5} kg/m-s;
- Backflow turbulence intensity as 12%;
- The velocity inlet is used for the velocity specification method;
- Wall roughness height as 0;
- Pressure-velocity coupling characterized with the SIMPLE algorithm;
- Turbulence kinetic energy and turbulence dissipation rate represented by second order upwind schemes.

4.3 Rotor rotation

The operation of a wind turbine is highly dependent on the rotor rotation and it must be represented for accurate predictions of turbine performance to be obtained. Two independent models will be used in this thesis to represent the rotation of the rotors, specifically, (i) MRF (multiple reference frame) and (ii) sliding mesh formulations.

In the MRF formulation, the solution domain is divided into two subdomains (see Fig. 4.2 for sample mesh discretization). For the stator and surrounding domain, a stationary reference frame is used. The rotor's reference frame rotates at a rotational velocity $\vec{\omega}$, with respect to the stationary frame. To represent the flow across the interface between the subdomains, continuity of the absolute velocity is enforced to provide the appropriate values of velocity for each subdomain [49]. Fluid computations across the subdomain interface are represented by

$$\vec{v}_r = \vec{v} - \vec{u}_r \tag{4.13}$$

where

$$\vec{u}_r = \vec{\omega} \times \vec{r} \tag{4.14}$$

Here $\vec{u}_r$ is the velocity due to the moving frame, also known as the whirl velocity, and $\vec{r}$ is the position vector from the origin of the rotating frame.

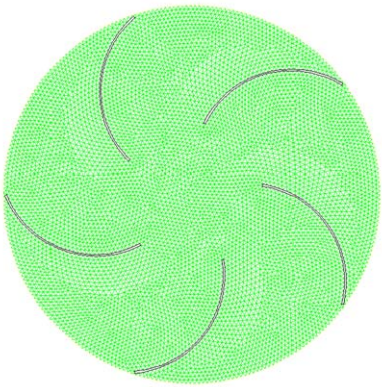

(a)

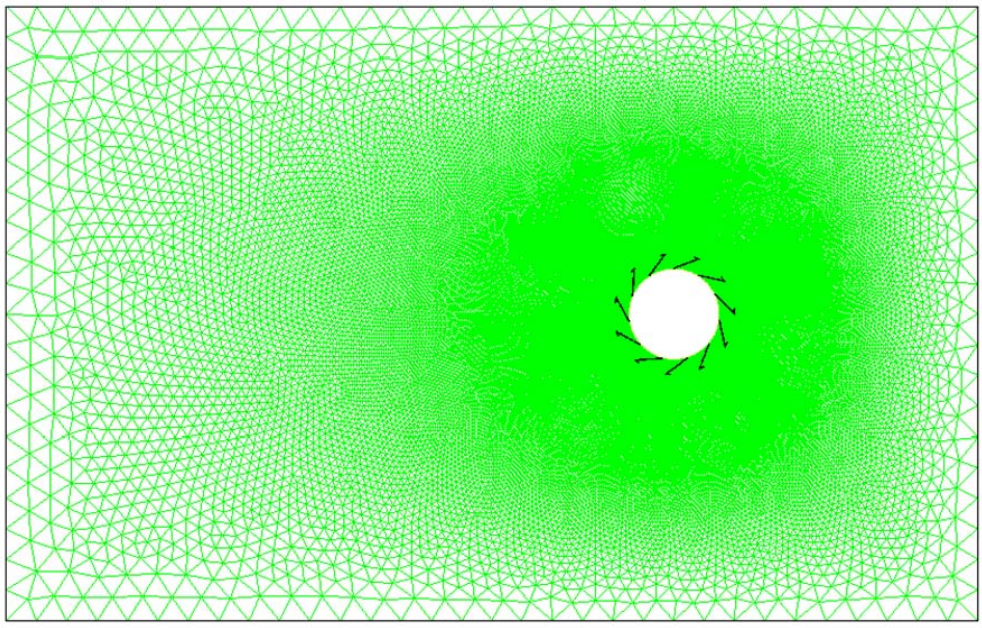

(b)

Figure 4-2 Sample 2-D mesh discretization of VAWT (a) rotor and (b) stator, together with surrounding subdomain

The use of a sliding mesh is a powerful tool for simulating flows with rotating fields. For this model, the overall domain is divided into two subdomains. The rotor subdomain rotates with respect to the stationary stator subdomain. This formulation allows cells adjacent to the boundary between the subdomains to slide relative to one another, thus allowing for transient predictions of the rotor interaction with the flow field, created by the stationary stator blades. To provide the appropriate values of velocity for each subdomain, a continuity of absolute velocity is enforced at the boundary. This formulation requires that the flux across the boundary between subdomains is computed with the cell faces at the boundary misaligned. Thus, new interface zones are determined at each timestep. Each cell face is converted to an interior zone. The resulting overlap between opposing interior faces produces a single interior zone. Therefore, the number of faces at the boundary will vary with each timestep [51]. The sliding mesh formulation offers increased accuracy over the MRF formulation, but with higher computational expense.

Chapter 5

Results and Discussion

In this chapter, the results of the predictive formulations are presented. Several case studies are examined to illustrate the model capabilities and estimate the error associated with each formulation. Section 5.1 examines the potential of greenhouse gas reduction with vertical axis wind turbines (VAWTs) in urban centers. Four different wind turbine designs are compared, in terms of greenhouse gas reduction and specific energy distribution of the wind energy resource. The numerical results, discussed in section 5.2, are used in the other sections to compare the various formulations and predict the transient power coefficient.

5.1 Potential carbon dioxide mitigation from Toronto urban wind power

Increasing wind power utilization will mitigate CO_2 emissions by reducing the reliance on fossil fuel energy production and the subsequent releases that come from the combustion of these fuels [53]. Due to the large environmental costs associated with these pollutants, many concerns have risen about the use of coal. For example, pressures are rising to close the remaining coal fired power plants in Ontario, which supply approximately one quarter of the Province's power. Although climate change emissions

are the main concern, there is also evidence linking 660 premature deaths and 1,100 emergency room visits each year to coal fired power plant emissions [54]. In this section, the residential wind power potential in Toronto will be discussed.

Toronto is home to about 4,753,000 people with numerous commercial and business wealth resources [55]. Currently, the wind power in the city center is limited to a few isolated installations. There is significant potential for CO_2 mitigation from wind power in Canadian cities. Canadians are among the worst per capita contributors to CO_2 emissions at 18.3 tonnes per year [56]. This is despite the vast ability for renewable power generation. Currently, 59% of Canada's 592,008 GWh total generated electricity is generated from hydroelectric power; 349,469 GWh per year. This is coupled with numerous other resources such as solar, wind, nuclear, tidal, and geothermal. Still, Canada relies on steam power plants, with coal as the primary fuel, for 20%, or 118,252 GWh of power [57]. CO_2 emissions of these plants are about 0.96 kg per kWh of generated power [58]. Furthermore, gas turbines, typically burning natural gas, are used for 4.4%, or 25,810 GWh of power [57]. The CO_2 release from natural gas is about 0.54 kg/kWh [58].

Limiting the use of fossil fuels will reduce the CO_2 emitted during power generation. A typical coal fired power plant contributes approximately 19% of Canada CO_2 emissions from power generation. Natural gas contributes 3.5% of Canada's CO_2 emissions from power generation. In total, Ontario generation is 30,199 GWh from steam power plants and 5,524 GWh from gas turbines. In contrast, wind power, which has zero emission operation, is used for 144,467 MWh of power generation in Ontario [57]. The main attributes of Ontario's power production methods are summarized in Table 5.1.

Table 5-1 Attributes of Ontario's power production and carbon dioxide pollution [53, 57]

Utilities and industries	**Primary fuel**	**Energy production**	**Contribution to total [%]**	**CO_2 footprint [kg_{CO2}/kWh**
Steam	coal	30 199 278	19.1	0.96
Gas turbine	natural gas	5,523,736	3.5	0.54
Wind	n/a	144 467	0.091	0.003 to 0.025
Total	n/a	158,023,212	100	≈0.202

Figure 5.1 compares the specific energy distributions of five different wind turbines, for one year. This figure uses wind data from RETSCREEN software [59], based on monthly average wind speeds for Toronto, Canada. A Weibull distribution, Eq. (5.1), is assumed for the wind velocity distribution, i.e. *p(V)* [60].

$$p(V) = \frac{k_w}{s}\left(\frac{V}{s}\right)^{k_w - 1} \exp\left[-\left(\frac{V}{s}\right)^{k_w}\right] \tag{5.1}$$

where k_w represents the shape parameter. A low value of k_w represents wind conditions that can be characterized by an exponential decay function, where a high value of k_w

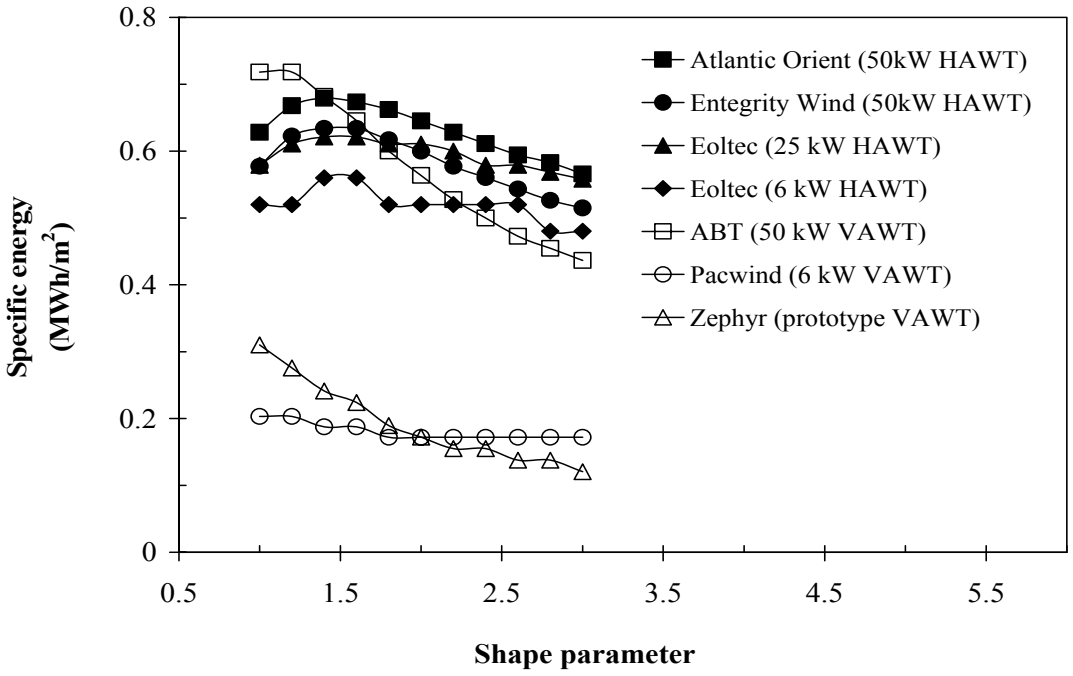

Figure 5-1 Specific energy with changes in wind distribution for various wind turbines

represents conditions that approach a normal distribution. The variable s is the scaling factor, determined analytically by [61]

$$s = \frac{\overline{V}}{\Gamma\left(1+1/k_w\right)} \tag{5.2}$$

The commercial turbines in Fig. 5.1 are the Atlantic Orient 50 kW HAWT [62], Entegrity Wind Systems (50 kW HAWT) [63], Eoltec (6 kW HAWT) [64], Eoltec (25 kW HAWT) [65], Air Breeze Technologies (ABT) (50 kW H-type VAWT) [66], and the PacWind (6kW Savonius VAWT) [67]. The characteristic curve unique to each turbine, including cut-in and cut-out limits, along with the calculated wind probability functions, are used to calculate the specific power coefficients. The ABT VAWT displays a common feature among Darrieus turbines, whereby they have a lowered cut in speed compared to HAWTs. These VAWTs have particular advantages when the wind speed distributions have a low shape factor. Such sites coincide with wind speed distributions that approach an exponential decay function. At such conditions, a VAWT can achieve a significantly higher capacity factor than a HAWT. This opposes the high values of k_w that approach a normal distribution of wind velocities about the mean wind speed, where the HAWT design is favoured. There is a relatively low efficiency shown by the drag type turbines (Pacwind and Zephyr VAWTs) in Fig. 5.1. The advantages of drag machines need to be better utilized, while the disadvantages need to be further reduced for them to make a significant contribution to the wind energy market. Numerical predictions [68] for the Zephyr Vertical axis Wind Turbine (ZVWT) are included in the plot. The comparison suggests that the Zephyr stator cage improves the Savonius performance in wind conditions that are represented by a low value of k_w in the Weibull distribution, conditions where Savonius turbines can already offer a significant advantage.

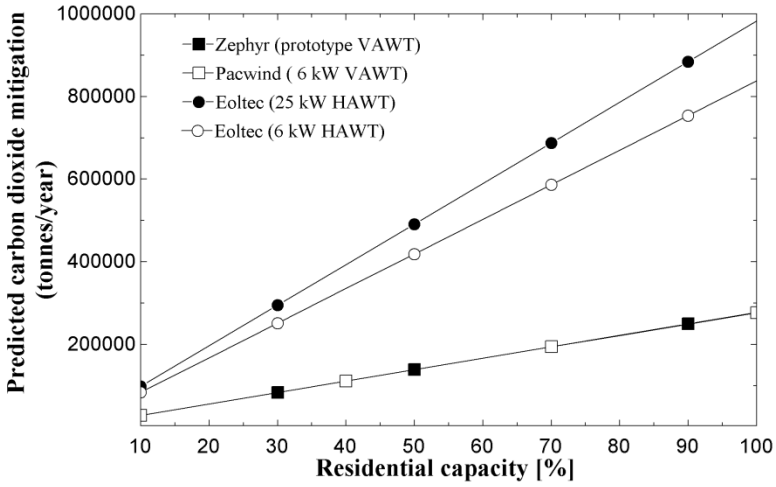

Figure 5-2 Predicted carbon dioxide mitigation with residential capacity

Toronto had about 1,765,000 private dwellings in 2006, with 1,678,536 occupied by residents [55]. There is a significant potential to mitigate CO_2 emissions from residential urban wind power in Toronto. Figure 5.2 illustrates the quantity of CO_2 mitigation that could be achieved from small wind power installations in Toronto's private dwellings. The analysis assumes that each installation captures one square meter of wind power. Linear scaling is assumed for each turbine. In this plot, the predicted mitigation for the drag type designs (Zephyr and Pacwind) are nearly identical. In comparison to VAWTs, a substantially higher amount of CO_2 mitigation is suggested from HAWT installations. However, this does not account for the adverse operating conditions of urban installations. The power production and resulting CO_2 mitigation from an urban HAWT would be substantially reduced, as the turbine would not perform properly in the turbulent wind conditions.

Figure 5.3 compares the mitigated CO_2 pollution based on two different assumptions about the displaced energy. In particular, the energy produced from the urban wind power displaces the energy from (i) coal fired power plants, and (ii) a

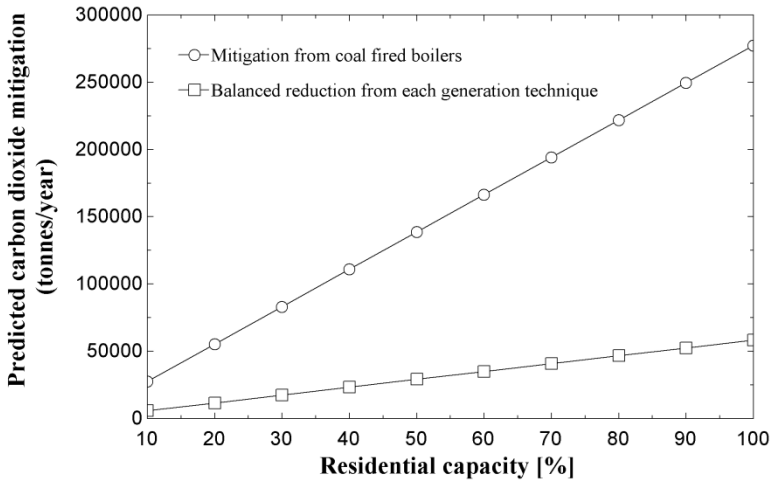

Figure 5-3 Predicted carbon dioxide mitigation with variations in residential capacity

balanced reduction is achieved in all energy generation techniques. In the first scenario, the analysis assumes that the energy generated from the residential urban wind power will reduce CO_2 emissions by 0.96 kg per kWh of generated power. In the second scenario, the relative quantities of power generation for the various technologies in Toronto are considered equal to that of Ontario. Here, the relative CO_2 mitigation from gas turbines and coal fired plants are included in the calculation. The product of the carbon released from coal fired power plants (0.96 kg/kWh) and the relative amount of use (19.1% of total power generation in Ontario) gives the relative carbon footprint from coal. Similarly, the relative natural gas carbon footprint is calculated from its carbon release (0.54 kg/kWh) and its relative use (3.5%). The summation of these two relative carbon footprints estimates the carbon footprint mitigation for the second scenario. These two extreme cases give useful predictions of the range of actual CO_2 mitigation, as it would likely occur between these two cases. From the figure, significant CO_2 mitigation can be achieved from residential urban wind power. For example, if 50% of the private dwellings occupied by usual residents installed a one square metre capacity VAWT, the

city could mitigate between 29,193 and 138,741 tonnes of carbon dioxide pollution. This could have a worthwhile impact on climate change action, while offering significant leadership and market penetration for this important cause.

In the results, the CO_2 emissions from the manufacturing, installation, and maintenance of these turbines were excluded. This would lower the potential carbon mitigation. However, the residential urban potential does not include various other potential urban sites, including commercial and entertainment buildings, parks, street lights, and many other locations. A full life cycle analysis would be beneficial to further investigate the potential of urban wind power to mitigate CO_2 pollution.

5.2 Numerical prediction of power coefficients

In this section, the results of numerical simulations for specific wind turbines are presented. These predictions are used as a benchmark for other predictive techniques presented in the following sections. Four systems are numerically investigated; two airfoils commonly used for horizontal axis wind turbines [69, 70] and two VAWTs (Savonius and Zephyr) operating under low quality wind conditions (see Figs. 2.1 and 3.2). These include (i) a NACA 63(2) - 215 airfoil developed by the National Advisory Committee for Aeronautics (NACA) and (ii) the Wortmann FX 63 - 137. The VAWTs include (iii) a conventional Savonius design and (iv) a more complex Zephyr VAWT prototype. A numerical model for each system is developed for the fluid flow analysis. Computational Fluid Dynamics software, FLUENT [49], is used to predict the operation of each system. These numerical models will offer insight into the fluid flow characteristics for each of the different turbines. Data gained from the numerical predictions are used to examine the various formulations discussed in Chapters 3 and 4.

For the airfoils, $\dot{W}_{out}$ will be determined by the model of Wilson et al. [71]. This is an empirical technique that correlates the turbine power coefficient with the lift (C_L), drag (C_D), number of blades (B), and tip speed ratio (λ).

$$C_P = \left(\frac{16}{27}\right)\lambda\left[\lambda + \frac{1.32 + \left(\frac{\lambda - 8}{20}\right)^2}{B^{\frac{2}{3}}}\right]^{-1} - \frac{(0.57)\lambda^2}{\frac{C_L}{C_D}\left(\lambda + \frac{1}{2B}\right)} \tag{5.3}$$

The lift and drag coefficients are estimated from numerical predictions obtained at the specified tip speed ratio and blade number. For the VAWTs, $\dot{W}_{out}$ is determined from the product of a numerically predicted torque and the simulated rotational velocity.

(i) System 1: NACA 63(2) - 215 Airfoil

As presented in Figure 5.4a, the NACA 63(2) - 215 airfoil is a conventional design that creates lift with low wind speeds, making it suitable for use in wind turbine blades [69, 70]. Throughout the following analysis, the approach angle (φ), i.e. the angle between the airsteam and the rotor blade, is estimated to be 10˚. The incoming components of velocity are V_x = 9.85 m/s and V_y = 1.74 m/s. The X and Y direction of the force vectors for the lift and drag components become X_L = -sin(10°) = -0.174, Y_L = cos(10°) = 0.985, X_D = cos(10°) = 0.985, and Y_D = sin(10°) = 0.174, respectively. Table 5.2 summarizes the system assumptions used in the numerical analysis.

Table 5-2 System parameters

	V_1 [m/s]	Radius [m]	Area [m^2]	W_{out}	$W_{out,2}$
NACA 63(2)-215 airfoil	10	1	$\pi \times 1^2$	$f(C_L,C_D)$	ΔKE
FX 63-137 airfoil	10	1	$\pi \times 1^2$	$f(C_L,C_D)$	ΔKE
Savonius VAWT	10	1	1.0^2	$f(Q, \lambda)$	ΔKE
Zephyr VAWT	10	0.762	0.762^2	$f(Q, \lambda)$	ΔKE

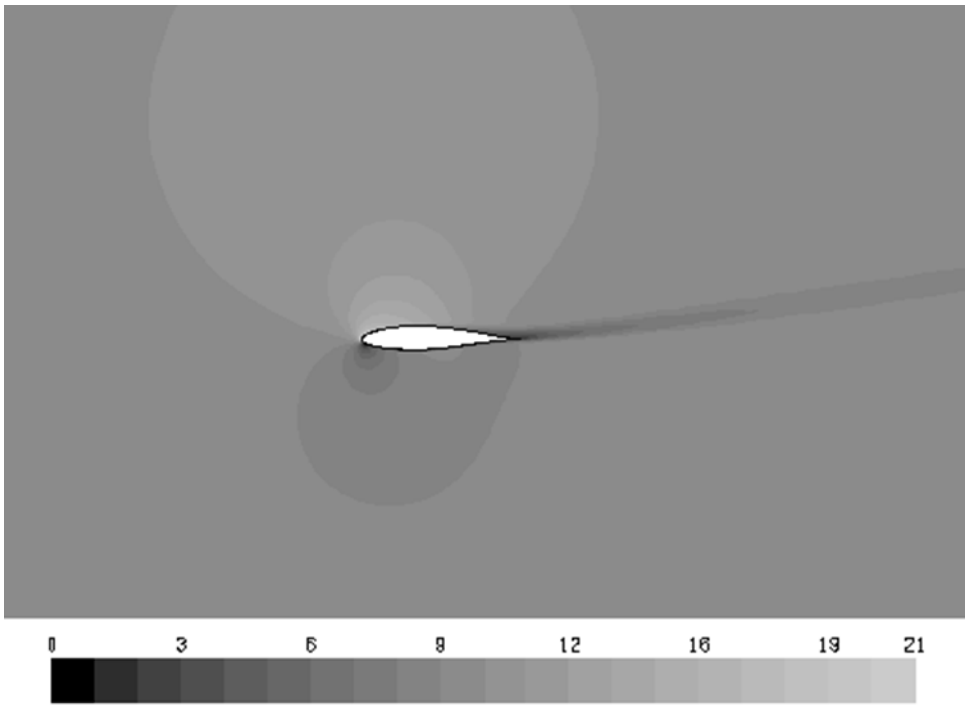

(a)

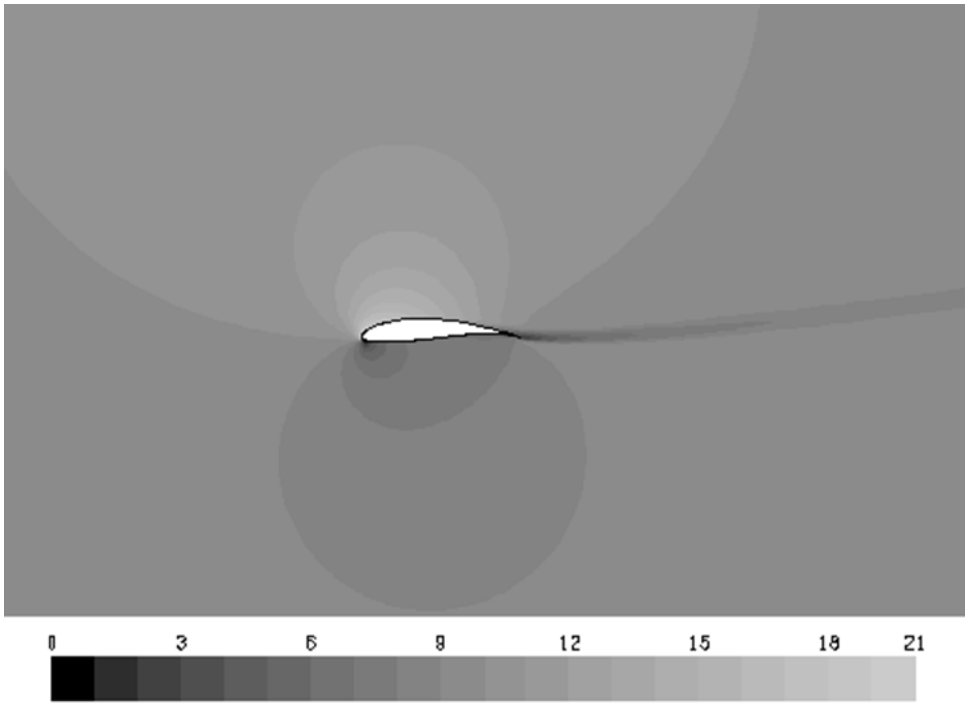

(b)

Figure 5-4 Contours of velocity magnitude (m/s) for (a) NACA 63(2)-215 and (b) FX 63-137 airfoils

The profile of the NACA 63(2) - 215 airfoil is discretized with a structured quadrilateral cell scheme. The mesh is refined from an average cell edge length of 260 mm at the outer region, to 14 mm at the airfoil surface. Refined to a total of 12,150 cells, with an average cell size of 0.061 m^2, produces results that are independent of further grid refinement [41]. The governing equations are the incompressible form of Navier-Stokes equations. The standard k - ε model is used to simulate turbulence in the flow field. This is a widely used model that provides reasonable accuracy and a robust ability to represent a wide range of flow regimes [49]. The features of the airfoil solver are summarized below:

- Finite volume method with a segregated solver;
- Standard k - ε turbulence model;
- Standard wall functions for near - wall treatment;
- Air density is constant as 1.225 kg/m^3;
- Air viscosity is constant as 1.7894×10^{-5} kg/m-s;
- Backflow turbulence intensity as 12 %;
- The velocity inlet is used for the velocity specification method;
- Inlet x-velocity as 9.85 m/s;
- Inlet y-velocity as 1.74 m/s;
- airfoil roughness height as 500 μm;
- Pressure-velocity coupling characterized with the SIMPLE algorithm;
- Turbulence kinetic energy and turbulence dissipation rate represented by second order upwind schemes.

(ii) System 2: FX 63 - 137 Airfoil

This airfoil has been examined widely in past literature. Its characteristics will be used to investigate the aerodynamic behaviour of wind turbines [69, 70]. In comparison to other common wind turbine airfoil profiles, this design provides a relatively complex configuration. The pronounced tail curvature provides a substantial contrast to System 1 that will be evaluated, as illustrated in Fig. 5.4b.

The same solver features, including the governing and turbulence equations, as with System 1, i.e. NACA 63(2) - 215, are used for this system. Variations in airfoil surface roughness are presented in Fig. 5.5. Convergence in both lift and drag coefficients are evident after 250 μm. For both airfoils, a C_L / C_D ratio are used for the power coefficient predictions with a roughness height of 500 μm. The mesh is refined from an average of 289 mm at the outer region, to 0.014 mm at the airfoil surface. It is refined to 12,195 cells, with an average cell size of 0.061 m^2.

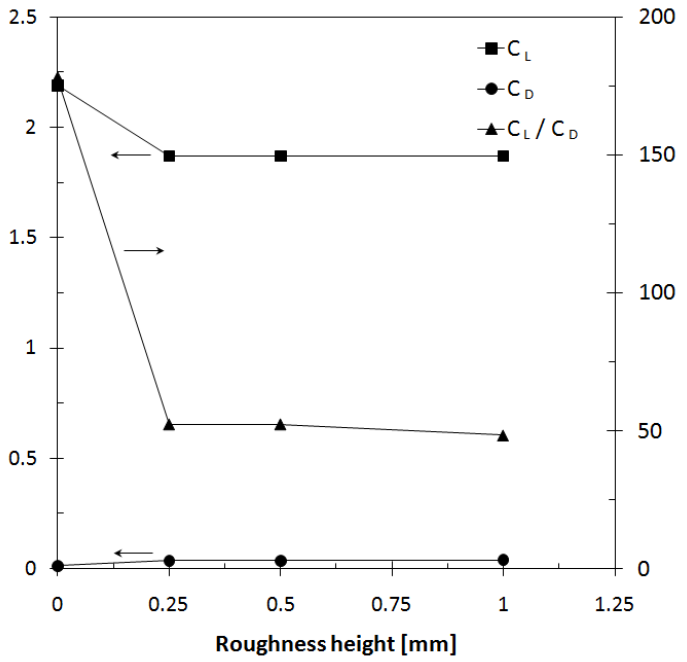

Figure 5-5 Airfoil performance with variable surface roughness

(iii) System 3: Savonius VAWT

The Savonius VAWT is a common design that is capable of reaching substantial efficiencies. A basic semicircular design will be used, with a 10% overlap; see Figs. 2.1 - 2.3. The domain is discretized into 13,693 cells with an average cell size of 0.019 m^2. The mesh is refined from 500 mm at the boundary, to 50 mm at the rotor surface. The same governing and turbulence equations, as for previous cases, will be used for this system. However, considerable differences in some solver features are required. A transient mesh formulation is used to simulate the rotor motion. A timestep size of 0.0209 seconds is simulated, resulting in 50 timesteps per revolution. The numerically predicted average moment induced on the rotor blades will be used to determine the power coefficient. The wall roughness height is assumed negligible, and the incoming velocity is simulated to be V_x = 10 m/s and V_y = 0.

(iv) System 4: Zephyr VAWT

As illustrated in Figs. 3.2 and 5.6, the Zephyr turbine represents a more complex VAWT. The features of this turbine allow it to perform in both low wind and high turbulence conditions. Thus, several turbines can operate in close proximity of each other in urban areas. The maximum power coefficient of this turbine is relatively low, in comparison to other systems. However, it is an ideal candidate to operate in low quality winds and offers a good contrast to the Savonius VAWT and airfoil HAWT systems. The stator subdomain is discretized with an edge length of 191 mm at the exterior, which is gradually refined to an edge length of 6.35 mm at the rotor. This yields approximately 117,000 cells, with an average area of 217 mm^2, see Fig. 4.2. At this resolution, the results become independent of grid spacing [68]. The analysis of this system employs the

same solver features, including the governing and turbulence equations, as the Savonius VAWT.

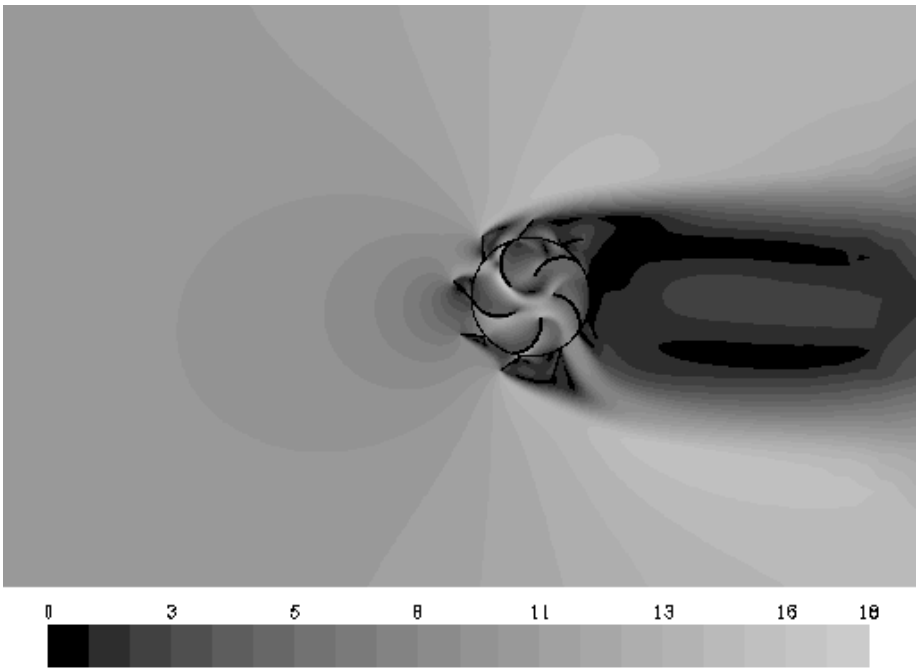

Figure 5-6 Zephyr VAWT velocity contours shaded by velocity magnitude (m/s)

With the multiple reference frame formulation, only one position of the rotor relative to the stator is simulated. The design of this turbine suggests that there is a relatively high degree of rotor-stator interaction. However, this problem is overcome by rotating the stator relative to the wind direction three times for each of the geometries and taking the average of the results. Figure 3.1 presents a range of predicted C_p (calculated by the average of three MRF predictions) at three different wind speeds. Also, an experimental correlation obtained by Hunt and Savory [72] is illustrated for the identical turbine design. The experimental correlation was obtained through a series of wind tunnel tests on a full scale VAWT prototype, with this particular correlation obtained at a

Reynolds number range of 80,000 - 100,000. This close agreement exhibited by the past experimental results provides useful validation of the predictions.

5.3 Energy and exergy efficiencies of horizontal and vertical axis wind turbines

In this section, a comparison of exergy efficiencies for the four different wind power systems will be presented. The analysis is intended to compare turbines that have different performance advantages in various operating conditions with a single parameter. A parametric study investigates the selection and associated predictions of key variables for each system. This section will also examine an exergy analysis of wind power for potentially valuable utility in the wind energy industry. The numerical simulations are used to obtain performance predictions of the various wind systems and provide useful information about the fluid flow behaviour. For the airfoils, the numerically predicted coefficients of lift and drag are used to determine the maximum power coefficient through Eq. (5.3). The inlet velocity is taken as 10 m/s. A numerically predicted moment coefficient is used to determine the power coefficient of the VAWTs. The results of the numerical study are summarized in Table 5.3.

Table 5-3 Problem parameters and predictions

	λ	p_0 [kPa]	T_0 [°C]	C_L	C_D	C_M	C_p
NACA 63(2)-215 airfoil	4	101.3	25	1.15	0.0385	-	0.44
FX 63-137 airfoil	4	101.3	25	1.87	0.0357	-	0.47
Savonius VAWT	0.8	101.3	25	-	-	0.0294	0.18
Zephyr VAWT	0.5	101.3	25	-	-	0.0147	0.11

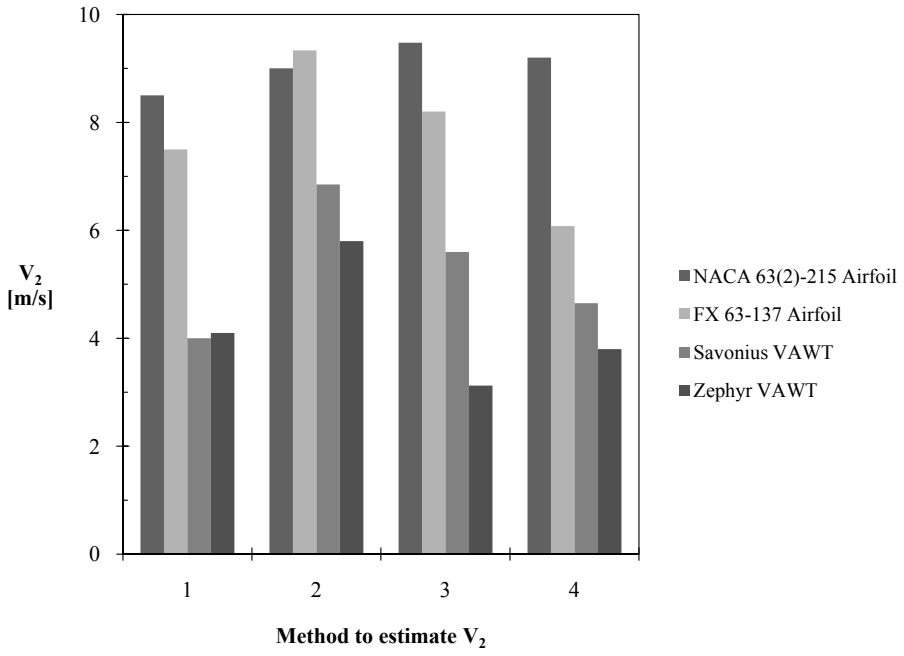

Figure 5-7 Methods to estimate V_2 for a variety of wind power systems

A standard metric for finding V_2, i.e., the exit velocity when applying Eq. (3.14), is crucial for maintaining consistent exergetic efficiency predictions for different wind turbine designs and operating conditions. Four different methods for estimating V_2 are presented. Each method is investigated with respect to its reference variables and operating conditions. The exergy predictions from each method are compared with the energy predictions and discussed with regards to accuracy. The ability to represent the performance of different turbine designs and operating conditions with a standard metric is a significant value of the second law. Four methods of estimating V_2 are presented below (see Fig. 5.7),

- Method 1: Point specific, low wind velocity (measured one chord behind the turbine);
- Method 2: Specific effective velocity ($V_2 = V_{2,\text{eff}} \times A_{\text{eff}} / A$);

- Method 3: Average velocity of useful area ($V_2 = V_{2,\text{useful, ave}}$);
- Method 4: Average of the low velocity stream.

A parametric study of the reference conditions and operating wind conditions will be presented for each of the four wind energy systems. The results will be compared for each method of estimating V_2. This includes (i) point specific low velocity, (ii) specific effective velocity, (iii) average velocity of useful area, and the (iv) average of the low velocity stream.

(i) Method 1: Point specific, low wind velocity (measured one chord behind the turbine)

Method 1 is advantageous because it can be determined in a consistent manner for different designs. Also, this method lends itself well to physical measurements. Virtually identical values of V_2 are predicted for the VAWTs, with similar values also suggested for the airfoils. The resultant airfoil second law efficiencies are 15% and 17% for the NACA 63(2) - 215 and FX 63 - 137, respectively. A 51 - 50% distinction between the first and second law efficiencies is predicted for the airfoil designs. A different trend is observed for the VAWTs. The second law efficiency for the Savonius VAWT is predicted to be 17%, a 6% difference from the first law predictions. Comparably, a 10% exergy efficiency, which is 9% different than the first law predictions, is obtained for the Zephyr VAWT.

Results of the energetic and exergetic analysis using Method 1 for determining V_2 are presented in Figs. 5.8 and 5.9a - 5.13a. Variations in the reference conditions P_0 and T_0 are presented in Figs. 5.9a and 5.10a, respectively. The minor effects of altering P_0 are included in the first law efficiencies for the VAWTs, but they do not affect the

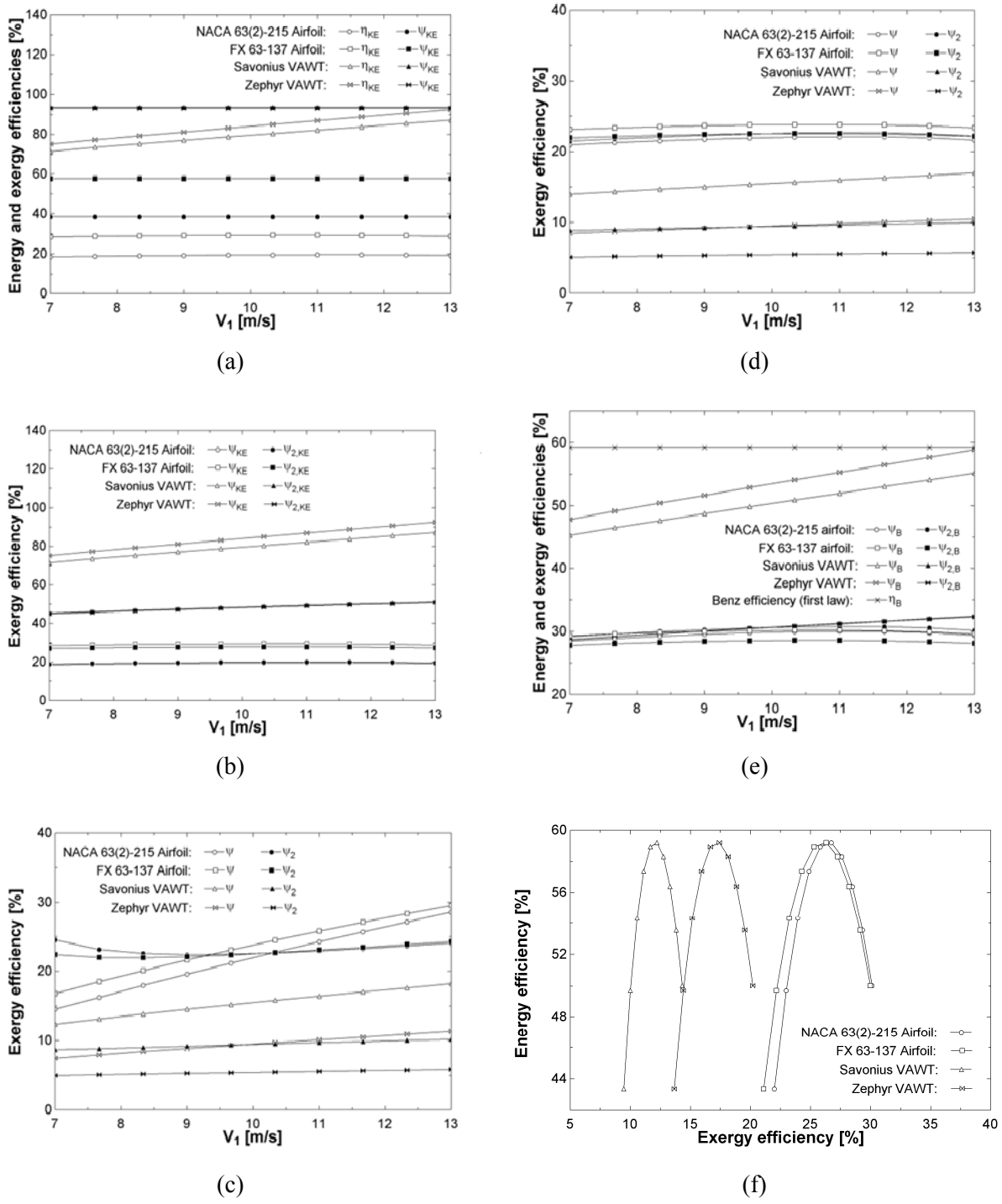

Figure 5-8 Energy and exergy efficiencies based on (a) kinetic energy, (b) flow exergies, (c) V_2 maintained constant, (d) V_2/V_1 maintained constant , (e) Benz efficiencies and (f) induction factor

airfoils. The discrepancy is caused by the method of determining $\dot{W}_{\text{out}}$, or more specifically, the power coefficient. The analysis of the airfoils uses an empirical correlation, which is independent of the reference pressure. In contrast, for the energy analysis, the VAWT predictions include the effects of local pressure on the local wind density, when predicting the power coefficient. The plot of varying reference temperature includes the majority of the standard operating conditions, with an equal distribution from 25 ˚C, standard reference temperature. Similar to the variable p_0, it can be observed that although the second law efficiencies depend on the choice of reference conditions, it allows different wind power systems to be compared with one descriptive parameter. A

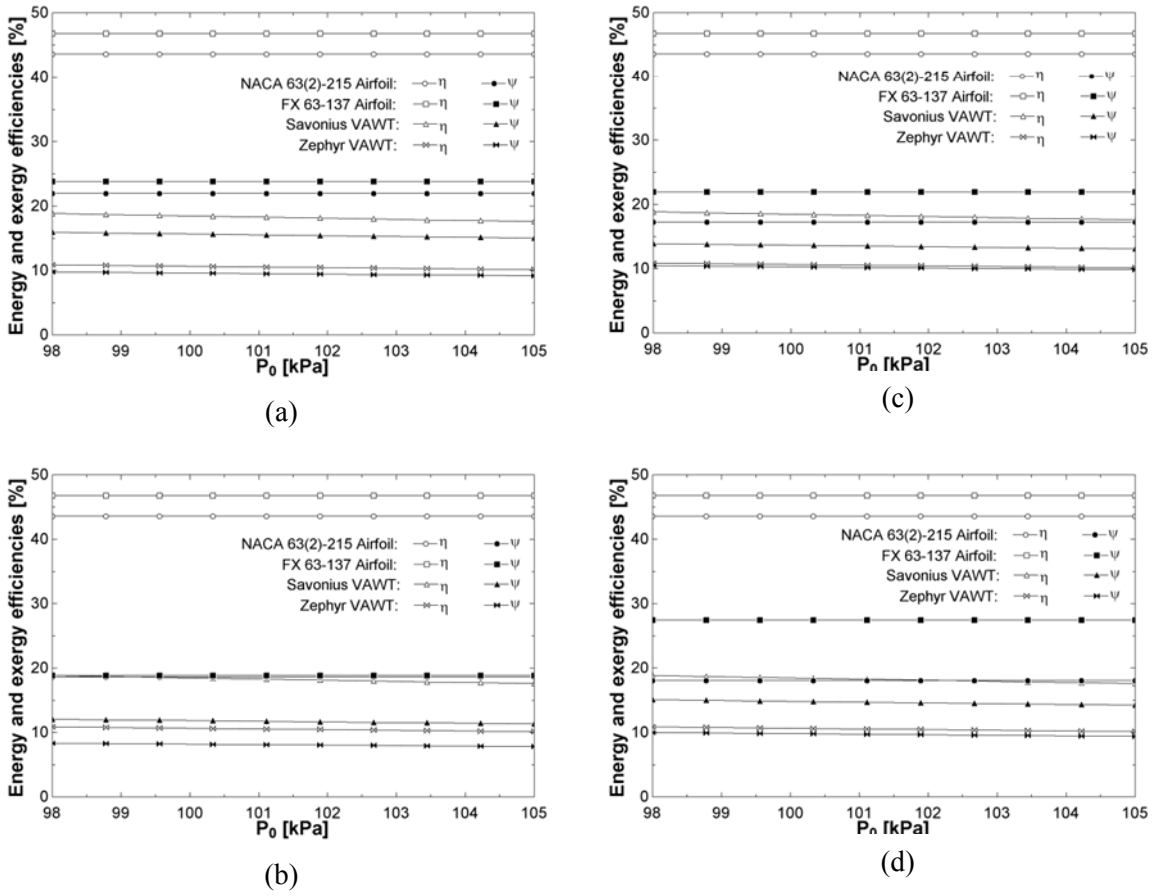

Figure 5-9 Energy and exergy efficiencies with varying pressure for (a) point specific low velocity, (b) specific effective velocity, (c) effective velocity and (d) average low velocity

summary of the variables used in the figures is provided below.

- η is the energy efficiency
- η_B is the maximum efficiency as defined by the Benz limit
- η_{KE} is the energy efficiency with 100% of the kinetic energy change converted to useful work
- ψ is the exergy efficiency with $Ex_{flow} = E_{shaft} + C_p \mathrm{h}\,\Delta T + T_0 \Delta S$
- ψ_2 is the exergy efficiency with $Ex_{flow} = \Delta \mathrm{KE} + C_p \mathrm{h}\,\Delta T + T_0 \Delta S$
- ψ_B is the maximum efficiency defined by the Benz limit and the second law
- ψ_{KE} is the exergy efficiency with 100% of the kinetic energy change converted to useful work

Variations to the input velocity, V_1, are presented in Figs. 5.11a and 5.12a. These figures illustrate the effects of variations of inlet velocity, while comparing the

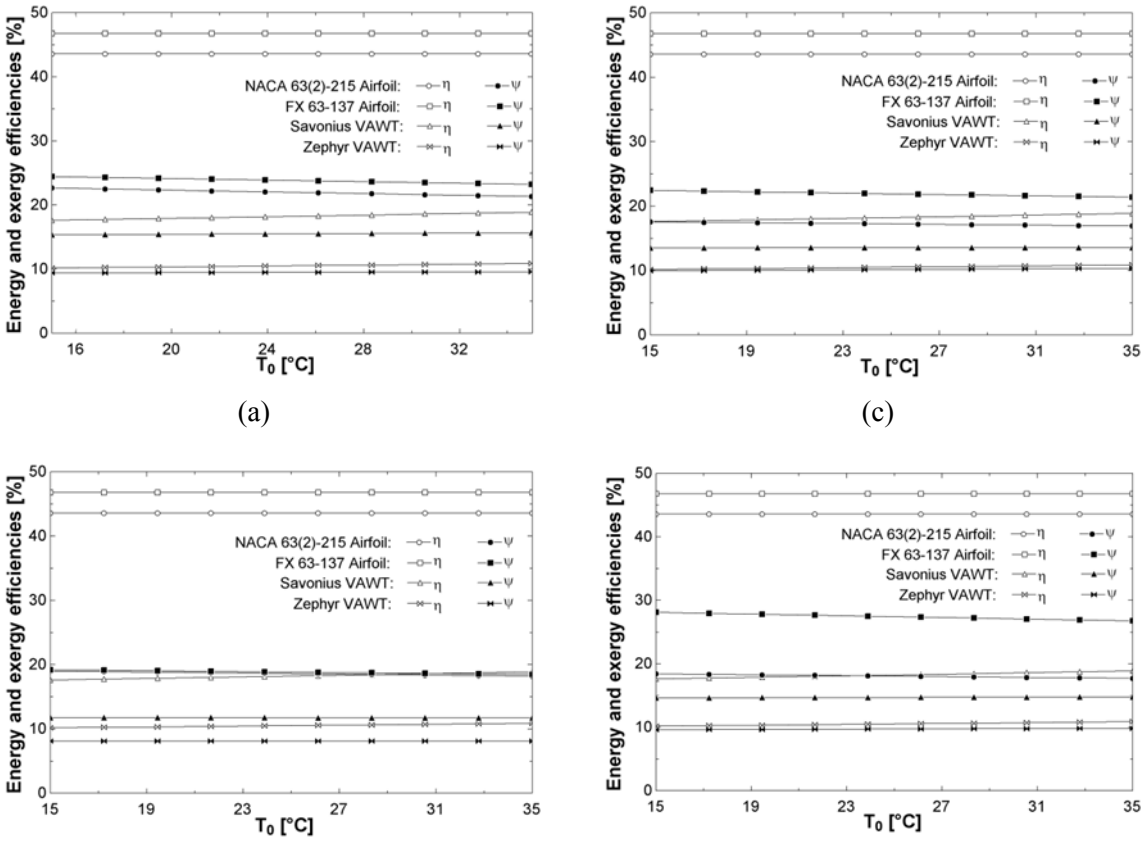

Figure 5-10 Energy and exergy efficiencies with varying temperature for (a) point specific low velocity, (b) specific effective velocity, (c) effective velocity and (d) average low velocity

assumptions that (a) V_2 is constant, or (b) V_2 / V_1 is maintained constant. The first law analysis does not predict changes to the system efficiency when this crucial operating condition is altered. In comparison, despite the assumption of V_2, the second law predicts an increased efficiency with higher values of V_1. The linear trend displayed by V_2 has a higher variability, suggesting that this method of estimating V_2 increases reliability with

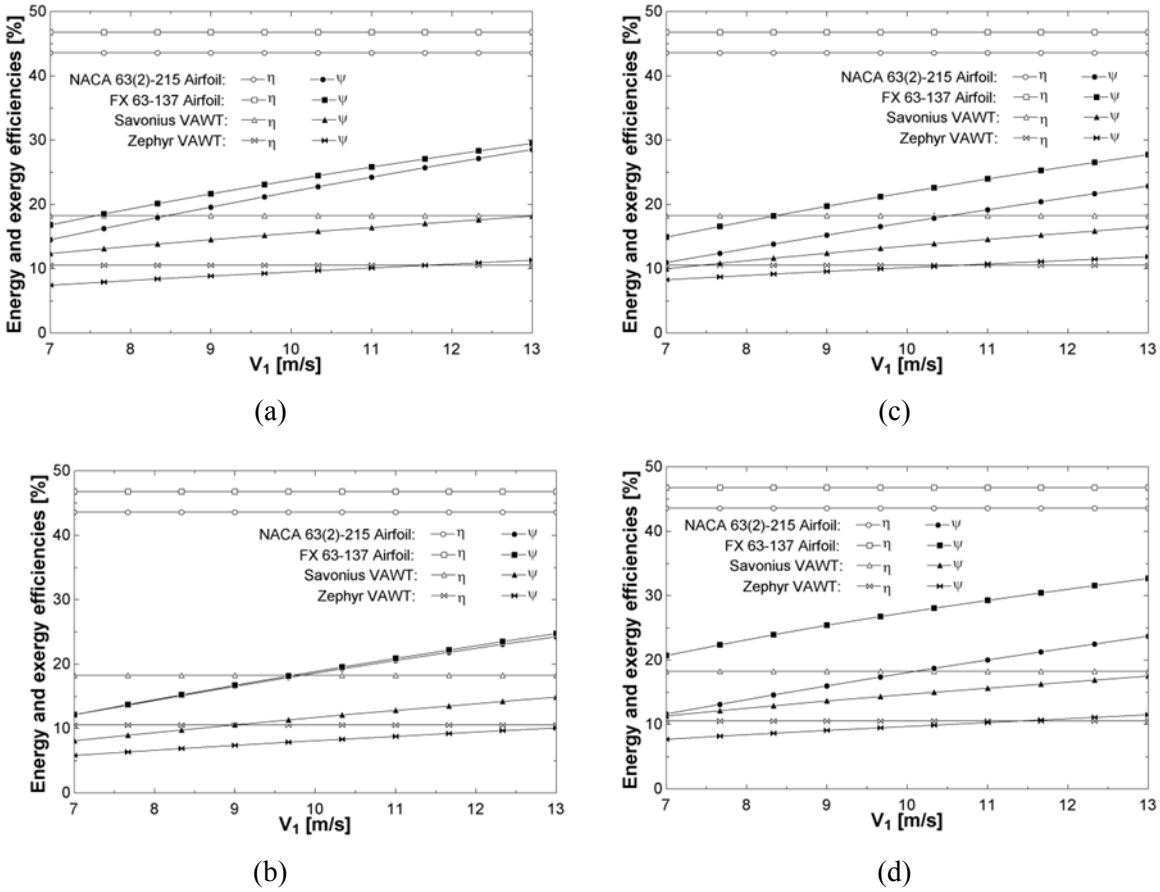

Figure 5-11 Energy and exergy efficiencies with varying V_1, constant V_2 for (a) point specific low velocity, (b) specific effective velocity, (c) effective velocity and (d) average low velocity

the assumption of V_1 / V_2 = C. More importantly, the second law efficiency reveals variability in the efficiency of each system for different wind conditions. This is valuable information when designing a turbine for a wide variety of wind conditions, or selecting a turbine for a specific site with one of the many different possible operating requirements.

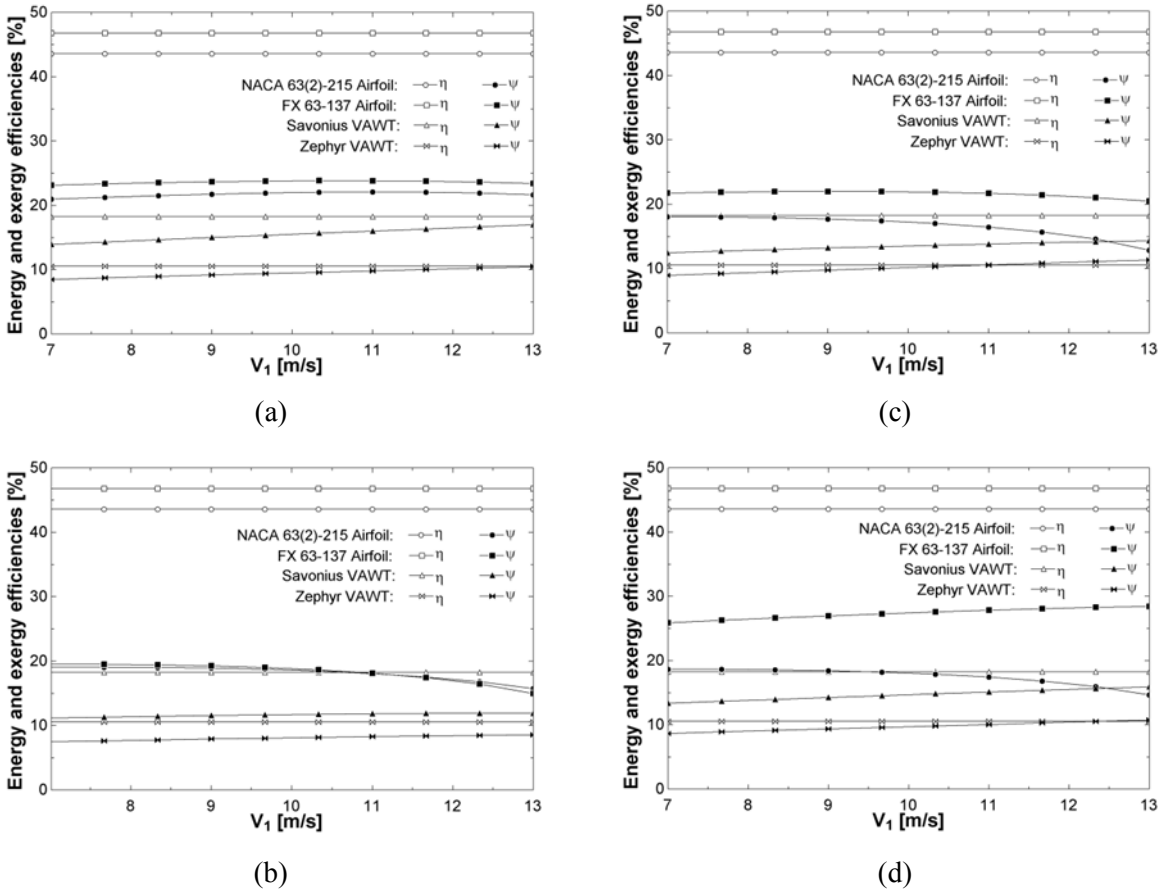

Figure 5-12 Energy and exergy efficiencies with varying V_1, constant V_1/V_2 for (a) point specific low velocity, (b) specific effective velocity, (c) effective velocity and (d) average low velocity

Sahin et al. [40] proposed that the shaft work is used to estimate the kinetic component of flow exergy. The same value is used to represent the work output, thereby assuming that the turbine is 100% energy efficient. This section identifies two alternative methods, using one of the proposed methods for obtaining V_2 to represent the change in kinetic energy. This includes the effects of ΔKE on (a) its inclusion in $\dot{E}x_{\text{flow}}$ as $\dot{E}x_{\text{KE}}$, and (b) assuming $\Delta KE = W_{\text{out}}$. To differentiate, the second law efficiencies in (a) are denoted as ψ_2. Figure 5.8a illustrates the variations in the incoming velocity, where η_{KE} and ψ_{KE} represent the first and second law efficiencies, with $\Delta KE = W_{\text{out}}$. A high level of variability is expected with the method of estimating V_2, thereby providing significant

information about the effects of the method. Furthermore, these plots present the point specific change in kinetic energy, as stated by the first law. Figures 5.8c and 5.8d present the methods of predicted flow exergy with a varying inlet velocity. A comparison with Figs. 5.11a and 5.12a predicts a 50 - 53% difference in the first and second law efficiencies for the airfoil systems, and 44 - 55% for the VAWTs, at reference conditions.

Figure 5.8e illustrates the results of a second law analysis of the Benz limit. The theoretical maximum energy efficiency is obtained with the Benz limit. With the first law, the Benz limit is a constant value, independent of operating conditions. However, combining the Benz limit theory with a second law analysis provides a theoretical maximum efficiency that includes the effect of irreversibilities, resulting in a dependence on design and operating conditions. Defining it here as $0.59\cdot(\dot{W}_{\text{out}}) \,/\, \dot{E}x_{\text{flow}}$, the second law Benz limit with both methods of obtaining $\dot{E}x_{\text{flow}}$ (i.e., ψ_B, and $\psi_{2,B}$) is presented. Significant variability between the VAWTs and the airfoils is predicted by ψ_B from 29% to 59%, while the range of $\psi_{2,B}$ is only 28% to 32%. As illustrated in Fig. 5.8f, Eqs, (3.7) and (3.9) are used to compare the maximum energy efficiency with the corresponding exergy efficiency. The value of C_a is varied from 0.15 to 0.5; Eq. (3.7) estimates the value of V_2 and Eq. (3.9) predicts the energy efficiency. Table 5.4 summarizes the first and second law efficiencies, predicted for the reference operating conditions.

Table 5-4 Predicted energy and exergy efficiencies

	η [%]	ψ [%]	ψ_2 [%]	ψ_B [%]	$\psi_{2,B}$ [%]	η_{KE} [%]	ψ_{KE} [%]	$\psi_{KE,2}$ [%]
NACA 63(2)-215 airfoil	44	21	22	29	30	39	19	20
FX 63-137 airfoil	47	23	22	30	28	59	29	27
Savonius VAWT	18	17	10	55	32	94	87	51
Zephyr VAWT	11	10	6	59	32	93	93	59

(ii) Method 2: Specific effective velocity ($V_2 = V_{2,\text{eff}} \times A_{\text{eff}} / A$)

This method suggests a high level of accuracy with the second law, as it attempts to specify the acting flow stream on the turbine. This method can provide a high level of comparability between different turbine designs and configurations. However, the precision of analysis could be problematic with this method, as it requires a level of intuition from the analyst. Figures 5.9b - 5.13b present the results of varying reference conditions and operating conditions for Method 2. A noticeable reduction in variability is experienced between the airfoils from Method 2. Also, the exergetic variability between the airfoils and VAWTs is reduced. Difficulties in defining the effective area for an airfoil could be a contributing factor.

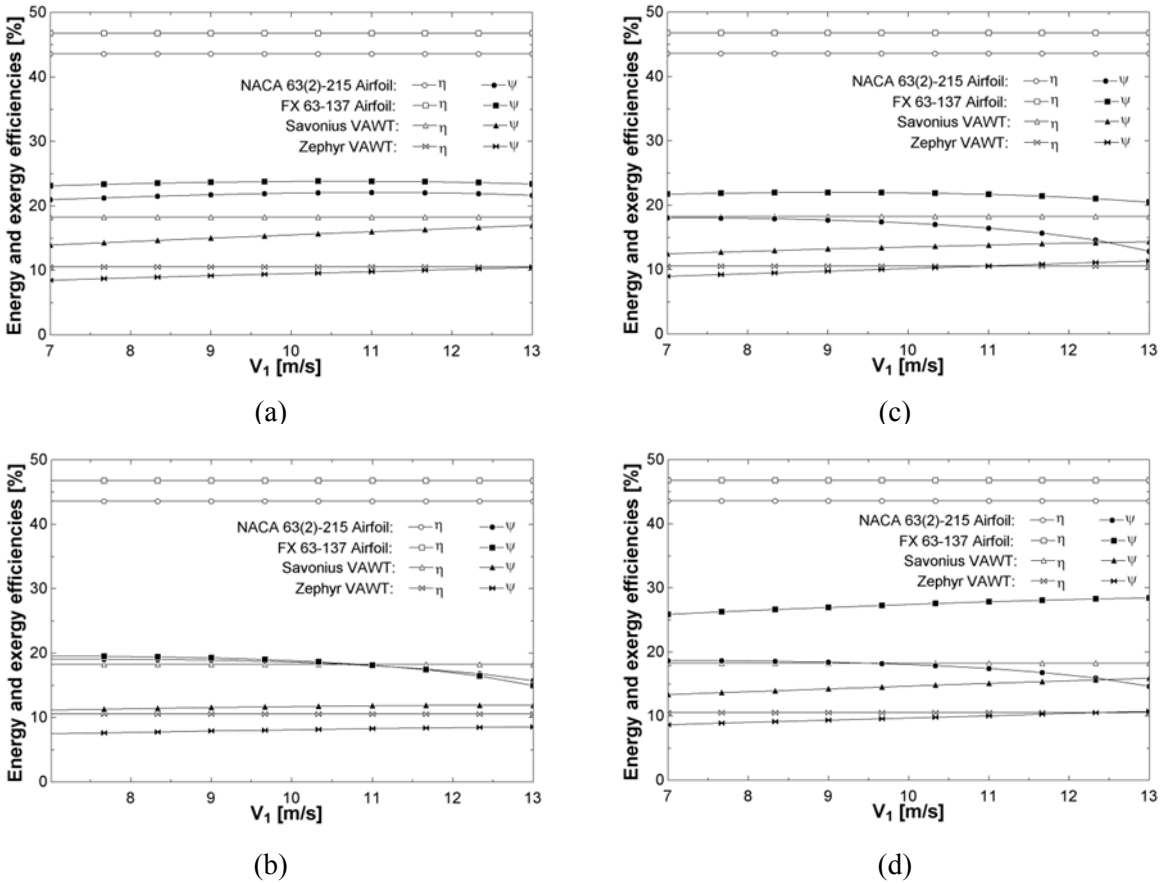

Figure 5-13 Specific exergy destruction with varying V_1, constant V_2/V_1 for (a) point specific low velocity, (b) specific effective velocity, (c) effective velocity and (d) average low velocity

The effective area is assumed as the high speed flow stream directed above the airfoil, with the total area taken to be the chord length. This method does not fully represent the differences in geometry between the airfoils, as the effects of tail curvature are not fully represented. Defining the effective area for the VAWT is comparatively straightforward. A low velocity flow stream is evident in the locations where a significant kinetic force is applied. An effective area is assumed as the cross-sectional area of this flow stream, with a total area assumed to be the turbine diameter. A notable result from Method 2 is illustrated in Fig. 5.12b, where the airfoil second law efficiencies exhibit a non-linear reduction in efficiency, falling rapidly after the reference wind velocity of 10 m/s. The VAWT second law efficiencies display a slight linear increase. The high values of V_2 suggested from Method 2 produce the lowest values of ψ throughout the study.

(iii) Method 3: Average velocity of useful area ($V_2 = V_{2,useful,\ ave}$)

Method 3 predicts the largest range in V_2, with 9.5 m/s for the NACA 63(2) - 215 airfoil, compared to 3.1 m/s for the Zephyr VAWT. A high dependence on the streamline configuration of the turbine is obtained by this method. A high level of precision is attainable, compared with Method 2, since the value is independent of size for the effective area. The analysis of Method 2 reveals an output for ψ that is evenly distributed at the reference conditions and throughout most of the varying operating conditions. Similar to Method 2, the relatively high values of V_2 for the airfoil translate into low second law efficiencies. However, the VAWTs are less affected. From Fig. 5.12c, the profile of an airfoil can significantly affect the second law efficiency. The basic profile of the NACA 63(2) - 215 exhibits only a slight reduction in second law efficiency, compared to the FX 63 - 137. A decreasing trend, which increases its rate of reduction

throughout the plot, is predicted for the more complex FX 63 - 137. At the upper boundary of V_1, the second law efficiency of the FX 63 - 137 airfoil falls below the value for the Savonius VAWT.

(iv) Method 4: Average of the low velocity stream

This method suggests a relatively even distribution of V_2 amongst the various systems. This translates into evenly distributed second law efficiencies, at the given reference operating conditions illustrated in Figs. 5.9d - 5.13d. Similar to the other methods, little effect is exhibited when altering the reference pressure. This method suggests a high variability between the airfoil second law efficiencies. Similar to Method 3, the second law efficiency for the NACA 63(2) - 215 airfoil deteriorates rapidly throughout the range of V_1, dropping below the Savonius second law efficiency within the operating velocity. The declining NACA 63(2) - 215 airfoil second law efficiency suggests that this method can give insight into the interdependence of the geometric profile, operating conditions, and turbine performance. Figure 5.13 compares the various methods of estimating V_2 in terms of ex_{dest}, assuming V_2 / V_1 is maintained constant. Many of the previous results can be understood through the exergy destruction. The first method predicts similar exergy destruction for the airfoils and VAWTs, respectively. It appears that this method does not fully represent the differences in flow irreversibilities between all systems. Better results would likely occur from Methods 3 and 4, whereby a greater range of variability is predicted between the various systems.

These case studies have compared the first and second law efficiencies of four wind energy systems. Difficulties exhibited with applying the exergetic analysis have been identified and preliminary solutions were obtained. The method of estimating V_2 has

been identified as a key component for implementing the second law in regular wind power analysis, optimization and design. The second law provides a valuable design tool that can help improve the efficiency and economic cost of wind power. Improvements to system output, development and installation can contribute to wind power systems alleviating the substantial demand from traditional non-renewable energy sources.

To ensure that wind energy capacity is fully utilized, the turbine design must be optimized to operate in various wind conditions. A second law analysis can contribute to improving the wind turbine design, system efficiency and power output. Significant reductions in the environmental impact of energy generation methods can be achieved through efficiency improvements via the second law. Wind power can provide a sustainable contribution to society's energy needs. The minimal impact caused by wind turbine manufacturing, installation, maintenance, and operation can be further reduced through efficiency improvements and enhanced design methodologies that use the second law of thermodynamics.

5.4 Rotor dynamics of a small horizontal axis wind turbine

In this section, the wind kinetic energy is used to estimate the turbine kinetic energy and shaft rotation of a HAWT. This approach offers the potential for higher accuracy when predicting fatigue stresses, transient operating conditions, and rotor control when converting mechanical to electrical energy. The new model will be applied to a standard HAWT.

Table 5.5 presents the operating parameters that are selected to represent typical turbine operating conditions. A three-blade turbine will be examined. The polar moment of inertia (J) for the systems is

$$J = \frac{1}{12}\, cbR(c^2 + R^2) \tag{5.4}$$

This assumes a rectangular blade profile. A constant chord length, angle of relative wind and wind speed are assumed throughout the length of each blade. The angle of relative wind is initially 8 degrees and then varied from 3 to 12 degrees in the parametric analysis. A range of drag coefficients is obtained for each parametric study. The values of C_D are taken to be 0, 0.01, 0.02, and 0.04, while the lift coefficient is maintained constant. This covers a range of C_L / C_D ratios, including 100, 50 and 25. The problem assumptions and range of parameters are presented in Table 5.5.

Table 5-5 Problem parameters

	Units	Value	Parametric Range
Number of blades	-	3	-
Air density	kg/m^3	1.225	-
Chord length	m	0.5	-
Blade length	m	10	-
Approach angle	°	8	3 to 12
Lift coefficient	-	1	-
Drag coefficient	-	-	0 to 0.04
Wind velocity	m/s	10	4 to 13

Figure 5.14 presents a comparison of the conventional wind kinetic energy availability (i.e. Eq. (3.18)) and the new rotor dynamic model that uses angular shaft acceleration to predict the maximum available energy. This figure provides useful validation of the new formulation, since it predicts the same power output throughout the entire range of simulated wind velocities. Also, this close agreement is independent of the C_L / C_D ratio, thereby indicating the model robustness. This curve exhibits the expected trend of a cubic increase of power output, as a function of wind velocity, for all three

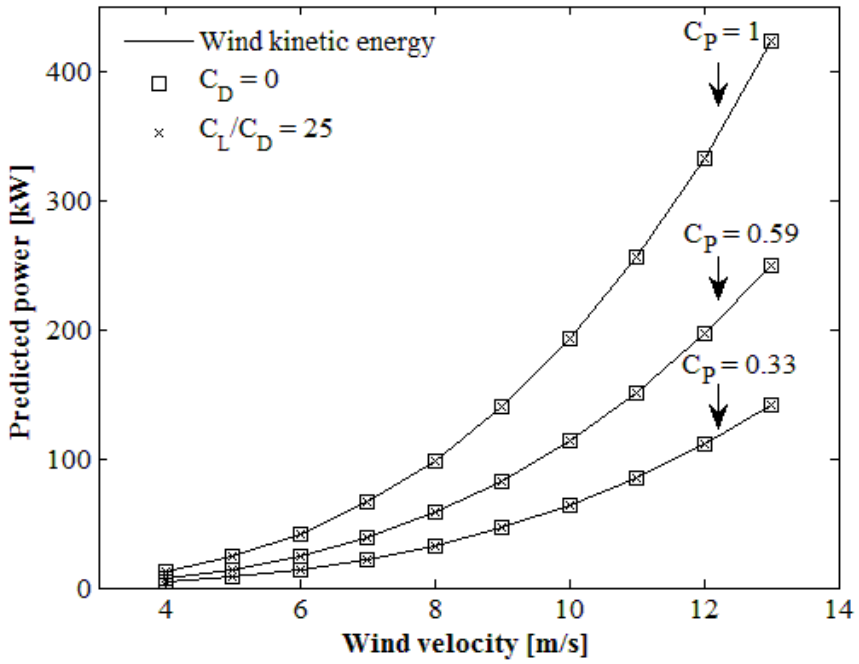

Figure 5-14 Comparison of predicted power output with maximum wind kinetic energy

cases. A range of 4 m/s to 13 m/s is covered by the results, which includes the majority of operating conditions commonly encountered by wind turbines. For the remaining results, the power coefficient in Eq. (3.18) is taken as 0.59, as defined by the theoretical maximum Benz limit.

Operating speeds are typically based on the maximum power output with the variable λ. As an individual turbine's capacity increases, the role of fatigue and mechanical stresses will also increase. The newly developed model can supply information about the acceleration and forces applied on the rotor. By including the rotational velocity and rotor acceleration, the controller can adjust operating components to extract higher energy from the air stream. As the C_L / C_D ratio is reduced, the predicted angular acceleration and rotor velocity are shifted left along the curve in Fig. 5.15. This illustrates a potential advantage compared to the conventional wind kinetic energy limit; predicted by Eq. (3.18). A higher angular acceleration component that coincides with a

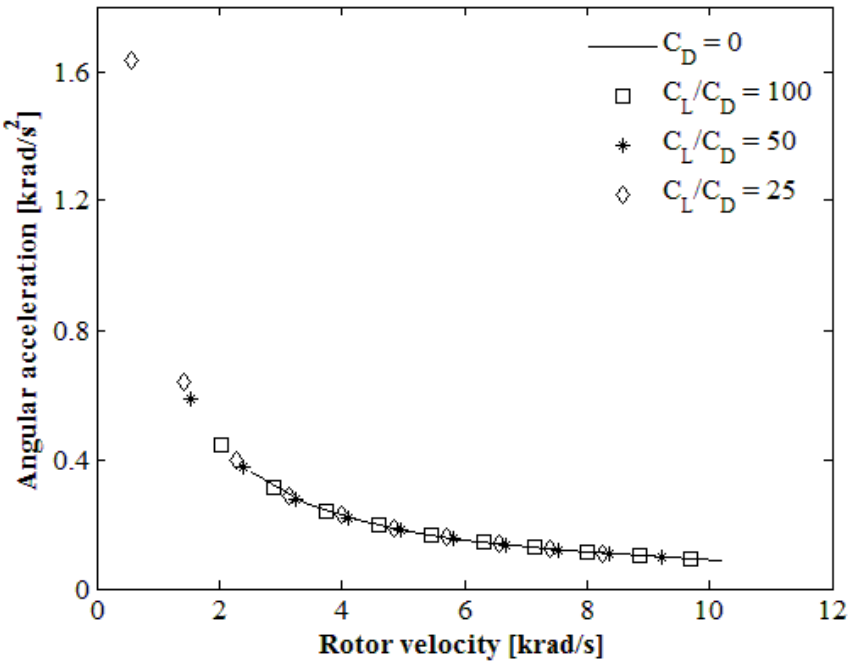

Figure 5-15 Shaft angular acceleration at varying rotor velocities and force coefficient ratios

lowered rotor velocity is adjusted so that the predicted power is constant (see Fig. 5.14). This can supplement existing techniques to control operating parameters and reduce fatigue stresses. Additional knowledge about the angular acceleration component can provide more precise cut-off limits, reduced maintenance costs, and increase turbine availability. Controlling a turbine at high wind speeds is generally accomplished by maintaining a constant speed, beyond a predetermined set-point. These limits can be improved with the newly developed model, by reducing the operating tolerances.

As presented in Fig. 5.16, the angular acceleration is examined with a variable angle of relative wind (φ). In contrast to Figs. 5.14 and 5.15, a change of C_L / C_D has a significant effect on the resulting angular acceleration. Reducing the value of C_D (i.e. increasing C_L / C_D) leads to an appreciable reduction in each curve that represents the rotor angular acceleration. A change that is proportional to the reduction in C_D is exhibited throughout the range of φ. Such variations are not represented by current

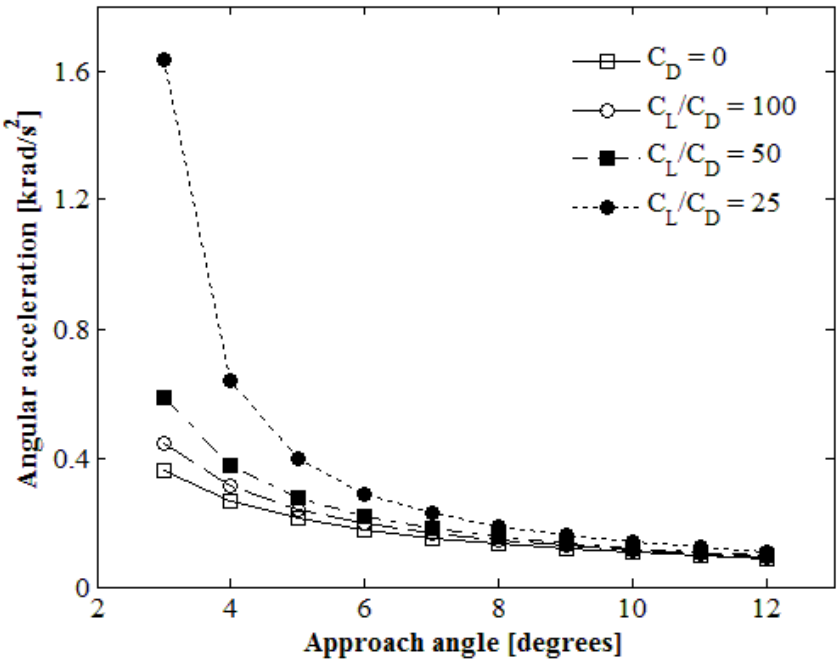

Figure 5-16 Shaft angular acceleration at varying approach angles and force coefficient ratios

models of maximum wind energy. By relating this wind energy to the rotor dynamics, electrical systems can have a more useful upper bound for the rotor control strategy, thereby extracting a higher amount of power from the incoming air stream.

Full transient aspects of the model have the biggest opportunity to improve performance, incorporated into more complicated control systems. An example transient application of the model is presented in Figs. 5.17 and 5.18. For this simplified example, the transient wind speed is represented by a positive sinusoidal curve. In the 100 modelled timesteps there are four wind velocity peaks, with a minimum velocity of 1m/s and a maximum velocity reaching 21 m/s. Predicting the rotor's acceleration allows controllers the opportunity to impose limits on the acceleration. Generally, controllers only limit the maximum speed of the rotor, but reducing the large acceleration forces can increase the longevity of the turbine and reduce maintenance costs.

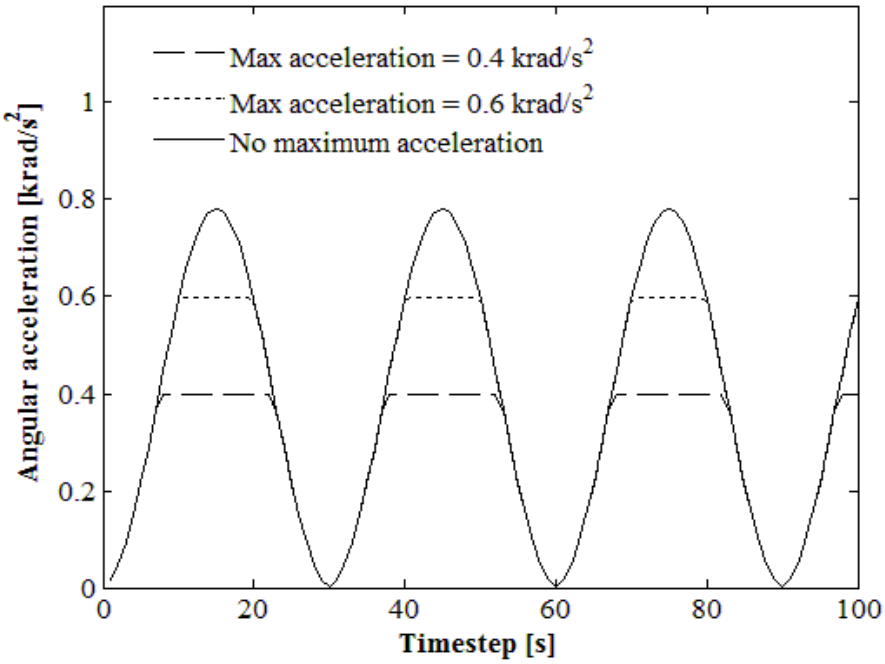

Figure 5-17 Predicted transient angular acceleration with varying limits of maximum rotor acceleration

Figure 5.17 illustrates the predicted angular acceleration imposed on the rotor from the transient wind conditions. Also, the figure shows two imposed limits on the maximum angular acceleration, specifically 0.4 krad/s^2 and 0.6 krad/s^2. Variable pitch blades and a variety of electrical control techniques can be used to impose the acceleration limits. However, a combination of mechanical control (variable pitch blades) and electrical control (adaptive feedback linearization, inverter firing angle control, etc.) can achieve superior performance. Relying solely on variable pitch blades to limit the rotor acceleration can reduce the power output during periods of high wind speeds. Figure 5.18 illustrates the predicted transient power coefficient with varied rotor acceleration limits. When the limit is maintained at 0.6 krad/s^2, the power coefficient drops during periods of high wind speed, thereby reducing the overall power output. This effect is dramatically expressed by the 0.4 krad/s^2 limit. An electrical control technique, whereby the power generation increases as the rotor acceleration is reduced, would be a beneficial

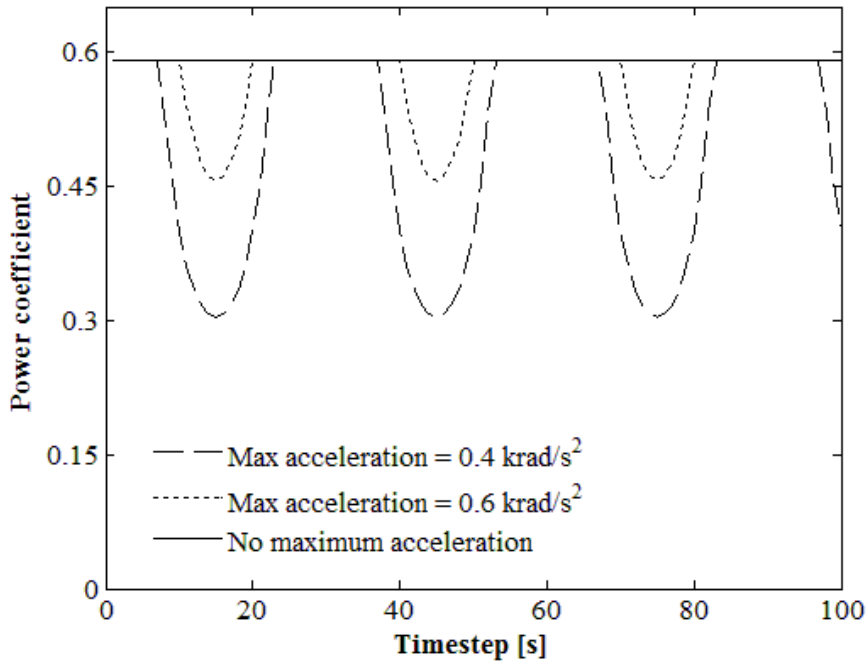

Figure 5-18 Predicted transient power coefficient with varying limits of maximum rotor acceleration

match for this model. This has the potential to increase maximum rotor velocity limits as the coinciding acceleration forces can be monitored and controlled.

5.5 Power correlation for Zephyr vertical axis wind turbine with varying geometry

In this section, the dimensional analysis in Section 3.3 will be applied to a Zephyr VAWT design. Numerical predictions are conducted to obtain a turbine-specific correlation for the ZVWT. The correlation will predict the turbine's C_p after changes to critical features of the VAWT, i.e., Fig. 3.2b, and operating conditions such as the rotor velocity and wind speed. A power coefficient correlation for a novel VAWT is developed, particularly a Zephyr Vertical axis Wind Turbine (ZVWT). The turbine is an adaptation of the Savonius design. The new correlation can predict the turbine's performance for altered stator geometry and variable operating conditions. Numerical

simulations with a rotating reference frame are used to predict the operating performance for various turbine geometries. The case study includes 16 different geometries for three different wind directions. The resulting 48 data points provide detailed insight into the turbine performance to develop a general correlation. The model is able to predict the power coefficient with changes in λ, rotor length, stator spacing and stator angle, to within 4.4% of the numerical predictions. Furthermore, the power coefficient is predicted with changes in rotor length, stator spacing and stator angle, to within 3% of the numerical simulations. As a result, the correlation provides a useful new design tool for improving the ZVWT for the conditions and operating requirements specific to this type of wind turbine. Also, the new model can be extended to other conditions that include different VAWT designs.

Figure 5.19 illustrates the predicted ZVWT performance curves. In order to develop the power correlation, 16 geometrical configurations were generated. Each of the

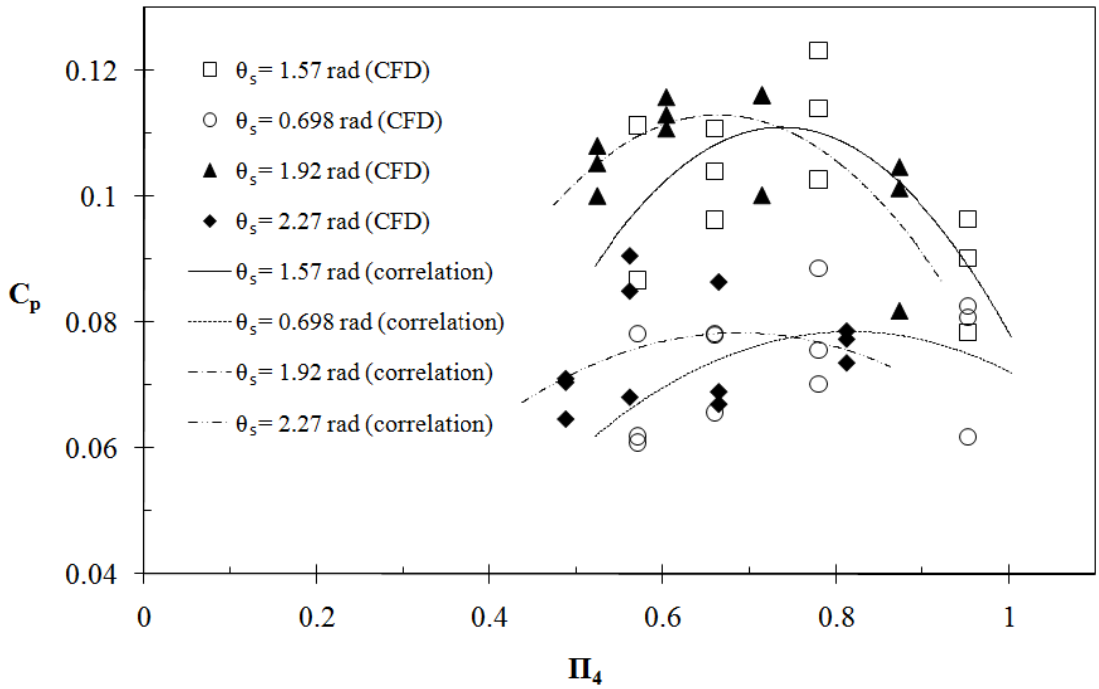

Figure 5-19 Results of C_p for different values of Π_4 (λ = 0.34 rad/s)

turbine geometries is represented at three different orientations relative to the wind direction. The orientations are made such that the stator is rotated by π / 3 radians. A detailed list of geometrical variables is presented in Table 5.6. The average C_p values at varying magnitudes of Π_4 are used for the dimensional analysis. A plot of the different geometrical configurations is illustrated in Fig. 5.19. The average C_p values are then used to generate four distinct power curves. These power curves represent discrete values of θ_s, specifically 0.698, 1.57, 1.92 and 2.27 radians. Each of these curves will be discussed in the four cases below.

Case 1: θ_s = 1.57 radians

This power curve represents the most recent ZVWT design. This design has been adapted for improved performance via both numerical and experimental studies [68, 72]. The value of θ represents a design where the stator makes a π / 4 planar angle with the

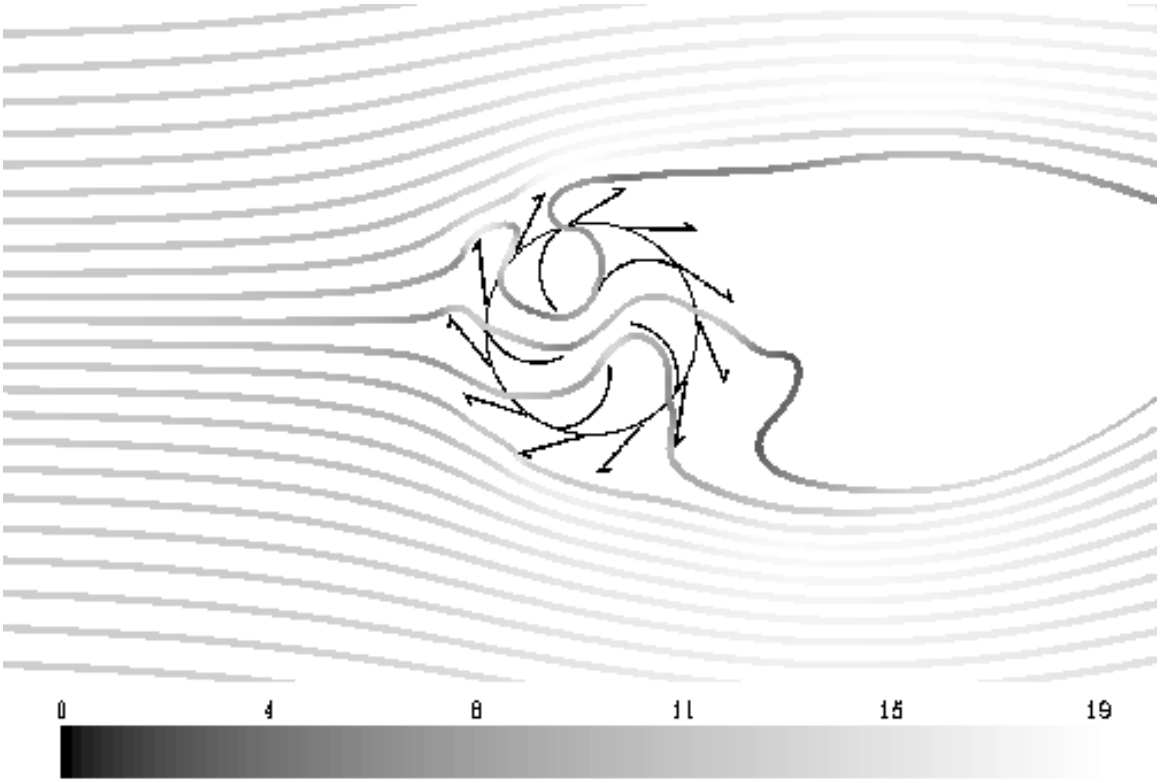

Figure 5-20 Pathlines shaded by the velocity magnitude (m/s)

turbine's centerline. This angle appears to provide a good balance between flow stream diversions, while maintaining a low degree of back pressure in front of the turbine. The flow pathlines in Fig. 5.20 represent the case 1 geometry, and they are useful for visualizing the air flow. This case will represent the base curve for the subsequent analysis. Geometries in this case have a rotor radius (R) of 0.28 m, as per the current Zephyr design. The analysis presented in Fig. 3.1 is used to identify a suitable rotor velocity for maximizing the turbine performance. This imposes a constraint of Ω = 15 rad/s for the rotational velocity of the rotor subdomain. The turbine width (W) is maintained at 0.762 m and the freestream velocity at 12.5 m/s, throughout the analysis. The power coefficient is determined from the product of the angular speed and the predicted torque applied on the rotor blades from the passing wind.

Previous experiments have investigated the performance of a ZVWT with 9 stator blades [72]. However, current numerical predictions have indicated that increasing the number of stator blades will improve turbine performance. Therefore, in all four cases, 9, 11, 13, and 15 stator blades will be represented. The result is four finite values of σ, specifically 0.27 m, 0.22 m, 0.18 m and 0.16 m, respectively. The power curve for this case was obtained by curve fitting of CFD data, leading to the following result:

$$C_P = -0.4744 \cdot \Pi_4^{\,2} + 0.6992 \cdot \Pi_4 - 0.1466 \tag{5.5}$$

This applies to geometries whereby the dimensionless variable Π_4 lies between 0.57 and 0.95. The variability in the data set is calculated by the coefficient of determination (R^2), determined from the square of the Pearson correlation coefficient [73]. The R^2 for the curve is 0.89, which indicates low variability.

Case 2: θ_s = 0.698 radians

This power curve represents the lowest value of θ in the study. The low stator angle in this configuration does not effectively divert the flow stream and it produces a relatively low power curve. This is illustrated in Fig. 5.21, which presents the contours of static pressure. The geometries in this case are maintained at an identical rotor radius, as with case 1. This maintained an equivalent Π_4 and Ω values between the two cases. The power curve for this case is represented by

$$C_p = -0.1901 \cdot \Pi_4^{\,2} + 0.3105 \cdot \Pi_4 - 0.0483 \tag{5.6}$$

for geometries where the dimensionless variable Π_4 lies between 0.57 and 0.95. The resultant R^2 value for this curve is 0.99, which demonstrates extremely low variability. At this low value of θ_s, the solution decreases in accuracy at lower values of Π_4. This is

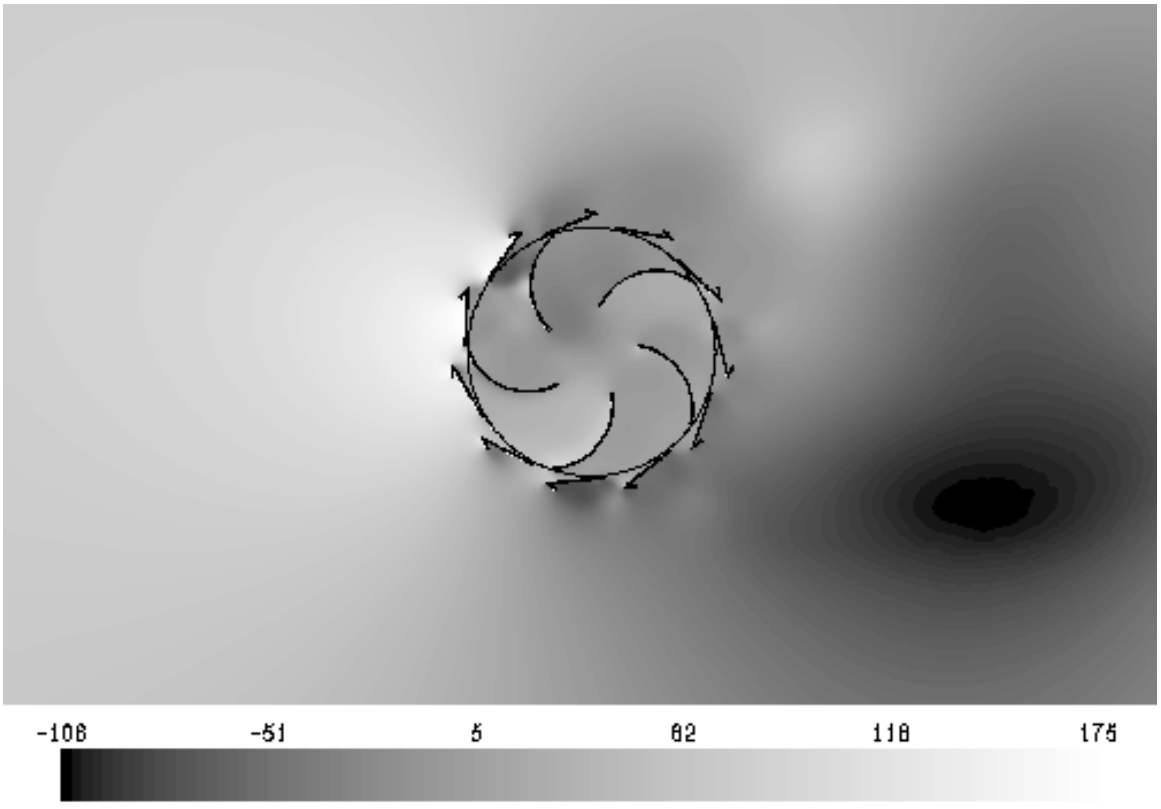

Figure 5-21 Contour plots of static pressure (Pa)

likely caused by the combination of low stator angle and large spacing, which significantly diminishes the stator cage effects. This configuration would not substantially reduce the turbulence effects on the rotor blades. The correlation's accuracy diminishes for this combination of very low θ_s and high Π_4.

Case 3: θ_s = 1.92 radians

To maintain a constant turbine radius, the increased stator angle associated with this case requires a geometrical constraint on the minimum length of R. The radius length is set to 0.3028 m. This change from case 1 shifts the power curve to the left. To maintain a constant λ between different cases, Ω for the simulations in this curve is set to 13.75 rad/s. Based on CFD data, the power curve for this case is correlated by

$$C_p = -0.3949 \cdot \Pi_4^{\,2} + 0.5242 \cdot \Pi_4 - 0.061 \tag{5.7}$$

for geometries where the dimensionless variable Π_4 lies between 0.52 and 0.87. The resultant R^2 value for this curve is 0.97, which indicates very low variability.

Case 4: θ_s = 2.27 radians

This power curve represents the highest value of θ in the study. The high stator angle in this configuration produces a large amount of back pressure and it captures relatively little flow through the turbine. These factors explain the low power curve associated with this case. The high back pressure can be visualized in Fig. 5.21, which depicts the pressure contours of the turbine flow field. The radius length is set to 0.3277m. This further shifts the power curve to the left. For this curve, Ω is maintained at a constant 12.79 rad/s. From curve fitting of CFD data, the power curve can be represented by

$$C_p = -0.1762 \cdot \Pi_4{}^2 + 0.2424 \cdot \Pi_4 - 0.005 \tag{5.8}$$

for geometries where the dimensionless variable Π_4 lies between 0.49 and 0.81. The resultant R^2 value for this curve is 0.31, which indicates a relatively high degree of variability. It is evident that the correlation has less accuracy as the value of θ_s approaches 2.27 radians, due to the high back pressure introduced by this turbine configuration.

In efforts to collapse all of the previous results into a single correlation, the curves associated with each of the four cases are normalized in the dimensionless plane according to the following function,

$$\tilde{C}_P(f) = -0.4744 \cdot \tilde{\Pi}_4(g)^2 + 0.6992 \cdot \tilde{\Pi}_4(g) - 0.1466 \tag{5.9}$$

where $\tilde{C}_p(f) = C_p + f(\theta_s)$ and $\tilde{\Pi}_4(g) = \Pi_4 + g(\theta_s)$. The four curves collapse onto a single curve, as shown in Fig. 5.22. As previously discussed, the curve representing θ_s =

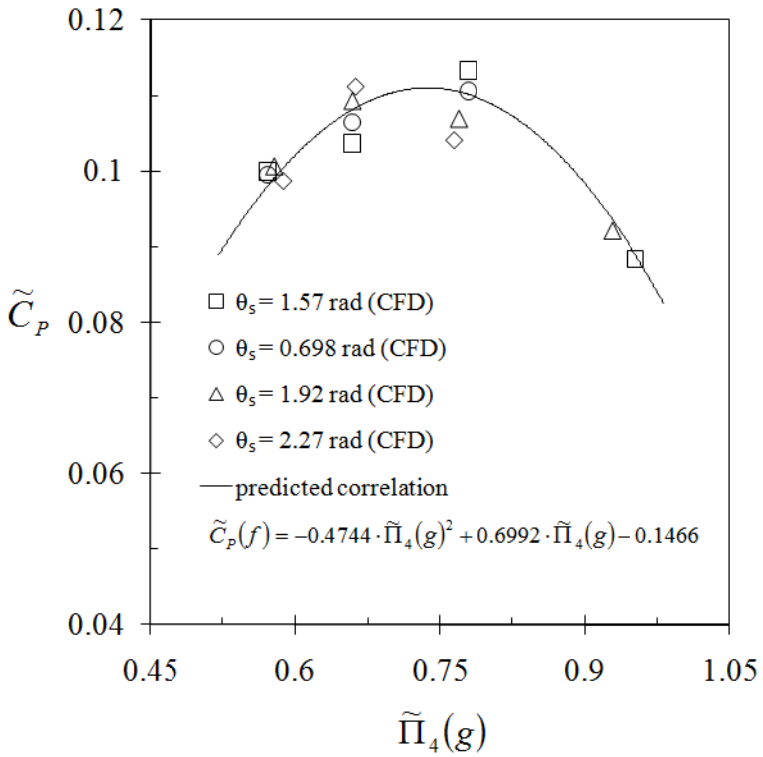

Figure 5-22 Comparison of numerical and predicted values, normalized to the plane $\left|\tilde{C}_p, \tilde{\Pi}_4\right|$

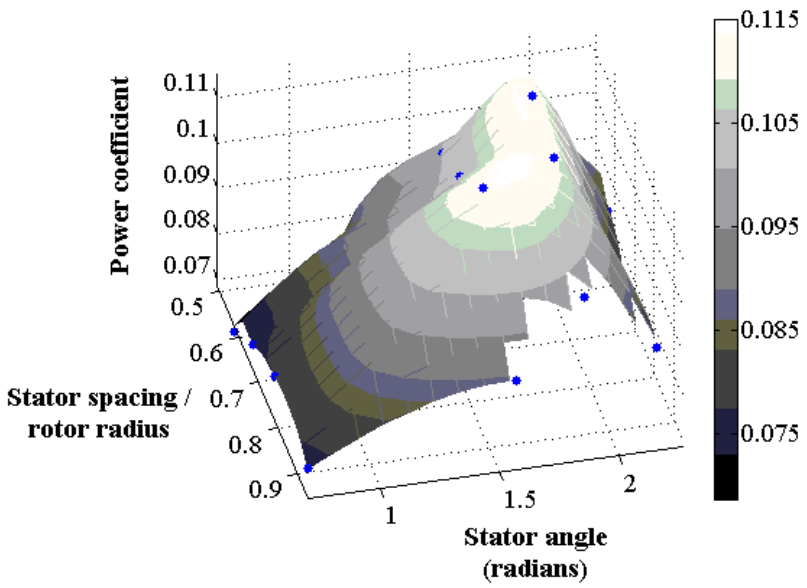

Figure 5-23 Surface contours relating the changes of C_p, Π_4, and θ_s

2.27 radians provides a moderate degree of accuracy, and less accuracy with a high Π_4 value (Π_4 = 0.81). Also, in the solution domain where a combination of low angle (θ_s = 0.698) and high Π_4 (Π_4 = 0.95) is used, the accuracy of the correlation also decreases (see Fig. 5.23). The curve fitted functions for f and g are presented in Fig. 5.24. The normalization coefficient $f(\theta_s)$ can be represented as follows,

$$f(\theta_s) = 0.0575\theta_s^{\,2} - 0.1746\theta_s + 0.127 \tag{5.10}$$

where minimal variability is exhibited compared with the numerical prediction (R^2 = 0.91). The normalization coefficient $g(\theta_s)$ can be represented by

$$g(\theta_s) = 0.0825\theta_s^{\,2} - 0.1782\theta_s + 0.0833 \tag{5.11}$$

which shows minimal variability with the numerical prediction (R^2 = 0.98). The overlapping data points at θ_s = 1.57 radians coincide with the base case configuration (case 1). All power curves are collapsed onto a single normalized power curve, resulting in a null value for $f(1.57)$ and $g(1.57)$. The general correlation becomes

$$C_P(\Pi_4,\theta_s) = -0.4744\cdot[\Pi_4 + g(\theta_s)]^2 + 0.6992\cdot[\Pi_4 + g(\theta_s)] - 0.1466 - f(\theta_s) \quad (5.12)$$

where $f(\theta_s)$ and $g(\theta_s)$ are described by equations (5.10) and (5.11), respectively.

Additional numerical predictions have been extensively compared with the correlation described by Eq. (5.12). Figure 5.25 illustrates the model's ability to predict results that lie outside of the CFD simulated conditions. For example, three additional ZVWT configurations are represented in Fig. 5.25. The first of these configurations provides a verification of the method's ability to provide accurate predictions for the turbine at θ_s = 2.09 radians. For this prediction, R = 0.32 m, σ = 0.20 m, and Ω = 13.2 rad/s, resulting in a Π_4 value of 0.63. The dimensionless predictions provide a useful comparison with the numerical predictions for this configuration, in Fig. 5.25. The error between the numerical prediction and the newly developed correlation is ±4.4%. The second point maintains θ_s = 2.09 radians, R = 0.32 m, and Ω = 13.2 rad/s, but σ is changed to 0.27 m. This selection

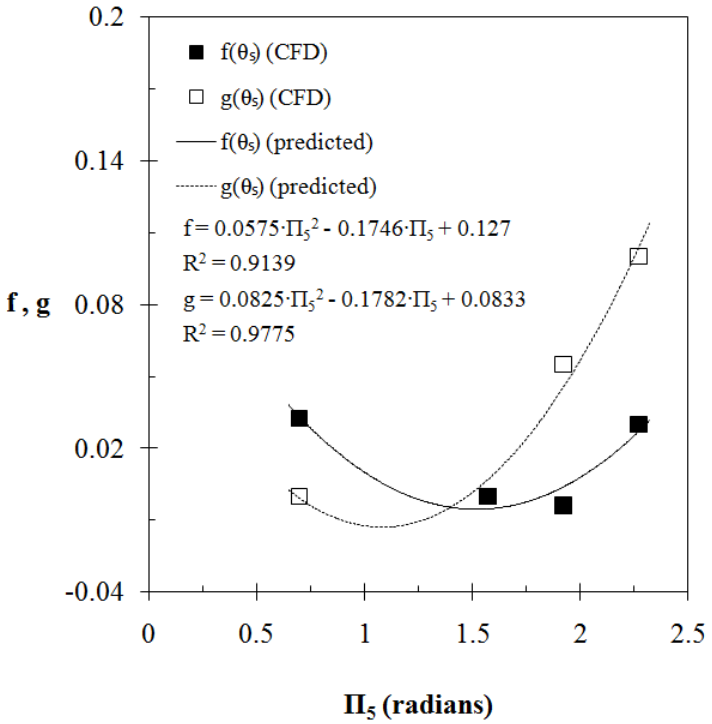

Figure 5-24 Dimensionless solution variables *f* and *g*

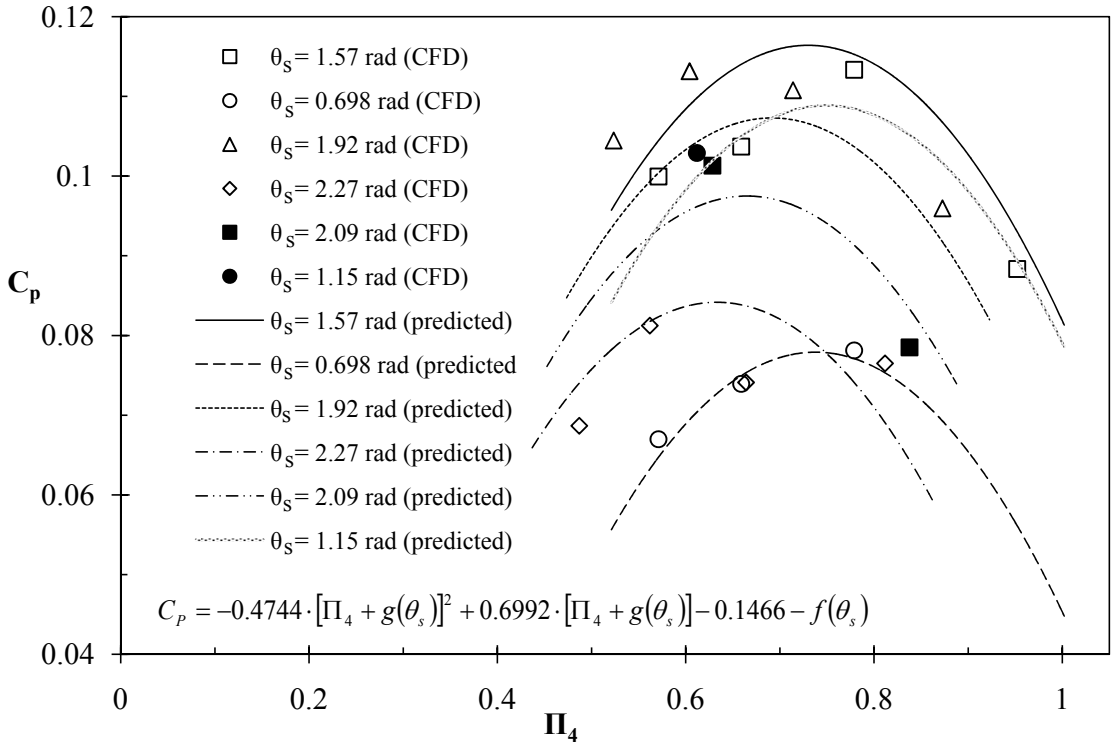

Figure 5-25 Validation plot of the dimensionless correlation

of variables represents a Π_4 term of 0.84, which is quite far from the previous Π_4 value of 0.63. The error is 5.8% when compared to the numerical predictions. Finally, the point at θ_s = 1.15 radians illustrates the model's ability to predict the performance for turbine configurations in the lower range of θ_s. For this prediction, R = 0.28 m, σ = 0.17 m, and Ω = 15 rad/s. Again the correlation described by Eq. (5.12) provides an excellent prediction of the turbine's performance in Fig. 5.25. The associated error is about 2.9%.

By developing a general correlation that predicts the ZVWT performance, further design improvements can be undertaken without the need for time-consuming CFD predictions for each case. The correlation provides a useful design tool for adapting the turbine conditions and operating requirements, specific to a drag type VAWT. It becomes easier to quickly predict how changes to the VAWT's essential design features will

impact its performance with a reasonable degree of accuracy. The correlation can also be useful for developing an optimum turbine design, while limiting the need for further CFD simulations and time intensive mesh generation for each different turbine configuration.

Table 5-6 Problem variables

Geometry	**Orientat-ion (°)**	**Rotor radius [R] (m)**	**Number of stators**	**Angle [θ_s] (deg)**	**Rotor velocity [Ω] (rad/s)**	**Moment (N-m)**
Case 1						
1		0.279	9	45	15	4.465
	13.3	0.279	9	45	15	4.178
	26.6	0.279	9	45	15	3.629
1 - average		**0.279**	**9**	**45**	**15**	**4.091**
2		0.279	11	45	15	5.281
	10.9	0.279	11	45	15	5.708
	21.8	0.279	11	45	15	4.756
2 - average		**0.279**	**11**	**45**	**15**	**5.248**
3		0.279	13	45	15	4.46
	9.23	0.279	13	45	15	4.818
	18.5	0.279	13	45	15	5.128
3 - average		**0.279**	**13**	**45**	**15**	**4.802**
4		0.279	15	45	15	5.154
	8	0.279	15	45	15	4.014
	16	0.279	15	45	15	4.717
4 - average		**0.279**	**15**	**45**	**15**	**4.628**
Case 2						
5		0.279	9	20	15	2.86
	13.3	0.279	9	20	15	3.743
	26.7	0.279	9	20	15	3.823
5 - average		**0.279**	**9**	**20**	**15**	**3.475**
6		0.279	11	20	15	3.499
	10.9	0.279	11	20	15	3.25
	21.8	0.279	11	20	15	4.105
6 - average		**0.279**	**11**	**20**	**15**	**3.618**
7		0.279	13	20	15	3.043
	9.23	0.279	13	20	15	3.609
	18.5	0.279	13	20	15	3.619
7 - average		**0.279**	**13**	**20**	**15**	**3.424**
8		0.279	15	20	15	2.821
	8	0.279	15	20	15	2.866

	16	0.279	15	20	15	3.619
8 - average		**0.279**	**15**	**20**	**15**	**3.102**
Case 3						
9		0.305	9	55	13.75	5.288
	13.3	0.305	9	55	13.75	5.118
	26.7	0.305	9	55	13.75	4.135
9 - average		**0.305**	**9**	**55**	**13.75**	**4.847**
10		0.305	11	55	13.75	5.062
	10.9	0.305	11	55	13.75	5.866
	21.8	0.305	11	55	13.75	5.860
10 - average		**0.305**	**11**	**55**	**13.75**	**5.596**
11		0.305	13	55	13.75	5.595
	9.23	0.305	13	55	13.75	5.706
	18.5	0.305	13	55	13.75	5.848
11 - average		**0.305**	**13**	**55**	**13.75**	**5.716**
12		0.305	15	55	13.75	5.458
	8	0.305	15	55	13.75	5.056
	16	0.305	15	55	13.75	5.318
12 - average		**0.305**	**15**	**55**	**13.75**	**5.277**
Case 4						
13		0.328	9	65	12.79	4.200
	13.3	0.328	9	65	12.79	3.994
	26.7	0.328	9	65	12.79	4.270
13 - average		**0.328**	**9**	**65**	**12.79**	**4.155**
14		0.328	11	65	12.79	3.636
	10.9	0.328	11	65	12.79	4.6961
	21.8	0.328	11	65	12.79	3.743
14 - average		**0.328**	**11**	**65**	**12.79**	**4.025**
15		0.328	13	65	12.79	3.696
	9.23	0.328	13	65	12.79	4.923
	18.5	0.328	13	65	12.79	4.6169
15 - average		**0.328**	**13**	**65**	**12.79**	**4.412**
16		0.328	15	65	12.79	3.506
	8	0.328	15	65	12.79	3.826
	16	0.328	15	65	12.79	3.857
16 - average		**0.328**	**15**	**65**	**12.79**	**3.730**

5.6 Analytical predictions of power coefficient for a Savonius vertical axis wind turbine

In this section, the results of the analytical model for predicting the performance of a Savonius turbine will be presented. The model is considered for a VAWT with one or two blades. As illustrated in Fig. 2.1, the simulated turbine has cylindrical rotor blades with a rotor radius, a, of 0.50 m and an overlap, β, of 0.10 m. A wind velocity of 10 m/s is used, with the turbine operating at a tip speed ratio, λ, of 0.5.

As the wind flows around the rotating rotor blades, a pressure differential is developed along the blade surface. The y-component of this force (perpendicular to the freestream), F_{yp}, represents the lift force on the turbine, predicted by Eq. (2.38). As illustrated in Fig. 5.26, a maximum positive value is exhibited as the rotor rotates around the wayward side of the turbine. This force acts perpendicular to the flow stream, contributing to turbine power throughout the entire rotor rotation. When the rotor rotates

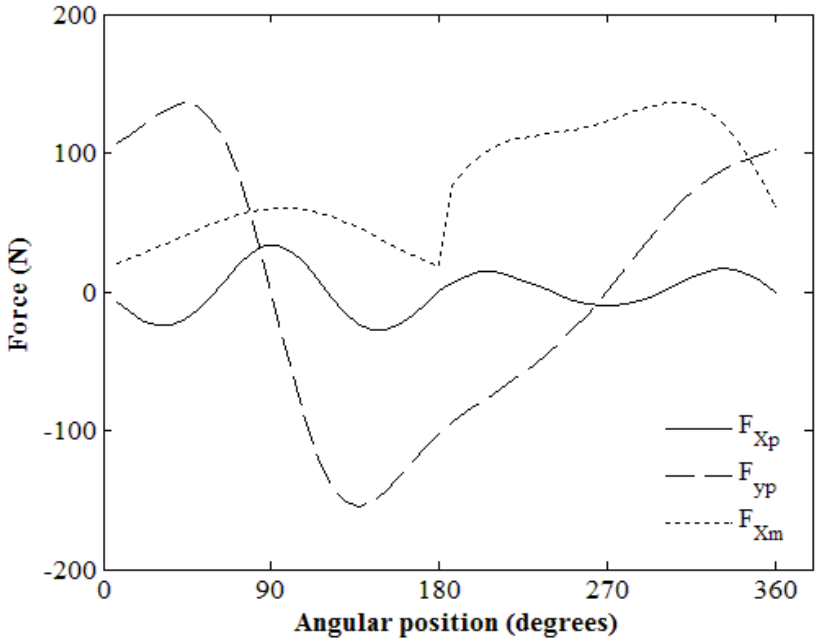

Figure 5-26 Analytical predictions of component forces on a cylindrical Savonius rotor blade

around the windward side of the turbine, the lift force has a similar magnitude to the wayward peaks, but an opposite sign (i.e. negative). In the Cartesian coordinate system, the rotor is rotating in the negative y-direction on the windward side. The lift is contributing to the rotor rotation though all θ angles. As predicted by Eq. (2.37), the pressure drag, F_{xp}, represents the induced force from the pressure differential on the convex surface of the rotor. With the exception of acting parallel to the freestream, this force is similar to the lift force. During the return stroke, the pressure drag reduces power and it should be limited. During the power stroke, this force can contribute to power production. As illustrated in Fig. 5.26, the pressure drag can cause a significant reduction in power as the rotor rotates through $\theta = 90°$, with smaller power contributions through $\theta = 200°$ and $\theta = 325°$. The momentum force, F_{Xm}, as predicted by Eq. (2.41), exhibits a discontinuity at the angles where the rotor changes streamtubes (i.e. $\theta = 0$ and $\theta = \pi$). In a field test, the effect of varying the rotor blade number would have a significant

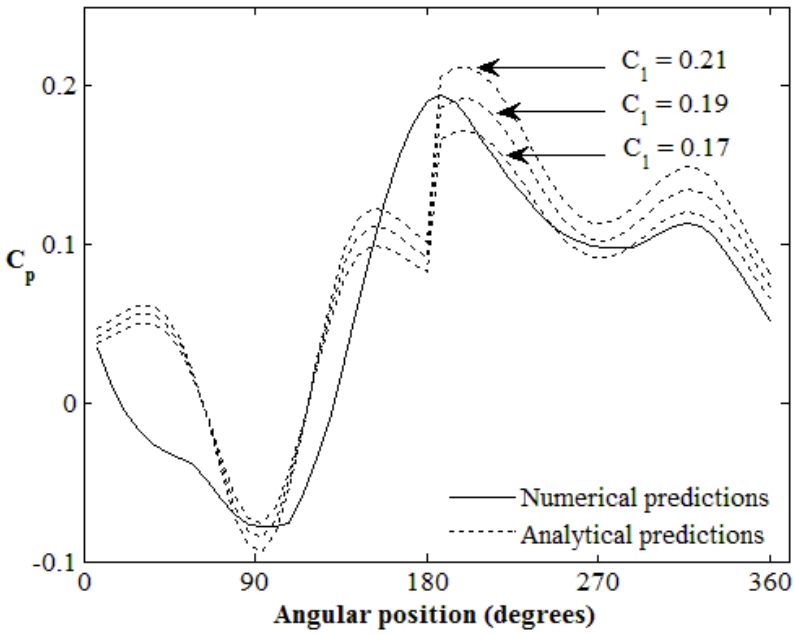

Figure 5-27 Predicted transient power coefficient for a single blade Savonius rotor blade

impact on this force, because of the blade interaction. A second rotor blade can alter the mass flowrate into the blades, as well as alter the wayward pressure, particularly, during the return stroke.

The analytical predictions are compared to numerically simulated power curves for both the single and double rotor designs. The numerical predictions are obtained from a rotating mesh simulation, as described in Chapter 2 and Section 5.2. A unique simulation is produced for each geometry (i.e. single or double blade). From the solid line in Figs. 5.27 and 5.31, an average power coefficient of 0.062 and 0.176 is numerically predicted for the single and double blade VAWT, respectively. As illustrated in Fig. 5.28, using the aerodynamic forces on the rotor blades with Eqs. (2.44) and (2.45), the model predicts a transient power coefficient that closely matches the normalized numerical predictions. The numerical predictions are normalized by dividing by the highest instantaneous C_p of 0.194. The analytical model does not fully represent the viscous,

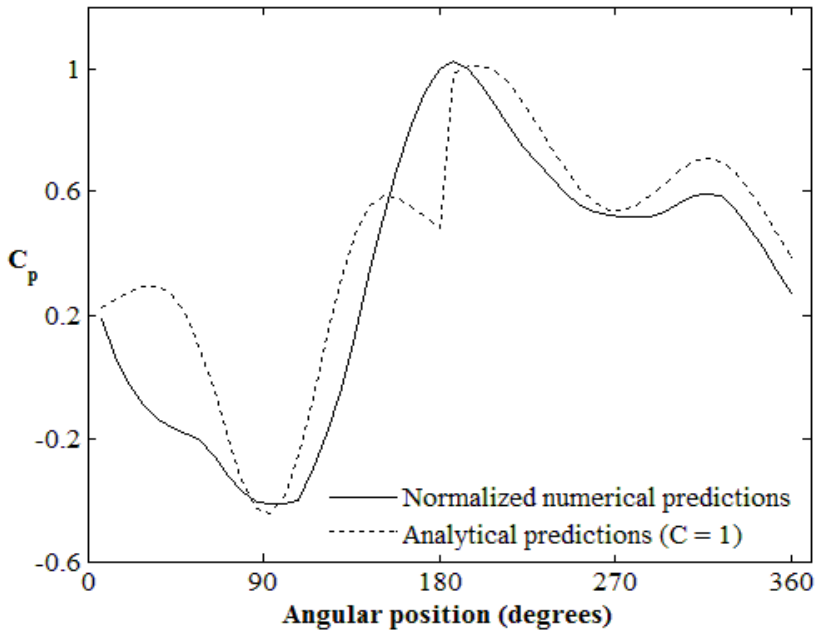

Figure 5-28 Comparison of transient power coefficient between normalized numerical and analytic predictions with $C = 1$ for a single rotor Savonius VAWT

frictional and rotational losses associated with the operation of a Savonius wind turbine. The coefficient C_1 is introduced to approximate these losses. The model will be investigated with three different methods of obtain C_1, each with a varying degree of complexity. In particular, C_1 is considered in relation to rotor position, $C_1(\theta)$, as (i) a constant value, (ii) a continuous function, and (iii) a piecewise function.

Presented in Fig. 5.27, the transient power coefficient is predicted at three constant values of C_1, 0.17, 0.19, and 0.21. All three values of C_1 are close to the same magnitude as the value used to obtain the normalized plot (i.e. 0.194 used to produce Fig. 5.28). Note that the inverse of the angular rotor velocity is close to the value of C_1 that achieves close agreement. This trend is interesting and worthy of future research. Better agreement between the numerical and analytical predictions can be achieved with a correction factor that is dependent on rotor position. However, as illustrated in Fig. 5.29, the difference between the numerical and analytical predictions cannot be adequately

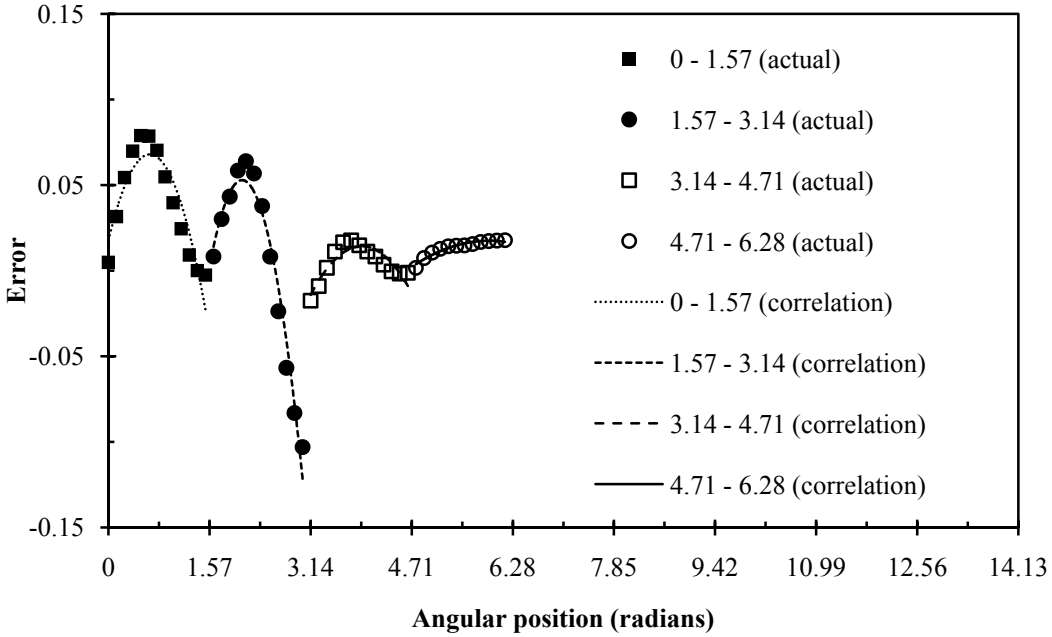

Figure 5-29 The difference in numerical and analytical predictions at varying rotor angles for a single blade Savonius VAWT, represented by C_1

represented by a continuous function of reasonable complexity. Alternatively, a piecewise function of second order polynomials will accurately represent the trends in the predicted error (see Fig. 5.29). The variability in the data set is calculated by R^2. A unique second order polynomial is used to represent each quarter of rotation (i.e. 90°), maintaining a coefficient of determination (R^2) above 0.8, which indicates low variability. The piecewise function is developed as follows:

$$C_1(\theta) = \begin{cases} -0.1217 \cdot \theta^2 + 0.1564 \cdot \theta + 0.0178, & \text{if } 0 \leq \theta < \dfrac{\pi}{2} \\ -0.1983 \cdot \theta^2 + 0.8237 \cdot \theta - 0.8022, & \text{if } \dfrac{\pi}{2} \leq \theta < \pi \\ -0.0453 \cdot \theta^2 + 0.3564 \cdot \theta - 0.6867, & \text{if } \pi \leq \theta < \dfrac{3\pi}{4} \\ -0.0107 \cdot \theta^2 + 0.126 \cdot \theta - 0.3547, & \text{if } \dfrac{3\pi}{4} \leq \theta < 2\pi \end{cases} \tag{5.13}$$

Illustrated in Fig 5.30, the application of C_1 as a piecewise function provides a transient prediction of a one-rotor Savonius VAWT that shows very close agreement with the numerical results.

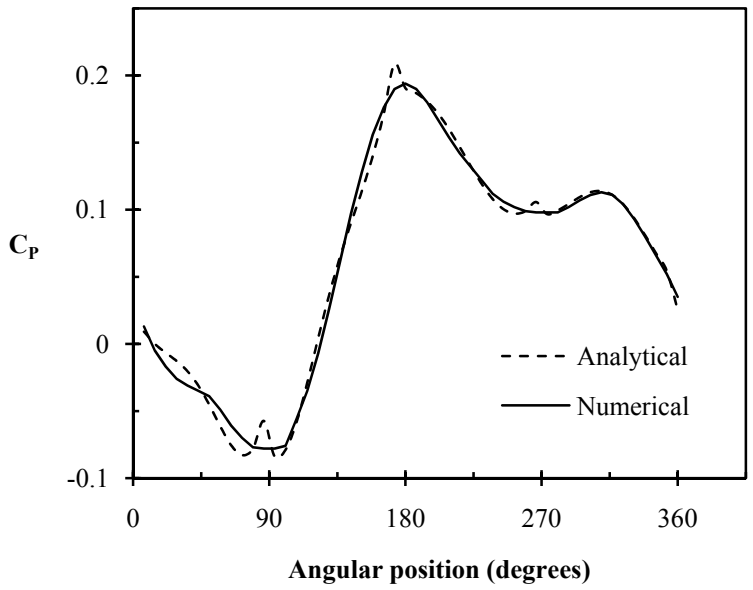

Figure 5-30 Comparison of transient power coefficient between numerical and analytic predictions with C_1 represented by a piecewise function

The number of rotor blades has complex effects on the operational attributes of a Savonius wind turbine. As predicted by the numerical formulation, adding a second rotor blade increases the power output from 0.062 to 0.176, or a factor of 2.8. This positive effect on power can be attributed to deflected air from the power stroke entering the concave side of the return stroke, through the overlap opening, and lowering the negative pressure on the backside of the return rotor blade. Secondly, some of the air will deflect off the convex side of the return stroke and increase the momentum of the air impacting the front surface of the power stroke. Both of these geometrically induced flow fields have a positive effect on performance and they increase the power output from the turbine. The result for the analytical formulation is, $C_{p2}(\theta) \neq C_{P1}(\theta) + C_{P1}(\theta + 180°)$, as further illustrated by Fig. 5.31, which compares this negated analytical relation with the two blade numerical predictions.

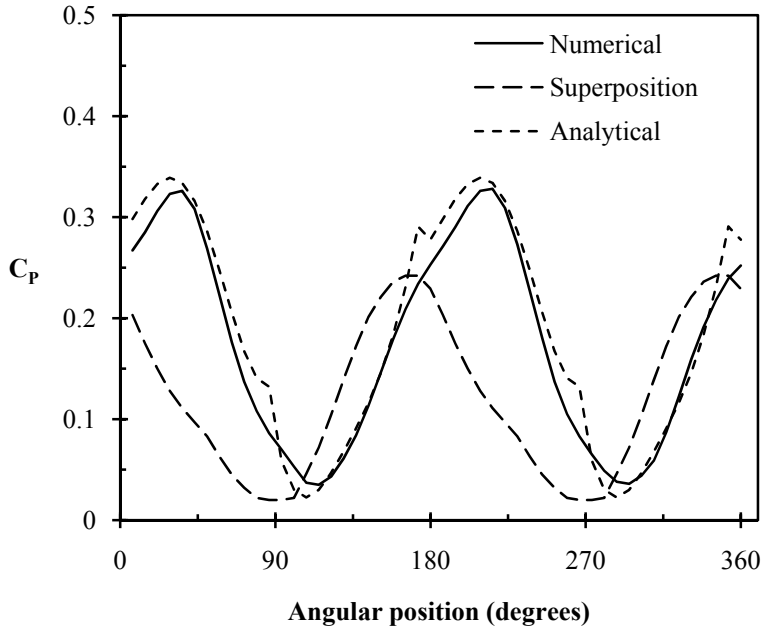

Figure 5-31 Predicted transient power coefficient for a two blade Savonius VAWT

The coefficient C_2 is used to represent the effects of rotor blade number on blade performance. As illustrated in Fig. 5.32, C_2 is developed from the difference in the numerical predictions for a one or two rotor blade turbine. A sinusoidal trendline closely follows the trends in error as follows,

$$C_2 = 0.065 + 0.15\ sin\left(\frac{\theta}{2}\right)$$

The sinusoidal shape with two peaks during one rotation can be explained by the cyclic trends in the two forces discussed previously. As illustrated in Fig. 5.31, combining C_1 and C_2 gives an accurate prediction of the transient power coefficient for a Savonius VAWT. In this plot a piecewise function of C_1 is combined with the sinusoidal C_2. These results have validated the formulations, and demonstrated the valuable utility of the analytical model.

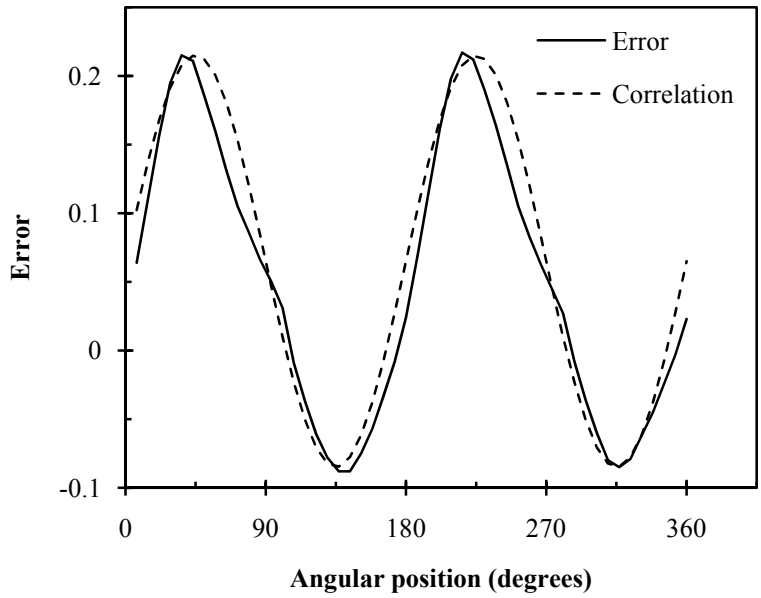

Figure 5-32 The difference in numerical and analytical predictions at varying rotor angles for a two blade Savonius VAWT, represented by C_2

Chapter 6

Conclusions and Recommendations

6.1 Conclusions

In this thesis, new methods to predict a turbines transient power output were presented. The first and second laws were used to compare the performance of a variety of wind power systems. The results indicated a 50 - 53% difference in first and second law efficiencies for the airfoil systems, and 44 - 55% for the VAWTs. Exergy is a useful parameter in wind power engineering, as it can represent a wide variety of turbine operating conditions, with a single unified metric.

Also a new correlation for VAWT performance analysis was presented. The correlation predicted the power coefficient in terms of dimensionless variables including C_p and λ, as well as turbine specific geometrical variables. The model's predictions have close agreement with the numerical results, with an error of 4.4%, 5.8% and 2.9% for three tested geometries, under varying operating conditions. It is a robust correlation that demonstrates that although a turbine's optimal λ is independent of wind speed, it is dependent on the geometry of the particular turbine.

A single state rotor dynamical model was also developed to enhance control mechanisms for extracting maximum power from an incoming air stream with a small HAWT. Unlike the conventional maximum kinetic energy model, the transient rotation of the rotor is included in the turbine power formulation.

A new analytical formulation has been presented to predict the operating trends of a Savonius VAWT. The velocity field produced by flow over a cylindrical rotor was combined with momentum theory to provide a new method to represent the transient power coefficient of a VAWT. A piecewise polynomial function was shown to provide a good representation of the turbine losses. A sinusoidal function accurately represented the interaction caused by the addition of a second rotor blade. Significant opportunity to improve the performance of a Savonius style VAWT is possible with this formulation.

More precise and detailed rotor information can be used for site selection, turbine control and design. Better operating tolerances can improve the system performance through increased turbine capacity and reduced fatigue stresses, thereby reducing operations and maintenance costs. Through these methods, better site selection and turbine design can improve system efficiency, decrease economic cost, and increase the capacity of wind energy systems.

6.2 Recommendations for future research

Several research areas would be useful to improve the predictive techniques in this thesis. The transient power coefficient formulations could be extended to investigate the effect of integration into a hybrid VAWT (a combination of Savonius and Darrius style rotor blades). This would allow the transient operating principles to be identified and the critical design features to be improved. The analytical predictions of a cylindrical

Savonius turbine could be extended to represent different rotor shapes. This could be achieved by supplementing the doublet theory for a flow field, with that of a Rankine oval. This would allow the pressure forces to be represented for an increased number of turbine designs.

The advantages of the model would be improved if they can be extended to variable tip speed ratios. The physical forces that affect C_1 and C_2 could be further examined to improve model precision and accuracy. Investigations into the interaction between multiple turbines, and the effect on performance, would be a valuable contribution. A sensitivity analysis into the relative effect of turbulence intensity on turbine performance and model accuracy would also be of value. Finally, full scale wind tunnel experiments that investigate the effect of rotor geometry, turbulence intensity, and operating principles on transient power curves would provide valuable insight and validation of the model's accuracy and VAWT performance.

Insights gained by the analytical formation could be extended to the Zephyr geometry. The geometry could be designed to better utilize the lift forces generated as the turbine operates. For example, the convex side of the blade could be redesigned to represent an airfoil shape. The shape of the airfoil should be designed to maximize the lift forces throughout its rotation.

References

[1] WWEA (2007). "New World Record in Wind Power Capacity: 14,9 GW added in 2006 Worldwide Capacity at 73,9 GW." World Wind Energy Association, Charles-de-Gaulle-Str. 5, 53113 Bonn, Germany.

[2] WWEA (2008). "Wind turbines generate more than 1 % of the global electricity. World," Wind Energy Association, Charles-de-Gaulle-Str. 5, 53113 Bonn, Germany.

[3] WWEA (2009). "World Wind Energy Report 2008." Wind Energy Association, Charles-de-Gaulle-Str. 5, 53113 Bonn, Germany.

[4] V. Akhmatov (2007). "Influence of Wind Direction on Intense Power Fluctuations in Large Offshore Windfarms in the North Sea." *Wind Engineering*, Vol. 31, No. 1, pp. 59-64.

[5] S. Eriksson, H. Bernhoff, and M. Leijon (2008). "Evaluation of different turbine concepts for wind power." Renewable and Sustainable Energy Reviews, vol. 12, pp. 1419-1434.

[6] U. Saha (2008). "Optimum design configuration of Savonius rotor through wind tunnel experiments," *Journal of Wind Engineering and Industrial Aerodynamics*" Vol. 96 No. 8, pp. 1359-1375.

[7] A. Biswas, R. Gupta, and K.K. Sharma (2007). "Experimental Investigation of Overlap and Blockage Effects on Three-Bucket Savonius Rotors." *Wind Engineering,* Vol. 31, No. 5, pp. 313-368.

[8] H. Hiraharaa, M.Z. Hossainb, M. Kawahashia, and Y. Nonomurac (2005). "Testing basic performance of a very small wind turbine designed for multi-purposes." *Renewable Energy*, Vol. 30, pp. 1279-1297.

[9] R. Gupta, A. Biswas, and K.K. Sharma (2008). "Comparative study of a three-bucket Savonius rotor with a combined three-bucket Savonius-three-bladed Darrieus rotor." *Renewable Energy*, Vol. 33, pp. 1974-1981.

[10] J. A. Alé, M. R. Petry, S. B. Garcia, G.C. Simioni, and G. Konzen (2007). "Performance Evaluation of the Next Generation of Small Vertical Axis Wind Turbine." European Wind Energy Conference & Exhibition, May 7-10, MIC - Milano Convention Centre, Milan, Italy.

[11] C. Sicot, P. Devinant, T. Laverne, S. Loyer and J. Hureau (2006). "Experimental Study of the Effect of Turbulence on Horizontal Axis Wind Turbine Aerodynamics." *Wind Energy*, Vol. 9, pp. 361-370.

[12] G. Botta, M. Cavaliere, S. Viani, and S. Pospõ (1998). "Effects of Hostile Terrains on Wind Turbine Performances and Loads: The Acqua Spruzza Experience." *Journal of Wind Engineering and Industrial Aerodynamics*, Vol. 74-76, pp. 419-431.

[13] V. A. Riziotis and S. G. Voutsinas (2000). "Fatigue loads on wind turbines of different control strategies operating in complex terrain." *Journal of Wind Engineering and Industrial Aerodynamics*, Vol. 85, pp. 211-240.

[14] H. Riegler (2003). "HAWT versus VAWT Small VAWTs find a clear niche." Elsevier Science Ltd., No. 1471 0846, Refocus July/August 2003, pp 44-46.

[15] Y. A. Gayev and E. Savory (1999). "Influence of street obstructions on flow processes within urban canyons." *Journal of Wind Engineering and Industrial Aerodynamics*, Vol. 82, pp. 89-103.

[16] J. Rohatgi and G. Barbezier (1999). "Wind turbulence and Atmospheric Stability - Their Effect on Wind Turbine Output." *Renewable Energy*, Vol. 16, pp. 908-911.

[17] I. P. Castro, H. Cheng, and R. Reynolds (2006). "Turbulence Over Urban-type Roughness: Deductions From Wind-Tunnel Measurements." *Boundary-Layer Meteorology*, Vol. 118: pp. 109-131.

[18] Center for sustainable Energy (2003). "Ealing Urban Wind Study," Ealing Borough Council Urban Wind Study. The CREATE Centre, Bristol.

[19] A. K. Wright and D. H. Wood (2004). "The Starting and Low Wind Speed Behaviour of a Small Horizontal Axis Wind Turbine." *Journal of Wind Engineering and Industrial Aerodynamics*, Vol. 92, pp. 1265-1279.

[20] S. Mertens (2002). "Wind Energy in Urban Areas: Concentrator Effects for Wind Turbines Close to Buildings." Refocus, Vol. 3, No. 2, pp. 22-24.

[21] J. F. DeCarolis and D. W. Keith (2006). "The Economics of Large-scale Wind Power in a Carbon Constrained World." *Energy Policy,* Vol. 34, Iss. 4, pp. 395-410.

[22] D. FitzHerbert (1999). "Electricity Generating Renewables and Global Warming Emissions." *Renewable Energy*, Vol. 16, pp 1057-1063.

[23] K. R. Voorspools, E. A. Brouwers and W. D. D'haeseleer (2000). "Energy Content and Indirect Greenhouse Gas Emissions Embedded in 'Emission-Free'

Power Plants: Results for the Low Countries." *Applied Energy*, Vol. 67, Iss. 3, pp 307-330.

[24] R. K. Rankine, J. P. Chick and G. P. Harrison (2006). "Energy and Carbon Audit of a Rooftop Wind Turbine." *Journal of Power and Energy*, Vol. 220, No. 7, pp. 643-654.

[25] J. G. Slootweg, S. W. de Haan, H. Polinder, and W. L. Kling (2001). "Modeling Wind Turbines in Power System Dynamics Simulations." Power Engineering Society Summer Meeting, 2001. IEEE, Vol. 1, pp. 22-26. Vancouver, Canada.

[26] W. E. Holley (2003). "Wind Turbine Dynamics and Control - Issues and Challenges." Proceedings of the American Control Conference, Denver, Colorado. June 4-6, 2003.

[27] L. Lavoie and P. Lautier (2006). "Nonlinear Predictive Power Controller with Constraint for a Wind Turbine System." IEEE International Symposium on Industrial Electronics, July 9-13, 2006. Vol. 1, pp. 124-129. Montreal, Canada.

[28] P. F. Puleston, R. J. Mantz, P. E. Battaiotto, and F. Valenciaga (2000). "An Adaptive Feedback Linearization Strategy for Variable Speed Wind Energy Conversion Systems." *International Journal of Energy Research*, Vol 24, Iss. 2. pp. 151-161.

[29] P. F. Puleston, R. J. Mantz, P. E. Battaiotto, and F. Valenciaga (2000). "Sliding Mode Control for Efficiency Optimization of Wind Energy Systems with Double Output Induction Generator." *International Journal of Energy Research*, Vol 24, Iss. 1. pp. 77-92.

[30] Z. Lin, G. Qingding (2003). "Adjustable-Pitch and Variable-Speed Control of Wind Turbines Using Nonlinear Algorithm. Electrical Machines and Systems, (ICEMS 2003). Vol. 1, pp. 270-273.

[31] M. J. Dalas, A. Wright, M. Hand, K. Stol (2003). "Dynamics and Control of Horizontal Axis Wind Turbines." American Control Conference, June 4-6, 2003. Vol. 5, pp 3781-3793.

[32] F. Wang, L. Bai, J. Fletcher, J. Whiteford, D. Cullen (2008). "Development of Small Domestic Wind Turbine with Scoop and Prediction of its Annual Power Output." *Renewable Energy*, Vol. 33, pp. 1637-1651.

[33] H. Hirahara, M. Z. Hossain, M. Kawahashi, and Y. Nonomura (2005). "Testing Basic Performance of a Very Small Wind Turbine Designed for Multi-Purposes." *Renewable Energy*, Vol. 30, pp. 1279-1297.

[34] I. Dincer, and M. Rosen (2007) "Exergy. Energy, Environment & Sustainable Development." Burlington, Massachusetts: Elsvier Ltd.

[35] Y. A. Cengel and M. A. Boles (2006). "Thermodynamics: An engineering approach (5th ed.)." Nevada, Reno: McGraw Hill.

[36] O. Adeyinka and G. F. Naterer (2005). "Entropy-Based Metric for Component-level Energy Management: Application to Diffuser Performance." *International Journal of Energy Research*, Vol. 29, No. 11, pp. 1007-24.

[37] G. F. Naterer (2006). "Entropy Based Design of Fuel Cells." *Journal of Fuel Cell Science and Technology*, Vol. 3, No. 2, pp. 165-74.

[38] J. Uche (2006). "Exergy Costs and Inefficiency Diagnosis of a Dual-Purpose Power and Desalination Plant." *Journal of Energy Resources Technology*, Vol. 128, No. 3, pp. 186-192.

[39] R. Jassim (2004). "Exergy Analysis of Carryover Leakage Irreversibilities of a Power Plant Regenerative Air Heater." Proceedings of the Institution of Mechanical Engineers, Part A (Journal of Power and Energy), 218(1), 23-32

[40] A. D Sahin, I. Dincer and M. A. Rosen (2006). "Development of New Spatio-Temporal Wind Exergy Maps," Proceedings of ASME2006 Mechanical Engineering Congress and Exposition, November 5-10, Chicago, Illinois, USA

[41] A. D. Sahin, I. Dincer and M. A. Rosen (2006). "Thermodynamic Analysis of Wind Energy," *International Journal of Energy Research*, Vol. 30, pp. 553-566

[42] B.R. Munson, D.F. young, and T.E. Okiishi (2006). "Fundamentals of Fluid Mechanics (5^{th} ed)," Jefferson City, USA: John Wiley and Sons.

[43] J. B. Zecher (1999) " A New Approach to an Accurate Wind Chill Factor." Bulletin of the American Meteorology Society 80(9): 1893-1899

[44] D. Weisser and T. J. Foxon (2003). "Implications of Seasonal and Diurnal Variations of Wind Velocity for Power Output Estimation of a Turbine: A Case Study of Grenada." *International Journal of Energy Research*, Vol 27., pp. 1165-1179.

[45] M. J. Lampinen, V. W. Kotiaho, and M.E. Assad (2006). "Application of Axial Fan Theory to Horizontal-Axis Wind Turbine." ." *International Journal of Energy Research*, Vol 30, Iss. 13. pp. 1093-1107.

[46] J. F. Manwell, J. G. McGowan, and A. L. Rogers (2002). "Wind Energy Explained: Theory, Design and Application." John Wiley & Sons, West Sussex, United Kingdom.

[47] X. Wang, E. Bibeau, and G.F. Naterer (2007). "Experimental Correlation of Forced Convection Heat Transfer from a NACA Airfoil," *Experimental Thermal and Fluid Science*, Vol. 31, pp. 1073-1082.

[48] X. Wang, G.F. Naterer, and E. Bibeau (2007). "Convective Droplet Impact and Heat Transfer from a NACA Airfoil," *Journal of Thermophysics and Heat Transfer*, Vol. 21, No. 3, pp. 536-542.

[49] ANSYS Inc. (2006). "Fluent 6.3 Users Guide," ANSYS Inc, Southpointe, 275 Technology Drive, Canonsburg, Pennsylvania 15317, USA.

[50] A.D. Gosman (1999). "Developments in CFD for Industrial and Environmental Applications in Wind Engineering," *Journal of Wind Engineering and Industrial Aerodynamics*, Vol. 81, pp. 21-39.

[51] ANSYS Inc. (2005). "Gambit 2.3.16 Users Guide," ANSYS Inc, Southpointe, 275 Technology Drive, Canonsburg, Pennsylvania 15317, USA

[52] P.S.Veers, and S.R. Winterstein (1998). "Application of Measured Loads to Wind Turbine Fatigue and Reliability Analysis," *Journal of Solar Energy Engineering*, Vol. 120, No. 4, pp. 233-239

[53] E. Denny, (2006). "Wind Generation, Power System Operation, and Emissions Reduction." IEEE transactions on power systems, 21(1), 341-7.

[54] W. D. Jones (2007). "Ontario Quits Coal. In the provinces energy plans, Kyoto looms large." IEEE Spectrum 07. pp 12-13.

[55] Statistics Canada (2008) "Population and Dwelling Counts, for Canada, Provinces and Territories, and Urban Areas, 2006 and 2001 Censuses - 100% data" Statistics Canada, Ottawa, Ontario.

[56] T. M. Harchaoui (2003). “Greenhouse Gas Emissions in the Canadian Economy, 1981-2000.” Statistics Canada, Micro-Economic Analysis Division, Ottawa.

[57] Statistics Canada (2006). “Electric Power Generation, Transmission and Distribution.” Catalogue no. 57-202-X

[58] S. Earle (2008). “Environmental Implications of Fossil Fuels.” Environmental Science: Perspectives and Relationships, Energy and the Environment. Vancouver Island University, British Columbia, Canada.

[59] RETScreen International, Empowering Cleaner Energy Decisions. “RETScreen Clean Energy Project Analysis Software.” Natural Resources Canada, Ottawa, Canada

[60] W. Weibull (1951). "A Statistical Distribution Function of Wide Applicability," J. Appl. Mech.-Trans. ASME, Vol. 18, No. 3, 293-297.

[61] C. G. Justus (1978). “Winds and Wind System Performance.” Franklin Institute Press, Philadelphia, PA.

[62] Atlantic Orient Canada (2004). “AOC 15/50 Wind Turbine Generator Brief Operation Data and Technical Specifications,” Wind Energy Systems for the World. Atlantic Orient Canada Inc, 300 Prince Albert Road, Suite 200 Dartmouth, Nova Scotia, Canada.

[63] Entegrity Wind Systems Inc. (2008). “EW50 Specifications” EW 50 Turbine,” Entegrity Wind Systems Inc, 4855 Riverbend Rd. Suite 100. Boulder, Colorado 80301, USA.

[64] Eoltec (2003). “Eoltec Scirocco 5.5-6000 Wind Turbine Performances,” Scirocco High Efficiency Ø5.6m/6kW Professional Wind Turbine. Eoltec, 455, promenade des Anglais, porte de l'Arenas, Hall C, 06299 Nice Cedex, France.

[65] Eoltec (2006). "Eoltec WindRunner 11-25 Wind Turbine Performances," Windrunner High Efficiency Ø11m/25kW Professional Wind Turbine. Eoltec, 455, promenade des Anglais, porte de l'Arenas, Hall C, 06299 Nice Cedex, France.

[66] Air Breeze Technologies (2008). "Air Breeze VAWT 50kW Air Breeze VAWT Technical Data Specifications & Power Curves," Create Energy with the Innovation of Vertical Axis Wind Turbines. Air Breeze Technologies.

[67] PacWind Inc. (2008). "SeaHawk Owners and Installation Manual," Alpha Series, 500W SeaHawk Vertical Axis Wind Turbine MorningStar TriStar-60. PacWind Inc, 23930 Madison Street, Torrance, CA 90505, USA.

[68] K. Pope, G. F. Naterer, and E. Tsang (2008). "Effects of Rotor-Stator Geometry on Vertical Axis Wind Turbine Performance," Canadian Society for Mechanical Engineers 2008 forum, June 5-8, Ottawa, Canada.

[69] M. S. Selig (2004). "Wind tunnel aerodynamic tests of six airfoils for use on small wind turbines." *Journal of Solar Energy Engineering*, 126(4), 986-1001

[70] H. G. Martinez (2007). "3D boundary layer study on a rotating wind turbine blade." *Journal of Physics* - Conference Series, 75(1), 012032-1

[71] R. E. Wilson, P. B. Lissaman, S. N. Walker (1976) "Aerodynamic Performance of Wind Turbines." Energy Research and Development Administration, ERDA/NSF/04014-76/

[72] G. Hunt and E. Savory (2006). "Report on Wind Tunnel Tests of the Performance of Vertical Axis Turbines," Department of Mechanical and Materials Engineering University of Western Ontario, London, Canada.

[73] Microsoft Corporation (2007). "Excel statistical functions: PEARSON." Microsoft Help and Support, Article ID: 828129.